ABSTRACT

Title of dissertation: NONLINEAR CONTROL DESIGN

TECHNIQUES FOR PRECISION

FORMATION FLYING

AT LAGRANGE POINTS

Richard J. Luquette, Doctor of Philosophy, 2006

Dissertation directed by: Associate Professor Robert M. Sanner
Department of Aerospace Engineering

Precision spacecraft formation flying is an enabling technology for a variety of proposed space-based observatories, such as NASA's Terrestrial Planet Finder (TPF), the Micro-Arcsecond X-Ray Imaging Mission (MAXIM), and Stellar Imager (SI). This research specifically examines the precision formation flying control architecture, characterizing the relative performance of linear and nonlinear controllers. Controller design is based on a 6DOF control architecture, characteristic of precision formation flying control. In an effort to minimize the influence of design parameters in the comparison, analysis employs "equivalent" controller gains, and incorporates an integrator in the linear control design. Controller performance is evaluated through various simulations designed to reflect a realistic space environment. The simulation architecture includes a full gravitational model

and solar pressure effects. Spacecraft model properties are based on realistic mission design parameters. Control actuators are modeled as a fixed set of thrusters for both translation and attitude control. Analysis includes impact on controller performance due to omitted dynamics in the model (gravitational sources and solar pressure) and model uncertainty (mass properties, thruster placement and thruster alignment).

Linearized equations of relative motion are derived for spacecraft operating in the context of the Restricted Three Body Problem. Linearization is performed with respect to a reference spacecraft within the formation. Analysis demonstrates robust stability for the Linear Quadratic Regulator controller design based on the linearized dynamics.

Nonlinear controllers are developed based on Lyapunov analysis, including both non-adaptive and adaptive designs. While the linear controller demonstrates greater robustness to model uncertainty, both nonlinear controllers exhibit superior performance. The adaptive controller provides the best performance. As a key feature, the adaptive controller design requires only relative navigation knowledge.

Analysis demonstrates the ability of the nonlinear controller to compensate for unknown dynamics and model uncertainty. Results exhibit the potential of a nonlinear adaptive architecture for improving controller performance. Nonlinear adaptive control is a viable strategy for meeting the extreme control requirements associated with formation flying missions like MAXIM and Stellar Imager. Mission specific analysis from a systems perspective is required to determine the best controller design.

NONLINEAR CONTROL DESIGN TECHNIQUES FOR PRECISION FORMATION FLYING AT LAGRANGE POINTS

by

Richard J. Luquette

Dissertation submitted to the Faculty of the Graduate School of the
University of Maryland, College Park in partial fulfillment
of the requirements for the degree of
Doctor of Philosophy
2006

Advisory Committee:
Associate Professor Robert M. Sanner, Chair/Advisor
Professor Darryll J. Pines
Professor Norman M. Wereley
Professor Emeritus William W. Adams
Dr. F. Landis Markley

Dedicated In Memory Of:

Parents

Norman A. and Helen J. Luquette

Brothers

Norman A. Luquette, Jr.

Robert A. Luquette

William E. Luquette

Brother-in-Law

Lawrence Kime

Father-in-Law

Edward Baclawski

Acknowledgments

While the contributions of this research reflect many personally invested hours in analysis and study, great credit is attributed to those who supported me. As I reflect on the experience, a number of people emerge as key players, deserving of my personal recognition and gratitude.

I thank my advisor, Professor Rob Sanner for his persistent encouragement and guidance. I thank each member of my dissertation committee, Professor Darryll Pines, Professor Norman Wereley, Professor William Adams, and Dr. F. Landis Markley of NASA/Goddard Space Flight Center.

I owe gratitude to many of my colleagues at NASA's Goddard Space Flight Center. Notably, Dr. Jesse Leitner, both colleague and friend, supported me as an encourager and enabler. He also served as a technical advisor and reviewer, and contributed his knowledge and experience with formation flying technology to help ensure practical relevance of this research. John VanEepoel spent careful hours supporting editorial review.

My involvement in youth ministry through my local church and the nation-wide Spoke Folk Ministries blessed me with an extensive network of people, who served both to encourage and inspire. The names are too many to list, but I'm indebted to each member of this community.

Family was another important contributor to this accomplishment. Most importantly my parents served a critical role throughout my life as nurturers, supporters and encouragers. Unfortunately, the were only able to witness the

beginnings of this endeavor. Their deaths prevent them from joining the graduation celebration.

My colleague, fellow graduate student and friend, Julie Thienel (more formally Dr. Julie Thienel!!!) has been central throughout my graduate experience. We endured hours of classroom lectures, challenging assignments, and seemingly endless research. We served and encouraged each other through long years of study, and emerged as everlasting friends.

My greatest debt is owed to my wife, Debby, for her continual support, encouragement and tolerance through our years of marriage.

As a closing, I consider my life threaded with constants and variables. The variables are people and a changing environment. Certain people have an enduring presence in my life, others come and go. However, people change through life. The principal constant in my life is my faith. Therefore, I end with a prayer of thanks to the God who equipped me with the academic skills and persistence required to complete this effort, and who provided my supporters, highlighted above.

Table of Contents

List of Tables

List of Figures

Chapter 1

Introduction

1.1 Background

"The first science in the modern sense that grew in the Mediterranean civilisation was astronomy...The rudiments of astronomy exist in all cultures, and were evidently important in the concerns of early people all over the world."

From Jacob Bronowski, *The Ascent of Man* [4]

1.1.1 Motivation...Looking to the Stars

Our continued quest to understand the universe is evident in our pursuit of technologies to enhance our observational capability. Space-based observatories, such as the Hubble Space Telescope, provide dramatically superior image quality in comparison to Earth-based observatories. Looking to the future, Distributed Spacecraft System (DSS) technologies will enable higher resolution imagery and interferometry, robust and redundant fault-tolerant architectures, and complex networks dispersed over clusters of satellites.

1.1.2 Mechanism...Spacecraft Precision Formation Flying

A Distributed Spacecraft System (DSS) is a collection of two or more spacecraft functioning to fulfill a shared or common objective. As a subset of the DSS architecture, formation flying missions add the requirement to maintain a relative position and/or orientation with respect to each other, or a common target. The term precision formation flying implies a requirement for continuous control (normally implemented in discrete time) to maintain the formation within the design specification. Control system designs for precision formation flying missions will vary based on the dynamic environment. For example, the dynamic environment for low Earth orbit differs significantly from that experienced in deep space.

Numerous formation flying missions are under development to enhance our remote sensing capability, including the Terrestrial Planet Finder, the Micro-Arcsecond X-Ray Imaging Mission, and the Stellar Imager. Although currently conceived as single spacecraft, Constellation-X was evaluated as a formation flying mission, and is used to characterize another mission profile. A description of each of these missions is deferred to Section 1.3.

The success of each of these missions depends on varied sets of enabling technologies, with a precision formation flying requirement critical to each. Specific formation definition and control requirements are mission dependent. These missions are ordered by their range of demands for formation flying technology. TPF requires position control at the level of centimeters over a separation distance of a kilometer. As a formation flying concept, Constellation-X requires millimeter

level control over a separation distance of 50 meters. MAXIM and SI, the most challenging, require micron to nanometer level control oversub-kilometer to kilometer ranges. The spacecraft control requirement for each of these missions is driven by optical performance requirements. Combining spacecraft control with active optical control serves to reduce the spacecraft position control requirements listed above.

1.1.3 Context...Libration Point Missions

Due to the large spacecraft separations and tight control requirements discussed above, the low Earth orbit environment is generally unfavorable for precision formation flying due to the high fuel cost associated with overcoming the local gravitational gradient. Therefore, TPF, Constellation-X, MAXIM, and SI are currently envisioned to orbit the Earth/Moon-Sun, L_2, libration point. This region of space is characterized by a benign gravitational gradient, compared to those experienced in a local Earth orbit.

Libration points are defined within the context of a rotating reference frame defined by two large masses rotating about their common center of mass, Figure 1.1. A libration point represents a location within the rotating frame at which the dynamical forces due to gravity and rotation are in equilibrium. These solutions, also referred to as Lagrange points, were first identified by Lagrange in 1772, as published in his prize memoir, *Essai sur le Probl'eme des Trois Corps*, [46]. In the absence of perturbing forces, an object placed at any one of these locations remains fixed in

3

the rotating frame. Libration point locations for the Earth/Moon-Sun system are identified in Figure 1.2.

Libration points L_1, L_2 and L_3, termed collinear, are unstable. The stability of the equilateral points, L_4 and L_5, is dependent on the mass ratio, ρ, of the two primary masses. The points are unstable if $0.03852 < \rho < 0.96148$, otherwise they are stable. For the Earth/Moon-Sun system with $\rho = 0.000003$, L_4 and L_5 are stable [68]. A detailed discussion of libration points, including stability properties, appears in the next chapter, Section 2.1.

While L_1 and L_2 are naturally unstable, it is possible to stabilize an orbit about either point with reasonable fuel cost. The regions surrounding L_1 and L_2 provide desirable locations for certain missions. Both regions are within reasonable proximity of Earth, easing the challenges of accessibility and communications between Earth stations and the spacecraft. As previously noted,
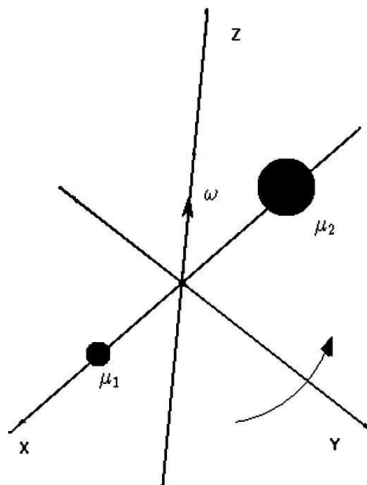
Figure 1.1: Rotating Frame for Two Body System
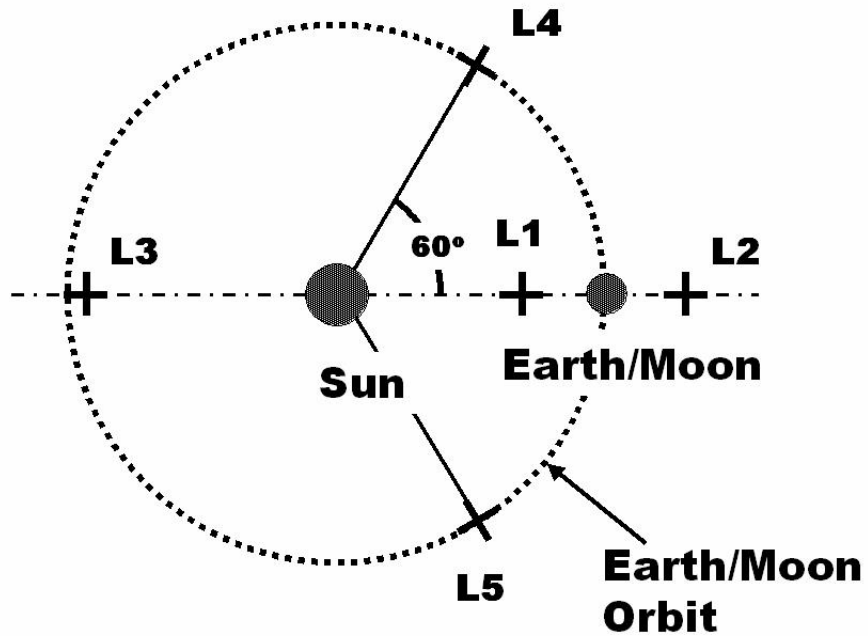
Figure 1.2: Lagrange/Libration Points in Earth/Moon-Sun Rotating Frame

fuel economy is a critical design consideration for space missions. The regions surrounding L_1 and L_2 provide the important advantage of a shallow gravity gradient, compared to the gravity field experienced by an Earth orbiting mission. A shallow gravity gradient supports the goal of minimizing fuel requirements while achieving formation performance criteria. Simultaneous reduction in solar and Earth interference provides the advantage of L_2 over L_1 for a mission designed to probe deep space.

1.1.4 Focus...Formation Control

From a systems perspective precision formation flying requires a high level of autonomy with an enabling subset of component technologies. Defined in the context of closed-loop control, the components generally align with metrology, estimation, control design and actuation.

Most of these technologies exist in some form. Formation flying demands refinement of each technology to a higher level of performance. Detailed exploration of each technology and the associated development challenges is beyond the scope of this effort. However, it is important to recognize interdependencies with formation flying technology development.

The precision formation flying control problem is uniquely defined for various mission classes, due to differences in the dynamic environment, principally the gravity field. Motivated by mission concepts for TPF, Constellation-X, MAXIM and SI, this research effort focuses on the precision formation control algorithm design problem within the context of the restricted three body problem. Research objectives are detailed in the next section.

1.2 Research Focus

This research was originally designed to address the specific problem of precision formation control in the vicinity of the Earth/Moon-Sun L_2, libration point. However, the analysis framework generalizes to other trajectories within the context of the Earth/Moon-Sun gravity field, as well as other RTBP rotating frames.

The theoretical construct for linear and nonlinear control algorithms is presented in Chapters 3 and 5. A benchmark problem, discussed below, provides a relevant scenario for demonstrating the theory. Modeling and analysis in Chapters 4 and 6, conform to the benchmark problem for libration point missions, presented in [5].

1.2.1 A Benchmark Problem

The general problem is to design a control algorithm for the Follower to track a desired trajectory relative to a Leader spacecraft in the context of a virtual space-based observatory. This new class of missions defines the extreme requirements for precision formation control.

The benchmark problem, based on a realistic mission profile, defines a generic formation design problem for a space-based telescope with a 20 spacecraft sparse aperture aligned with a distant detector spacecraft. The specifications permit independent control of each aperture spacecraft with respect to the detector spacecraft in a Leader/Follower configuration. The Leader/Follower architecture, applied in this research, allows modeling the formation with three spacecraft, a Leader and two Followers, Figure 1.3. One Follower, the Freeflyer, maintains a trajectory in close proximity to the Leader. The second Follower, the Detector, maintains a distant trajectory. The two Follower formation facilitates examination of control strategies for both short and long separation distances.

The three spacecraft, Leader/Follower formation is stationed in the vicinity of L_2 in the Earth/Moon-Sun rotating frame. Each Follower is required to
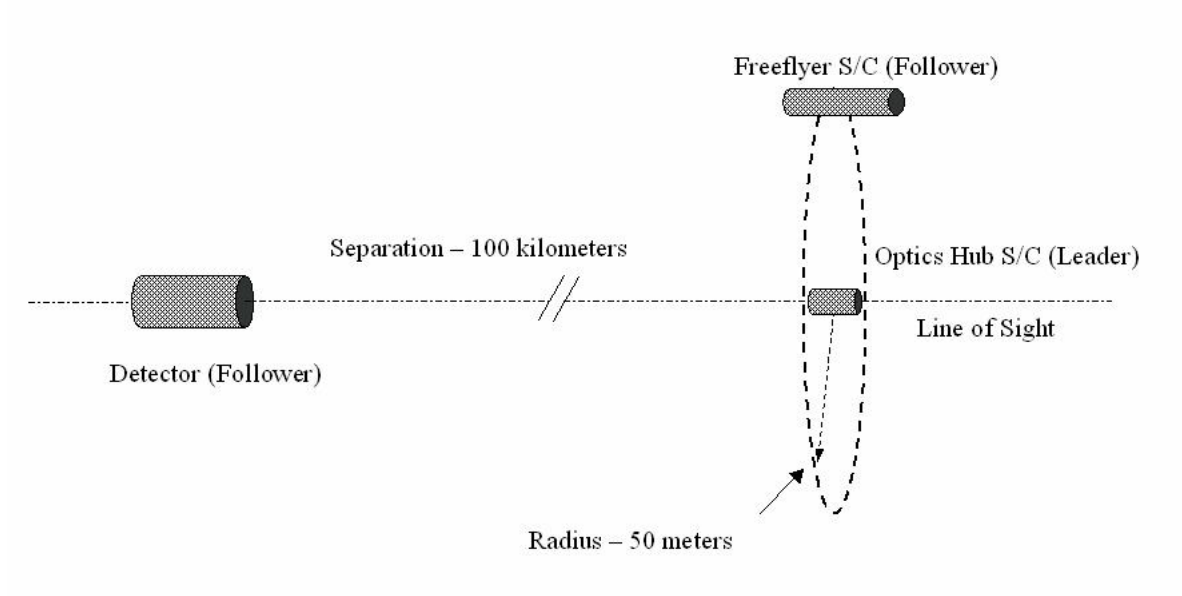
Figure 1.3: Three Spacecraft Formation Design for a Large Aperture Telescope Mission
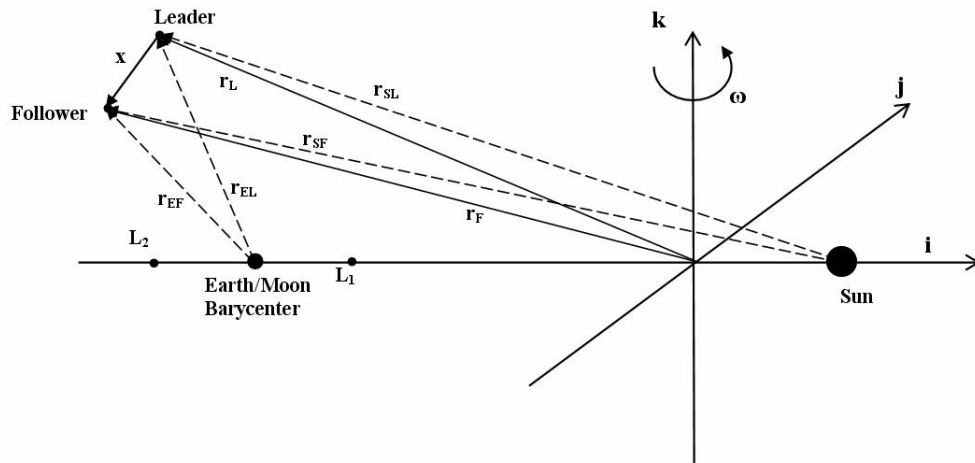
Figure 1.4: Two Spacecraft Formation Operating in the Earth/Moon-Sun Rotating Frame

maintain a predetermined trajectory (position and attitude) relative to the Leader, effectively defining two distinct formations with the Leader as a common spacecraft. Figure 1.4 depicts a typical Leader/Follower formation. The Earth/Moon system is modeled as a combined mass located at the system center of mass to facilitate control design. The Earth and Moon are treated as separate bodies for simulations. The position and relative motion of the Earth/Moon barycenter about the Sun defines the rotating frame. The Leader maintains a planned ballistic trajectory with periodic station-keeping maneuvers, and a predetermined attitude trajectory. Attitude control on the Leader is accomplished with reaction wheels to avoid perturbing its orbit trajectory. Each Follower tracks a specified separation and attitude trajectory relative to the Leader. Measurement data provides the relative position and velocity between the two spacecraft. Each spacecraft is equipped to measure attitude, referenced to an inertial coordinate frame. Each Follower is equipped with fixed thrusters to serve as actuators for both translation and attitude maneuvers. Thrusters are fully throttleable. Detailed spacecraft and trajectory specifications for the benchmark problem are included in the modeling discussion in Section 4.1.

1.2.2 Generalized Architecture

As introduced, the control algorithm applied to the benchmark problem is based on a generalized architecture within the context of the restricted three body problem. While motivated by mission scenarios similar to the benchmark problem,

9

the theoretical framework is constructed about the dynamics for a generic restricted three body problem (RTBP), Section 2.1. The control strategies are formulated with the general RTBP dynamics and simplifying assumptions, such as a slow moving trajectory with the RTBP rotating frame. The result is a generalized architecture for defining formation flying control laws, and an analysis framework for characterizing their performance.

1.2.3   Thesis

The goal of this research is to provide a fair performance comparison of linear and nonlinear control strategies applied to the precision formation flying problem to test the following assertion through analysis.

1.2.3.1   Assertion:

Linear control may prove adequate to meet formation flying requirements with less stringent performance specifications. However, a linear control design provides inadequate compensation to overcome perturbations due to unmodeled nonlinearities in the system dynamics necessary to achieve the strict performance requirements for precision formation flying. The control performance specifications for MAXIM and SI, require nonlinear adaptive techniques applied to the six-degree of freedom (6DOF) control problem with coupled attitude and orbit dynamics.

1.2.3.2 Analysis:

Analysis provides the mechanism for testing the thesis. Three basic control designs are developed: Linear, Nonlinear (based on Lyapunov theory), and Nonlinear Adaptive (also Lyapunov based). Control gains for each design are chosen to be "equivalent", allowing fair comparison of the performance. Tracking performance is assessed with simulations. The MATLAB based simulation employs a rigid body model for attitude dynamics, a realistic gravity model based on planetary ephemeris data, and a model for solar pressure. Controller robustness to model uncertainty is demonstrated through analysis and simulation.

1.3 Precision Formation Flying Missions

As discussed earlier, a principal goal for precision formation flying is to support advanced astronomy missions. Several of these missions are highlighted here.

The Terrestrial Planet Finder (TPF) is designed to detect and characterize remote planets from formation through various stages of development. Science goals include spectrographic analysis of planetary atmospheres, seeking to identify planetary bodies with the capacity to support life. TPF aims to locate tiny, faint planets around distant stars, requiring suppression of the glare from the parent star by a factor of a million or better. This level of suppression will enable imaging of planetary systems as far away as 50 light years. With a resolution a hundred times finer than the Hubble Space Telescope, TPF also allows the study of the black hole at the center of the Milky Way and other exciting phenomena in the

universe. As one of several design concepts TPF is proposed as an interferometer composed of a four-element linear array of a spacecraft formation in orbit about the Earth/Moon-Sun L_2 libration point. Target dependent, spacecraft separations range 75-1000 meters with a control tolerance on the order of centimeters. The attitude control requirement for the individual spacecraft is on the order of a few arcminutes. [35, 48, 50, 61]

The Constellation-X Observatory (Con-X) will enable scientists to investigate black holes, Einstein's Theory of General Relativity, galaxy formation, the evolution of the Universe on the largest scales, the recycling of matter and energy, and the nature of "dark matter". The current concept for Con-X is a single spacecraft. However, several alternative design concepts have been considered for the observatory. One envisions a formation of two spacecraft acting as a virtual X-ray telescope. Based on this design, Con-X will orbit the Earth/Moon-Sun L_2 libration point. The two spacecraft will maintain a 50 meter separation with a control tolerance on the order of millimeters. The formation will remain inertially fixed during observations. Repointing maneuvers will occur approximately twice a day over a period of one hour with a nominal slew angle of 60 degrees. The attitude control requirement for the individual spacecraft is on the order of arcseconds.[10]

The Micro-Arcsecond X-Ray Imaging Mission (MAXIM) is an X-Ray observatory, designed to image the event horizon of a black hole. With light trapped by its strong gravitational field, direct imaging of a black hole is not possible. However, it is possible to image the event horizon, a region surrounding the

black hole characterized by strong X-Ray emissions. The current MAXIM concept envisions a central optics hub spacecraft, surrounded by a fleet of 32 spacecraft, forming a 500-1000 meter diameter ring. The fleet has even angular spacing in the optical plane with a random radial distribution. The array forms an X-Ray lens, focused on a detector spacecraft, located 20,000 kilometers from the optics hub/ring array along the line of sight. The position control requirement for the spacecraft optics forming the ring array about the hub is on the order of nanometers. The spacecraft position control could be reduced with active optics. The detector spacecraft is required to maintain the 20,000 kilometer separation range to within 10 meters while holding the position error off the line of sight to a tolerance on the order of microns.

MAXIM Pathfinder, a proposed predecessor mission to the full MAXIM mission, is designed to demonstrate the feasibility of space-based X-ray interferometry for astronomical applications. The Pathfinder mission concept limits the ring array to six spacecraft, and operates with relaxed, extremely challenging, control tolerances at a reduced range of 450 kilometers. The attitude control requirement for these missions is on the order of arcseconds. Pathfinder is not currently supported as part of the MAXIM mission development, but provides a good design profile for analysis. [8, 19, 20, 21, 22, 37, 44, 55]

Stellar Imager (SI) provides a space-based UV-optical Fizeau Interferometer with an angular resolution of 100 micro-arcseconds. SI is designed to study the various effects of stellar magnetic fields, the field generating dynamos, and the

internal structure and dynamics of the associated stars. Ultimately the science goal is to achieve the best-possible forecasting of solar activity on time scales ranging up to decades, combined with understanding the impact of stellar magnetic activity on astrobiology and life in the universe. SI consists of a reconfigurable array of 10-30 one-meter class "mirrorsats", forming a 0.5 kilometer primary mirror, focused on a hub (detector) spacecraft separated along the line of sight by ∼5 kilometers. Maintenance of the range between the "mirrorsats" and the hub requires control to the level of nanometers. Spacecraft attitude control requirements are on the order of 10's of micro-arcseconds. [6, 7, 20, 56]

1.4 Formation Flying - Current Technology Assessment

Precision formation control is a topic of active research. EO-1, launched in November 2000, is NASA's first mission to successfully demonstrate autonomous formation flying [15]. EO-1's orbit was designed to lag LANDSAT-7's ground track by one minute with a tolerance of +/- 6 seconds, equivalent to a 450 kilometer along track separation with a tolerance of 85 kilometers. EO-1 represents a basic form of formation flying with orbit control implemented as discrete maneuvers, approximately every three weeks. The EO-1 formation flying experiment was conducted during the period, January-July 2001, and November 2001. While EO-1's baseline mission was completed in November 2001 the spacecraft continues to support Earth science.

Another indicator of the importance of formation flying development is the

near term, proposed ST9 mission concept. ST9 is a technology demonstration mission funded under NASA's New Millennium Program. Precision Formation Flying is one of five technologies competing for the ST9 flight opportunity. In contrast to EO-1 the ST-9 precision formation flying mission concept is conceived to demonstrate continuous control. Details for the ST-9 mission concept are not publicly available. [47]

The following subsection highlights recent technology developments associated with precision formation flying.

1.4.1 Current Control Technology

In 1994, Egeland and Godhaven [14] published an adaptive attitude control law for a rigid spacecraft, providing the framework for the attitude portion of the control law presented here. Conventional attitude control systems are based on linear models. This design is based on the nonlinear attitude dynamics and provides an adaptive mechanism to autotune the controller performance. Their work builds on earlier research by Wen and Kreutz-Delgado (1991) [66], Slotine and DiBenedetto (1990) [57], and Crouch (1984) [11].

The general problem of 6DOF (position/attitude) vehicle control is addressed by Fossen and Sagatun (1991) [16], and reappears in [17]. Their work focuses on the problem of 6DOF control of underwater vehicles. However, the framework is applicable to the 6DOF control problem for spacecraft formation flying.

The design for relative position control is based on an analysis of the

relative equations of motion, derived from basic astrodynamics [1, 2, 68], and adaptive nonlinear control [58]. Related work on this topic is presented in [3, 12, 25, 32, 45, 59, 65].

Wang, Hadaegh and Lau (1999) [65] explored the problem of synchronized, formation rotation and attitude control. The analysis demonstrates coordinated simultaneous control of relative position and attitude within a formation. However, the spacecraft dynamic model assumes a gravity-free and disturbance-free environment.

deQueiroz, Kapila and Yan (2000) [12] propose a relative position adaptive control law for a formation in a circular orbit. Adaptation is applied to compensate for uncertainty/slow variation in spacecraft mass properties, disturbance forces and gravity. Their work builds on earlier research by Kapila, Sparks, Buffington and Yan (2000) [32] and by Vassar and Sherwood (1985) [63]. The formation design includes two spacecraft in a Leader/Follower configuration. The Leader follows a ballistic trajectory while the Follower is controlled to orbit the Leader in a circular path with a 100 meter radius. Simulated results employ a geostationary Earth orbit and artificially assume a fixed disturbance force, rather than employing a high fidelity dynamic simulator. The analysis only addresses relative position control with perfect actuation. Spacecraft attitude effects are not considered.

Hamilton, Folta and Carpenter (2002) [26] examined the problem of relative position control for a formation stationed in the vicinity of the Earth/Moon-Sun L_2 libration point. Their control design is based on linearized dynamics extracted

from Generator, a high fidelity simulator developed at Purdue University. While the linearized dynamics matrix is time-varying the design treats it as constant, applying periodic updates. Since Generator is computationally intensive, a typical mission scenario would require periodic uploading/updating of the control algorithm based on tracking data. Ground-based tracking data analysis would estimate an updated spacecraft state. The updated state would be fed to Generator, then Generator would update the state-space expression for the linearized dynamics. Finally, the new gain matrix, computed using linear control design, would be uploaded to the spacecraft. Their design includes a Kalman filter to examine the impact of measurement noise. Attitude dynamics are not addressed. Perfect actuation is assumed.

Marchand and Howell (2005) [43], also exploited Generator to study natural formations and control strategies for formations in the vicinity of a libration point. Their analysis compared the application of nonlinear and linear control designs. The nonlinear designs utilized feedback linearization techniques. As in [26], the linear design is based on the linear dynamics matrix computed with Generator. The technique employed for feedback linearization requires knowledge of the spacecraft state. Attitude dynamics are not addressed. Perfect actuation is assumed. Results demonstrated equivalent performance based on tracking error and fuel consumption. The analysis did not assess the impact of unmodeled dynamics and modeling errors on tracking performance.

In 2003 Gurfil, Idan and Kasdin (2003) [25] proposed an adaptive control

algorithm for deep-space formation flying. The approach uses feedback linearization, applies control methods for linear systems, and then adds a neural network to compensate for unmodeled dynamics. The equations of relative motion, the basis of the control law design, assume circular-restricted three body problem (CRTBP) dynamics. The feedback linearization mechanism requires the spacecraft state relative to the reference frame origin, the Earth. The analysis only addresses relative position control, and assumes perfect actuation.

Related research includes the study of the control architecture for large spacecraft formations. Mesbahi and Hadaegh (2001) [45] examine the application of logic-based switching in combination with elementary graph theory linear matrix inequalities to define a framework for implementing control of large formations. The design assumes linear dynamics. Beard, Lawton and Hadaegh (2001) [3] study the issue of coordinated control for large spacecraft formations. Their study assumes a gravity-free and disturbance-free environment.

Finally in recent literature, Hsiao and Scheeres (2005) [27] examine control strategies for stabilizing natural relative spacecraft motion for formations orbiting libration points. The study is conducted in the context of the circular restricted three body problem. The control strategy employs pole placement to locate the poles of the stabilized linearized dynamics along the imaginary axis.

Smith and Hadeagh (2005) [59] present a method of formation control using switched topologies. A centralized control topology is designed based on all relative spacecraft measurements within the formation. Analysis shows the equivalence of

distributed local relative control topologies when redundant relative measurements are unavailable. Switching between the equivalent topologies is applied on individual spacecraft based on available measurements. The analysis assumes a gravity and disturbance free environment.

Vaddi, Alfriend, Vadali and Sengupta (2005) [62] develop a control strategy for a two spacecraft formation orbiting a central body. The strategy utilizes orbital element differences. Analysis shows the solution is fuel-optimal and maintains homogenous fuel consumption between spacecraft. Their results correlate with similar numerical optimization studies.

Sengupta and Vadali (2005) [54] present an orbit transfer/formation control algorithm for an Earth orbiting spacecraft. Their approach employs Lyapunov analysis with Euler parameters to characterize the orbit.

Based on this review of current literature, several key observations are made regarding formation flying technology.

Cited works:

- Focus on problem specific formation control in either Earth orbit or in the vicinity of the Earth/Moon-Sun L_2 libration point. Lack of a common framework makes comparing results difficult.

- Employ numerical analysis tools, such as Generator, to model RTBP dynamics.

- Assumed perfect actuation and knowledge of spacecraft parameters.

- Focus on translation control as a 3DOF problem without considering attitude maneuvers.

- Neglect modeling uncertainty associated with dynamics, mass properties, and actuator performance.

- Require knowledge of absolute spacecraft states to compute control.

The next section identifies specific contributions of this research.

1.5   Contributions and Conclusions

Based on noted observations from the literature review, this research is directed toward development of a generic 6DOF (coupled translation/attitude) approach to the formation flying control problem within the context of the RTBP. Also, adopting the benchmark problem framework from [5] facilitates future comparative analysis. The following discussion traces the development of this research, highlighting relevant publications and contributions.

1.5.1   Preliminary Analysis

The initial effort examined the application of nonlinear adaptive control techniques to track a prescribed trajectory about the Earth-Moon L_2 point, reference [38]. The adaptation mechanism compensated for unmodeled dynamics (solar pressure and gravity). The control design, based on the Circular Restricted Three Body Problem dynamics, performed successfully despite modeling errors associated

with gravitational dynamics. Analysis demonstrated the gravitational influence of the sun is non-negligible within the Earth-Moon system. In fact the angular momentum of the Earth-Moon system varies in direction and magnitude due to the sun's gravity field. Also, the lunar orbit is slightly elliptic with an eccentricity of 0.055. While perhaps an unlikely application of continuous control, this step established a foundation for building the control architecture for precision formation flying.

Next, reference [39] studied nonlinear adaptive methods applied to formation control. In this case the formation was stationed near the Earth/Moon-Sun L_2 point. As with the previous case, adaptation compensated for unmodeled dynamics associated with gravity and solar pressure. The control design assumed perfect actuation independent of the spacecraft attitude.

Finally, reference [40], developed the 6DOF formation control architecture, combining translation and attitude control. Adaptation compensated for uncertain mass properties in addition to the dynamic modeling errors associated with gravity and solar pressure.

1.5.2 Linearized Relative Dynamics

Linear control theory offers the designer with a rich heritage of tools. However, application of the tools requires an equivalent linear expression of the true nonlinear system dynamics. As noted, prior work employs numerical models to compute the dynamics relative to a reference spacecraft, or applied the linearized dynamics

about the libration point. Numerical models for relative linearized dynamics are computationally expensive. Linearized dynamics about a libration point are easily computed with analytic methods, but do not accurately reflect the linearized dynamics of the formation [41].

Reference [41] represents a key contribution through development of an analytic expression of the linearized dynamics about a Leader spacecraft. Prior work commonly views relative dynamics in terms of a RTBP rotating frame when modeling system behavior near a libration point. This perspective unnecessarily constrains the problem. To maintain generality linearization is performed using inertial coordinates with restricted three body problem dynamics. Details are presented in Section 2.1.2. While time-varying, an important feature of the solution is its applicability for any trajectory of the reference spacecraft. Therefore, the linearized model can be applied for missions stationed in the vicinity of any libration point or alternative trajectories such as an Earth drift away orbit. Reference [42] demonstrates the utility of the analytic linear model in a linear control design for the MAXIM mission.

1.5.3   6DOF Control Design

Spacecraft position and attitude control are typically treated as independent problems. The approach is appropriate for single spacecraft. Precision formation flying implies a requirement for continuous control. While unforced spacecraft translation and attitude dynamics are uncoupled, continuous thruster firing

potentially induces a coupling action. Using a common set of actuators (thrusters), the design approach couples the translation and attitude control problem into a single 6DOF architecture. The coupling action is particularly important if the physical characteristics of the thrusters are uncertain, i.e. pointing and placement. This issue is particularly important for the nonlinear adaptive control design, and is discussed in detail in Sections 5.2.2 and 5.5.

1.5.3.1 Linear Control Design

The Linear Quadratic Regulator (LQR) is a common technique for linear control design, providing robust and optimal performance. However, an LQR design requires time invariant dynamics. Recall, the linearized relative dynamics for the formation flying problem are time varying. Therefore, a gain scheduling strategy is required which assumes time invariant dynamics over regular intervals. A robustness analysis in Section 3.2.2.3 shows the dynamics allow a time invariant characterization with LQR gain updates computed every two weeks. The two week time period is specific for the selected design scenario (benchmark problem). A mission specific robustness analysis must be performed to determine the appropriate interval for gain scheduling.

Standard linearization of the rigid body attitude dynamics is applied to extend the design to 6DOF control. Chapter 3 reviews linear control design theory and develops the linear control design structure for the formation flying problem.

Chapter 4 presents specific details on the controller design for the benchmark problem and simulation results.

1.5.3.2 Nonlinear Control Design

The stated thesis goal is to present a comparative analysis of linear and nonlinear control designs. The specific nonlinear control approach is a Lyapunov based design. Both nonadaptive and adaptive formulations are considered. Design theory details appear in Chapter 3 (nonadaptive) and Chapter 5 (adaptive). An important requirement for performance comparison is the specification of nonlinear controller gains that are "equivalent" to the linear design. As noted, linear gains are computed using LQR. The definition of equivalent gains is explained in Sections 4.2 and 6.1.

1.5.3.3 Adaptation

The adaptive mechanism of the nonlinear controller represents a set of integrators structured according to the system dynamics. The structure enables systematic compensation for model uncertainty, resulting in improved performance. The adaptive nonlinear controller design compensates for unmodeled dynamics associated with gravity and solar pressure, mass property uncertainty, and actuator (thruster) performance uncertainty.

1.5.3.4 Implementation Issues

Precision formation flying implies autonomous spacecraft control, minimizing the interface with ground based control networks. Implementation of a linear control design requires knowledge of the absolute reference spacecraft state to compute the linearized equations of motion. Similarly control designs presented in the literature review require absolute spacecraft state knowledge. Absolute spacecraft knowledge requires ground based tracking and analysis. Therefore these control designs are not fully autonomous.

Another important contribution is the development of a nonlinear adaptive design that requires only relative state measurements. The design is limited by general assumptions, such as slow moving trajectories within the RTBP frame. However, the assumptions are consistent with profiles for proposed formation flying missions. The nonlinear nonadaptive controller also depends on absolute state knowledge. The adaptive design compensates for unmodeled gravitational and solar dynamics, and uncertainty in mass properties and thruster performance.

1.5.4 Simulation Results

Simulation results for the linear and nonadaptive nonlinear controllers are presented in Chapter 4. Nonlinear adaptive controller simulation results appear in Chapter 6. Controller performance is characterized with and without unmodeled dynamics and uncertain spacecraft parameters.

The simulation is based on realistic spacecraft parameters and employs a

full gravity model based on planetary ephemeris data. The control cycle is set at one Hertz, typical for attitude control systems. Perhaps one unrealistic aspect of the simulation is the duration of the reconfiguration maneuvers. Typically these maneuvers would occur over much longer periods of time, reducing the required fuel. However, the compressed maneuver periods provide a consistent scenario to assess controller performance, and provide the benefit of reduced computational time for the simulation.

The linear controller is robust to dynamics and mass uncertainty. However, performance degrades when confronted with actuator performance uncertainty. In contrast the nonadaptive nonlinear controller provides orders of magnitude better tracking control in the absence of model uncertainty. Each component of model uncertainty degrades tracking performance. However, the nonlinear nonadaptive controller outperforms the linear controller based on maximum and mean tracking error.

The nonlinear adaptive controller exhibits the best overall tracking characteristic. Simulation results in Chapter 6 reflect equivalent performance for the nonadaptive and adaptive controller designs in the absence of modeling uncertainty, both orders of magnitude better than the linear control design. While performance degraded, the adaptive controller demonstrates the ability to compensate for unmodeled dynamics and uncertainties. For the case including all uncertainties, the adaptive controller outperformed the nonadaptive design by two orders of magnitude based on mean error for both translation and attitude tracking.

1.6 Synopsis of Contributions

While not conclusive, this analysis supports the thesis that nonlinear adaptive control methods, as compared to tradition linear designs, are advantageous in the development of precision formation flying algorithms. Ultimately the best controller design is mission specific, based on many factors including the trajectory profile, spacecraft parameters, actuators and performance requirements.

The following list highlights the contributions and unique features of this work mentioned above.

- Derived analytic expression for linearized relative spacecraft dynamics within a RTBP framework

  - Eliminates need for numerical models of relative dynamics

  - Time-varying expression valid for any unforced trajectory of the reference spacecraft, not constrained to vicinity of libration point

  - Analytic model provides a tool to understand the natural relative dynamics without the tedium of numerical simulation

- Coupled, 6DOF translation/attitude dynamics model

  - Accounts for dynamic coupling associated with actuation (thrusters)

- Linear versus Nonlinear Control Performance Comparison

  - Based on "equivalent" gains

– Benchmark problem simulation framework, facilitates comparison with other research

• Stable, real-time adaptive controller development

– Compensates for mass property uncertainty

– Compensates for thruster performance uncertainty

– Compensates for unmodeled dynamics (gravity and solar pressure)

• Modified adaptive control law

– Removes need for absolute position information

1.6.1 List of Publications

Luquette, R. J. and Sanner, R. M., "A Nonlinear Approach to Spacecraft Trajectory Control in the Vicinity of a Libration Point," *Proceedings of the Flight Mechanics Symposium*, Goddard Space Flight Center, June 2001.

Luquette, R. J. and Sanner, R. M., "A Nonlinear Approach to Spacecraft Formation Control in the Vicinity of a Collinear Libration Point," *Proceedings of the AAS/AIAA Astrodynamics Specialist Conference*, July 2001, Paper No. AAS 01-330.

Luquette, R. J. and Sanner, R. M., "A Nonlinear, Six-Degree of Freedom, Precision Formation Control Algorithm, Based on Restricted Three Body Dynamics," *26th Annual AAS Guidance and Control Conference*, February 2003, Paper No. AAS 03-007.

Luquette, R. J. and Sanner, R. M., "Linear State-Space Representation of the Dynamics of Relative Motion, Based on Restricted Three Body Dynamics," *AIAA Guidance, Navigation and Control Conference*, August 2004, Paper No. AIAA-2004-4783.

Luquette, R. J., Sanner, R. M., Leitner, J. and Gendreau, K. C., "Formation Control for the MAXIM Mission," *2nd International Symposium on Formation Flying*, September 2004.

Chapter 2

Spacecraft Dynamics

This chapter reviews spacecraft orbital and attitude dynamics to provide the context for the control design discussion in the following chapters. Section 2.1 presents the orbital dynamics with specific emphasis on the Restricted Three Body Problem. The discussion includes linearized equations of motion about Libration points and stability analysis. Section 2.2 discusses rigid body spacecraft kinematics and dynamics. Section 2.3 discusses dynamic coupling between the orbital and attitude dynamics.

2.1   Orbital Dynamics

As discussed in Chapter 1, the region surrounding the Earth/Moon-Sun L_2 point provides a favorable dynamic environment for precision formation flying missions designed to probe deep space. Orbital dynamics in this region, as well as near other libration points, are governed by gravity and solar pressure, plus thruster action. Principal gravitational sources are the Sun and the Earth/Moon system. For control design the Earth/Moon system is treated as a combined mass located at the system barycenter. The spacecraft are comparably small such that their mutual gravitational interaction is neglected. References for spacecraft orbital dynamics include: [1, 2, 46, 68].

The dynamics associated with the gravity field of the Earth/Moon-Sun is appropriately modeled by the Restricted Three Body Problem (RTBP). This section begins with a review of the RTBP, followed by a discussion of the dynamics of relative motion with the context of the RTBP.

2.1.1 Restricted Three Body Problem

The Restricted Three Body Problem (RTBP) examines the behavior of an infinitesimal test mass in the combined gravitational field of two finite masses orbiting their common center of mass, Figure 2.1. The description and analysis of this problem appear in many texts. Reference [68] is the principal source for this discussion. In the most general form of the problem the two primary masses (primaries) follow elliptical trajectories. Analysis is greatly simplified by assuming circular trajectories of the primaries about their barycenter. Euler originally formulated the Circular Restricted Three Body Problem (CRTBP) in 1772.

The structure of the CRTBP is depicted in Figure 2.2. The coordinate system is constructed so the X-axis passes through the center of each mass with the larger mass located in the positive X-direction. The Z-axis is in the direction of angular velocity of the two primary masses about the barycenter. The Y-axis completes the triad forming a right handed coordinate frame.

The equations of motion in inertial coordinates for the test mass within the context of CRTBP dynamics is expressed as:

$$m\ddot{\boldsymbol{r}} = -\mu_1 m \frac{\boldsymbol{r_1}}{||\boldsymbol{r_1}||^3} - \mu_2 m \frac{\boldsymbol{r_2}}{||\boldsymbol{r_2}||^3}$$
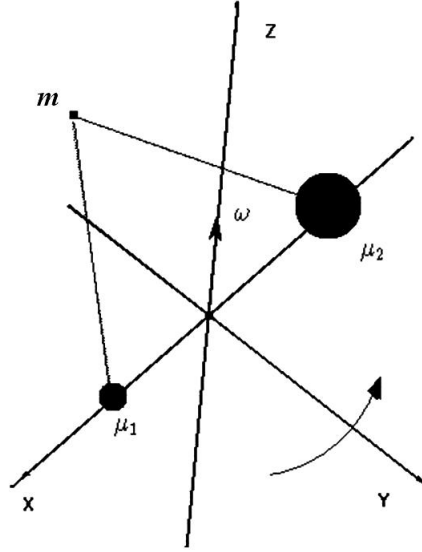
Figure 2.1: General Restricted Three Body Problem, Plane of Rotation

Where:

$\mu_i \quad = GM_i$, Gravitational Parameter for Primary Mass, M_i,

$\boldsymbol{r}_i \quad$ – Infinitesimal Mass Position from Primary Mass, M_i

$m \quad$ – Mass of Infinitesimal Test Mass/Spacecraft

Transforming the equations of motion into the rotating frame of the CRTBP

provides a natural framework for evaluating the dynamic behavior of the test mass.

$$
\begin{aligned}
\ddot{X} - 2n\dot{Y} - n^2 X &= -\frac{\mu_1(X-D_1)}{\|\boldsymbol{r_1}\|^3} - \frac{\mu_2(X+D_2)}{\|\boldsymbol{r_2}\|^3} \\
\ddot{Y} + 2n\dot{X} - n^2 Y &= -\frac{\mu_1 Y}{\|\boldsymbol{r_1}\|^3} - \frac{\mu_2 Y}{\|\boldsymbol{r_2}\|^3} \\
\ddot{Z} &= -\frac{\mu_1 Z}{\|\boldsymbol{r_1}\|^3} - \frac{\mu_2 Z}{\|\boldsymbol{r_2}\|^3}
\end{aligned}
\tag{2.1}
$$
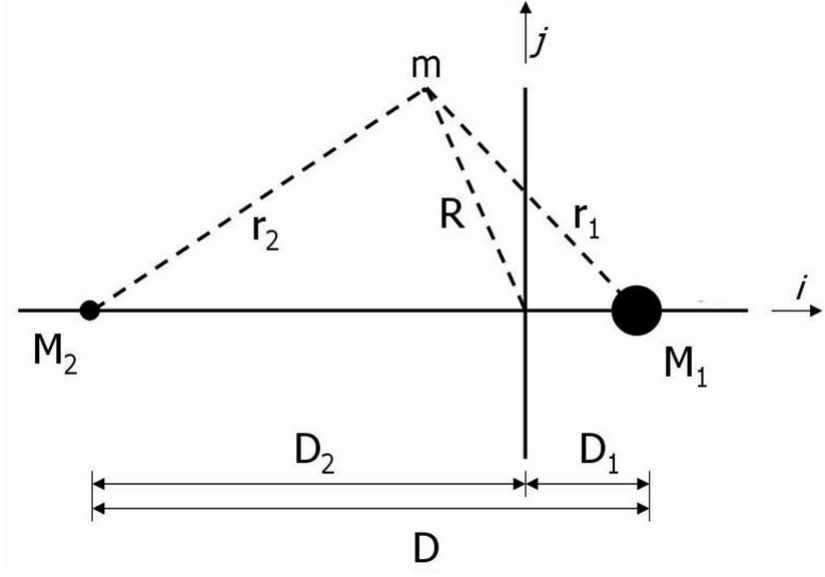
Figure 2.2: Circular Restricted Three Body Problem

Where:

D — Distance Between Primaries, Constant

D_i — Distance of Primary Mass, M_i, from the Barycenter, Constant

n = $\sqrt{(\mu_1 + \mu_2)/D^3}$, Angular Velocity of Primaries about Barycenter

R = $Xi + Yj + Zk$, Location of Infinitesimal Test Mass/Spacecraft

Introducing non-dimensional parameters facilitates analysis and maintains generalized results. Non-dimensional parameters are defined such that D, $(M_1 + M_2)$, and n have unity values. Defining $\rho = \frac{M_2}{M_1 + M_2}$, the additional parameters assume the following values:

$$\mu_1 = (1 - \rho) \qquad \mu_2 = \rho$$

$$D_1 = \rho \qquad D_2 = (1 - \rho)$$

Using the non-dimensional parameters, Equation 2.1 is expressed as:

$$\ddot{X} - 2\dot{Y} - X = -\frac{(1-\rho)(X-\rho)}{||\boldsymbol{r_1}||^3} - \frac{\rho(X+1-\rho)}{||\boldsymbol{r_2}||^3}$$

$$\ddot{Y} + 2\dot{X} - Y = -\frac{(1-\rho)Y}{||\boldsymbol{r_1}||^3} - \frac{\rho Y}{||\boldsymbol{r_2}||^3} \qquad (2.2)$$

$$\ddot{Z} = -\frac{(1-\rho)Z}{||\boldsymbol{r_1}||^3} - \frac{\rho Z}{||\boldsymbol{r_2}||^3}$$

With: $||\boldsymbol{r_1}|| = \sqrt{(X-\rho)^2 + Y^2 + Z^2}$, and $||\boldsymbol{r_2}|| = \sqrt{(X+1-\rho)^2 + Y^2 + Z^2}$.

2.1.1.1 Libration Points

The dynamics expressed in Equation 2.2 yield natural equilibrium points, generally termed Libration Points, also Lagrangian Points. The equilibrium point locations are computed by setting the derivative terms in Equation 2.2 to zero, and solving for X, Y and Z. The defining equations for the equilibrium points are:

$$X = \frac{(1-\rho)(X-\rho)}{||\boldsymbol{r_1}||^3} + \frac{\rho(X+1-\rho)}{||\boldsymbol{r_2}||^3} \qquad \text{(a)}$$

$$Y = \frac{(1-\rho)Y}{||\boldsymbol{r_1}||^3} + \frac{\rho Y}{||\boldsymbol{r_2}||^3} \qquad \text{(b)} \qquad (2.3)$$

$$\boldsymbol{0} = \frac{(1-\rho)Z}{||\boldsymbol{r_1}||^3} + \frac{\rho Z}{||\boldsymbol{r_2}||^3} \qquad \text{(c)}$$

Equation 2.3c yields, $Z = 0$. Hence all the equilibrium points lie in the $X - Y$ plane. The location of these points are depicted in Figure 2.3. The points are divided into two groups. The collinear points L_1, L_2 and L_3 lie along the X-axis. The location of the collinear points is governed by the value of ρ, determined by solving Equation 2.3a with $Y = Z = 0$. The equation does not lend itself to an analytic solution, so numerical methods are required. The Triangular (also, Equilateral) Points, L_4 and L_5, are at the apex of an equilateral triangle with the

34
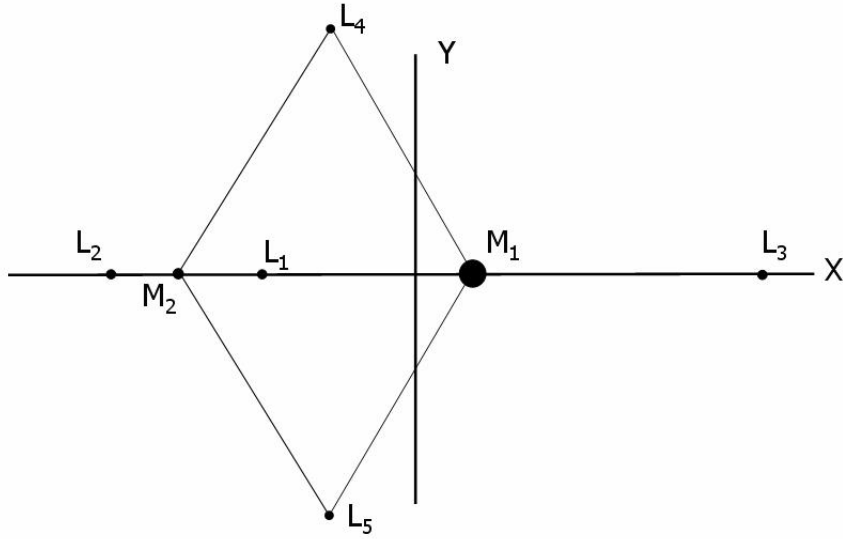
Figure 2.3: Libration Point Locations for Circular Restricted Three Body Problem

base defined as the line between M_1 and M_2. As geometry governs the location of
the Triangular Points, their locations are readily determined as: $[(\rho - \frac{1}{2}), \pm\frac{\sqrt{3}}{2}, 0]$.

2.1.1.2 Stability of Libration Points

Stability properties of the Libration Points are determined by examining the
characteristics of the linearized equations of motion about each point. Denoting the
location of an equilibrium point as: $[X_0, Y_0, Z_0]$, the coordinates of the test mass are
defined as: $[X_0 + x, Y_0 + y, Z_0 + z]$. The linearized equations of motion relative to a
Libration Point are given by:

$$\ddot{x} - 2\dot{y} - x = -\left\{(1-\rho)\left[\frac{1}{||\boldsymbol{R_1}||^3} - 3\frac{(X_0-\rho)^2}{||\boldsymbol{R_1}||^5}\right] + \rho\left[\frac{1}{||\boldsymbol{R_2}||^3} - 3\frac{(X_0+1-\rho)^2}{||\boldsymbol{R_2}||^5}\right]\right\}x$$

$$+ \left\{3(1-\rho)\frac{(X_0-\rho)Y_0}{||\boldsymbol{R_1}||^5} + 3\rho\frac{(X_0+1-\rho)Y_0}{||\boldsymbol{R_2}||^5}\right\}y$$

$$\ddot{y} + 2\dot{x} - y = \left\{3(1-\rho)\frac{(X_0-\rho)Y_0}{||\boldsymbol{R_1}||^5} + 3\rho\frac{(X_0+1-\rho)Y_0}{||\boldsymbol{R_2}||^5}\right\}x \tag{2.4}$$

$$- \left\{(1-\rho)\left[\frac{1}{||\boldsymbol{R_1}||^3} - 3\frac{(X_0-\rho)^2}{||\boldsymbol{R_1}||^5}\right] + \rho\left[\frac{1}{||\boldsymbol{R_2}||^3} - 3\frac{(X_0+1-\rho)^2}{||\boldsymbol{R_2}||^5}\right]\right\}y$$

$$\ddot{z} = -\left\{\frac{(1-\rho)}{||\boldsymbol{R_1}||^5} - \frac{\rho}{||\boldsymbol{R_2}||^5}\right\}z$$

With: $||\boldsymbol{R_1}|| = \sqrt{(X_0-\rho)^2 + Y_0^2}$, and $||\boldsymbol{R_2}|| = \sqrt{(X_0+1-\rho)^2 + Y_0^2}$.

Inspection of Equation 2.4 reveals coupling in the X-Y plane motion. The motion along the Z-axis is uncoupled from the X-Y motion. If excited, Z-axis dynamics at each point exhibit undamped harmonic motion with a frequency of $\omega_z = \sqrt{\frac{(1-\rho)}{||\boldsymbol{R_1}||^5} - \frac{\rho}{||\boldsymbol{R_2}||^5}}$. Understanding the natural motion in the X-Y plane requires separate analysis for the Triangular Points and the Collinear Points.

The stability of the Triangular Points is evaluated by substituting their location, $[(\rho - \frac{1}{2}), \pm\frac{\sqrt{3}}{2}, 0]$, into Equation 2.4, yielding the matrix form of equations for in-plane motion:

$$\dot{\boldsymbol{\xi}} = \boldsymbol{A_T}\,\boldsymbol{\xi} \tag{2.5}$$

Where:

$$\boldsymbol{\xi} = \begin{bmatrix} x \\ y \\ \dot{x} \\ \dot{y} \end{bmatrix} ; \quad \boldsymbol{A_T} = \begin{bmatrix} 0 & 0 & 1 & 0 \\ 0 & 0 & 0 & 1 \\ \frac{3}{4} & \frac{3\sqrt{3}}{2}(\rho-\frac{1}{2}) & 0 & 2 \\ \frac{3\sqrt{3}}{2}(\rho-\frac{1}{2}) & \frac{9}{4} & -2 & 0 \end{bmatrix}$$

Stability properties are determined by the roots of the characteristic equation:

$det(\lambda\,\mathbf{I} - \mathbf{A_T}) = 0$, which reduces to: $\lambda^4 + \lambda^2 + \frac{27}{4}\rho(1-\rho) = 0$

The roots, given by: $\lambda = \pm\sqrt{\frac{-1\pm\sqrt{1-27\rho(1-\rho)}}{2}}$, are purely imaginary for $\rho \leq 0.033852$

or $\rho \geq 0.96148$. For $0.033852 < \rho < 0.96148$, the roots are complex pairs with one set

in the right hand plane (unstable), and the other set in the left hand plane (stable).

The Triangular Points are stable for both the Earth-Moon system ($\rho = 0.01215$)

and the Sun - Earth/Moon system ($\rho = 3.0404e - 006$).

The location of the Collinear Points is expressed as: $[X_0, 0, 0]$. Substituting

the coordinates into Equation 2.4, yields:

$$\dot{\boldsymbol{\xi}} = \boldsymbol{A_C}\,\boldsymbol{\xi} \qquad (2.6)$$

Where:

$$\boldsymbol{\xi} = \begin{bmatrix} x \\ y \\ \dot{x} \\ \dot{y} \end{bmatrix} ; \quad \boldsymbol{A_C} = \begin{bmatrix} 0 & 0 & 1 & 0 \\ 0 & 0 & 0 & 1 \\ (2\sigma+1) & 0 & 0 & 2 \\ 0 & -(\sigma-1) & -2 & 0 \end{bmatrix}$$

Where: $\sigma = \frac{(1-\rho)}{(X_0-\rho)^3} + \frac{\rho}{(X_0+1-\rho)^3}$

The characteristic equation is:

$det(\lambda\,\mathbf{I} - \mathbf{A_C}) = 0$, expressed as: $\lambda^4 - (\sigma-2)\lambda^2 - (2\sigma+1)(\sigma-1) = 0$

The roots, given by: $\lambda = \pm\sqrt{\frac{(\sigma-2)\pm\sqrt{(\sigma-2)^2+4(2\sigma+1)(\sigma-1)}}{2}}$, consist of two purely

imaginary roots and two real roots, symmetric about the origin. Hence, the Collinear

Points are unstable for all values of ρ.

The orbit of the Earth/Moon barycenter about the sun is nearly circular with an eccentricity of 0.0167. Therefore, the CRTBP provides a reasonable model of the dynamics associated with the Libration Points for the Sun/Earth-Moon System. As previously stated, reference [68] is the principal source for the material related to the CRTBP.

2.1.2   Dynamics of Relative Motion in the Restricted Three Body Problem

A typical two spacecraft formation is depicted in Figure 2.4. The spacecraft are designated Leader and Follower. In this scenario, the Leader spacecraft is intended to follow a ballistic trajectory with infrequent control for orbit maintenance. Control is only applied to the Follower spacecraft to maintain a specified trajectory relative to the Leader spacecraft.

A linear model of the relative dynamics sets the framework for linear control design. Libration points represent natural locations for linearizing the dynamics with the context of the RTBP. The linearized dynamics relative to a libration point are presented in the previous section as part of the stability analysis. However, applying this form of the linearized dynamics to the problem of spacecraft relative motion limits the validity and utility of the model to regions within close proximity of a libration point. Linearizing the dynamics about a reference spacecraft provides a generalized solution, applicable to any trajectory within the context of the RTBP. The development begins with the nonlinear equations of relative motion.
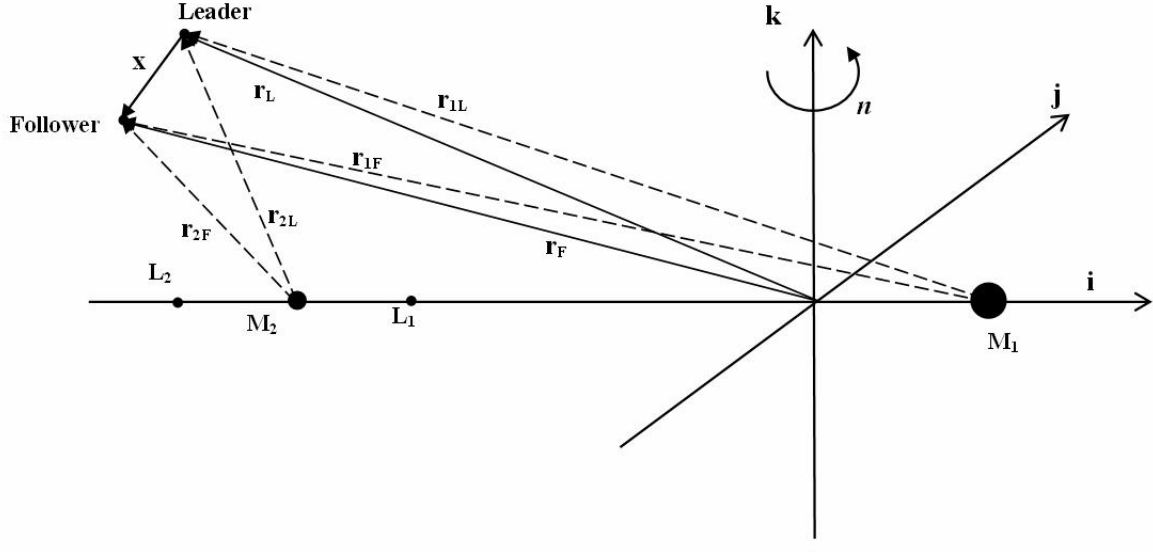
Figure 2.4: Two Spacecraft Orbiting in the RTBP Frame

The equations of relative motion in inertial coordinates are obtained by differencing the equations of motion for the Follower and Leader.

$$
\begin{aligned}
\ddot{\boldsymbol{r}}_F &= -\mu_1 \frac{\boldsymbol{r}_{1F}}{\|\boldsymbol{r}_{1F}\|^3} - \mu_2 \frac{\boldsymbol{r}_{2F}}{\|\boldsymbol{r}_{2F}\|^3} + \boldsymbol{u}_{thrust,F} \\
\ddot{\boldsymbol{r}}_L &= -\mu_1 \frac{\boldsymbol{r}_{1L}}{\|\boldsymbol{r}_{1L}\|^3} - \mu_2 \frac{\boldsymbol{r}_{2L}}{\|\boldsymbol{r}_{2L}\|^3} \\
\ddot{\boldsymbol{x}} &= \left(-\mu_1 \frac{\boldsymbol{r}_{1F}}{\|\boldsymbol{r}_{1F}\|^3} - \mu_2 \frac{\boldsymbol{r}_{2F}}{\|\boldsymbol{r}_{2F}\|^3} + \boldsymbol{u}_{thrust,F} \right) - \left(-\mu_1 \frac{\boldsymbol{r}_{1L}}{\|\boldsymbol{r}_{1L}\|^3} - \mu_2 \frac{\boldsymbol{r}_{2L}}{\|\boldsymbol{r}_{2L}\|^3} \right) \qquad (2.7) \\
&= -\left\{ \frac{\mu_1}{\|\boldsymbol{r}_{1F}\|^3} + \frac{\mu_2}{\|\boldsymbol{r}_{2F}\|^3} \right\} \boldsymbol{x} - \mu_1 \left\{ \frac{1}{\|\boldsymbol{r}_{1F}\|^3} - \frac{1}{\|\boldsymbol{r}_{1L}\|^3} \right\} \boldsymbol{r}_{1L} \\
&\quad - \mu_2 \left\{ \frac{1}{\|\boldsymbol{r}_{2F}\|^3} - \frac{1}{\|\boldsymbol{r}_{2L}\|^3} \right\} \boldsymbol{r}_{2L} + \boldsymbol{u}_{thrust,F}
\end{aligned}
$$

Equation 2.7 represents the full nonlinear dynamics of relative motion. As discussed, linearization of the relative dynamics about the Leader (reference) spacecraft position sets the framework for linear control design. The Leader/Follower separation is assumed to be much smaller than the distance of

39

the Leader (or Follower) to either of the primary masses, $||\boldsymbol{x}|| << ||\boldsymbol{r_{1L}}||$ and $||\boldsymbol{x}|| << ||\boldsymbol{r_{2L}}||$. As the first step, several terms on the right hand side of this expression are examined, beginning with the term $\left\{ \frac{1}{||\boldsymbol{r_{1F}}||^3} - \frac{1}{||\boldsymbol{r_{1L}}||^3} \right\}$

$$
\begin{aligned}
\left\{ \frac{1}{||\boldsymbol{r_{1F}}||^3} - \frac{1}{||\boldsymbol{r_{1L}}||^3} \right\} &= \left\{ \frac{1}{||\boldsymbol{r_{1L}}+\boldsymbol{x}||^3} - \frac{1}{||\boldsymbol{r_{1L}}||^3} \right\} \\
&= \left\{ \frac{1}{[(\boldsymbol{r_{1L}}+\boldsymbol{x})\cdot(\boldsymbol{r_{1L}}+\boldsymbol{x})]^{3/2}} - \frac{1}{||\boldsymbol{r_{1L}}||^3} \right\} \\
&= \left\{ [(||\boldsymbol{r_{1L}}||^2 + ||\boldsymbol{x}||^2) + 2\,(\boldsymbol{r_{1L}} \cdot \boldsymbol{x})]^{-3/2} - ||\boldsymbol{r_{1L}}||^{-3} \right\} \\
&= \left\{ \left[\left(1 + \left(\frac{||\boldsymbol{x}||}{||\boldsymbol{r_{1L}}||}\right)^2 + 2\,\frac{(\boldsymbol{r_{1L}}\cdot\boldsymbol{x})}{||\boldsymbol{r_{1L}}||^2}\right]^{-3/2} - 1 \right\} ||\boldsymbol{r_{1L}}||^{-3}
\end{aligned}
\tag{2.8}
$$

As assumed $||\boldsymbol{x}|| << ||\boldsymbol{r_{1L}}||$,

$$
1 + \left(\frac{||\boldsymbol{x}||}{||\boldsymbol{r_{1L}}||}\right)^2 + 2\,\frac{(\boldsymbol{r_{1L}}\cdot\boldsymbol{x})}{||\boldsymbol{r_{1L}}||^2} \approx 1 + 2\,\frac{(\boldsymbol{r_{1L}}\cdot\boldsymbol{x})}{||\boldsymbol{r_{1L}}||^2}
\tag{2.9}
$$

Substitute Equation 2.9 in the final expression of Equation 2.8, then apply binomial expansion to first order.

$$
\begin{aligned}
\left\{ \frac{1}{||\boldsymbol{r_{1F}}||^3} - \frac{1}{||\boldsymbol{r_{1L}}||^3} \right\} &\approx \left\{ \left[1 + 2\,\frac{(\boldsymbol{r_{1L}}\cdot\boldsymbol{x})}{||\boldsymbol{r_{1L}}||^2} \right]^{-3/2} - 1 \right\} ||\boldsymbol{r_{1L}}||^{-3} \\
&= \left\{ \left[1 + \left(-\tfrac{3}{2}\right)\left(2\,\frac{(\boldsymbol{r_{1L}}\cdot\boldsymbol{x})}{||\boldsymbol{r_{1L}}||^2}\right) + H.O.T. \right] - 1 \right\} ||\boldsymbol{r_{1L}}||^{-3} \\
&\approx -3\,(\boldsymbol{r_{1L}} \cdot \boldsymbol{x})||\boldsymbol{r_{1L}}||^{-5}
\end{aligned}
\tag{2.10}
$$

Likewise:

$$
\left\{ \frac{1}{||\boldsymbol{r_{2F}}||^3} - \frac{1}{||\boldsymbol{r_{2L}}||^3} \right\} \approx -3\,(\boldsymbol{r_{2L}} \cdot \boldsymbol{x})||\boldsymbol{r_{2L}}||^{-5}
\tag{2.11}
$$

Combining Equations 2.10 and 2.11 yields.

$$\left\{ \frac{\mu_1}{||\boldsymbol{r_{1F}}||^3} + \frac{\mu_2}{||\boldsymbol{r_{2F}}||^3} \right\} \approx \frac{\mu_1}{||\boldsymbol{r_{1L}}||^3} \left[1 - \frac{3\,(\boldsymbol{r_{1L}} \cdot \boldsymbol{x})}{||\boldsymbol{r_{1L}}||^2} \right] + \frac{\mu_2}{||\boldsymbol{r_{2L}}||^3} \left[1 - \frac{3\,(\boldsymbol{r_{2L}} \cdot \boldsymbol{x})}{||\boldsymbol{r_{2L}}||^2} \right] \qquad (2.12)$$

Substituting Equations 2.10, 2.11 and 2.12 into Equation 2.7.

$$\begin{aligned}
\ddot{\boldsymbol{x}} \approx &-\left\{ \frac{\mu_1}{||\boldsymbol{r_{1L}}||^3} \left[1 - \frac{3\,(\boldsymbol{r_{1L}} \cdot \boldsymbol{x})}{||\boldsymbol{r_{1L}}||^2} \right] + \frac{\mu_2}{||\boldsymbol{r_{2L}}||^3} \left[1 - \frac{3\,(\boldsymbol{r_{2L}} \cdot \boldsymbol{x})}{||\boldsymbol{r_{2L}}||^2} \right] \right\} \boldsymbol{x} \\
&+ \left\{ 3\, \frac{\mu_1}{||\boldsymbol{r_{1L}}||^5}(\boldsymbol{r_{1L}} \cdot \boldsymbol{x}) \right\} \boldsymbol{r_{1L}} + \left\{ 3\, \frac{\mu_2}{||\boldsymbol{r_{2L}}||^5}(\boldsymbol{r_{2L}} \cdot \boldsymbol{x}) \right\} \boldsymbol{r_{2L}} \qquad (2.13) \\
&+ \boldsymbol{u_{thrust,F}}
\end{aligned}$$

Note: $(\boldsymbol{r_{1L}} \cdot \boldsymbol{x})\,\boldsymbol{r_{1L}} = \boldsymbol{r_{1L}}\,(\boldsymbol{r_{1L}}^\mathsf{T}\,\boldsymbol{x}) = [\boldsymbol{r_{1L}}\,\boldsymbol{r_{1L}}^\mathsf{T}]\,\boldsymbol{x}$

Rewrite Equation 2.13 as:

$$\begin{aligned}
\ddot{\boldsymbol{x}} \approx &-\left\{ \frac{\mu_1}{||\boldsymbol{r_{1L}}||^3} \left[1 - \frac{3\,(\boldsymbol{r_{1L}} \cdot \boldsymbol{x})}{||\boldsymbol{r_{1L}}||^2} \right] + \frac{\mu_2}{||\boldsymbol{r_{2L}}||^3} \left[1 - \frac{3\,(\boldsymbol{r_{2L}} \cdot \boldsymbol{x})}{||\boldsymbol{r_{2L}}||^2} \right] \right\} \boldsymbol{x} \\
&+ 3\, \frac{\mu_1}{||\boldsymbol{r_{1L}}||^5} \left\{ [\boldsymbol{r_{1L}}\,\boldsymbol{r_{1L}}^\mathsf{T}]\,\boldsymbol{x} \right\} + 3\, \frac{\mu_2}{||\boldsymbol{r_{2L}}||^5} \left\{ [\boldsymbol{r_{2L}}\,\boldsymbol{r_{2L}}^\mathsf{T}]\,\boldsymbol{x} \right\} \\
&+ \boldsymbol{u_{thrust,F}} \\
= &\left\{ -\left(\frac{\mu_1}{||\boldsymbol{r_{1L}}||^3} \left[1 - \frac{3\,(\boldsymbol{r_{1L}} \cdot \boldsymbol{x})}{||\boldsymbol{r_{1L}}||^2} \right] + \frac{\mu_2}{||\boldsymbol{r_{2L}}||^3} \left[1 - \frac{3\,(\boldsymbol{r_{2L}} \cdot \boldsymbol{x})}{||\boldsymbol{r_{2L}}||^2} \right] \right) \mathbf{I_3} \right. \qquad (2.14) \\
&\left. + 3\, \frac{\mu_1}{||\boldsymbol{r_{1L}}||^5} [\boldsymbol{r_{1L}}\,\boldsymbol{r_{1L}}^\mathsf{T}] + 3\, \frac{\mu_2}{||\boldsymbol{r_{2L}}||^5} [\boldsymbol{r_{2L}}\,\boldsymbol{r_{2L}}^\mathsf{T}] \right\} \boldsymbol{x} \\
&+ \boldsymbol{u_{thrust,F}}
\end{aligned}$$

In summary the linearized dynamics are expressed as:

$$\ddot{\boldsymbol{x}} = {}^{I}\boldsymbol{\Xi}(t)\,\boldsymbol{x} + \boldsymbol{u_{thrust,F}} \qquad (2.15)$$

Where:

$$\begin{aligned}
{}^{I}\boldsymbol{\Xi}(t) = &\left\{ -\left(\frac{\mu_1}{||\boldsymbol{r_{1L}}||^3} \left[1 - \frac{3\,(\boldsymbol{r_{1L}} \cdot \boldsymbol{x})}{||\boldsymbol{r_{1L}}||^2} \right] + \frac{\mu_2}{||\boldsymbol{r_{2L}}||^3} \left[1 - \frac{3\,(\boldsymbol{r_{2L}} \cdot \boldsymbol{x})}{||\boldsymbol{r_{2L}}||^2} \right] \right) \mathbf{I_3} \right. \\
&\left. + 3\, \frac{\mu_1}{||\boldsymbol{r_{1L}}||^5} [\boldsymbol{r_{1L}}\,\boldsymbol{r_{1L}}^\mathsf{T}] + 3\, \frac{\mu_2}{||\boldsymbol{r_{2L}}||^5} [\boldsymbol{r_{2L}}\,\boldsymbol{r_{2L}}^\mathsf{T}] \right\} \\
= &\left\{ -\left(\frac{\mu_1}{||\boldsymbol{r_{1L}}||^3} \left[1 - \frac{3\,(\boldsymbol{r_{1L}} \cdot \boldsymbol{x})}{||\boldsymbol{r_{1L}}||^2} \right] + \frac{\mu_2}{||\boldsymbol{r_{2L}}||^3} \left[1 - \frac{3\,(\boldsymbol{r_{2L}} \cdot \boldsymbol{x})}{||\boldsymbol{r_{2L}}||^2} \right] \right) \mathbf{I_3} \right. \\
&\left. + \frac{3\,\mu_1}{||\boldsymbol{r_{1L}}||^3} [\boldsymbol{e_{1L}}\,\boldsymbol{e_{1L}}^\mathsf{T}] + \frac{3\,\mu_2}{||\boldsymbol{r_{2L}}||^3} [\boldsymbol{e_{2L}}\,\boldsymbol{e_{2L}}^\mathsf{T}] \right\}
\end{aligned}$$

Note: $\boldsymbol{e}_{1L}$ and $\boldsymbol{e}_{2L}$ denote unit vectors along $\boldsymbol{r}_{1L}$ and $\boldsymbol{r}_{2L}$, respectively.

Finally, recalling the assumption, $||\boldsymbol{x}|| \ll ||\boldsymbol{r}_{1L}||$ and $||\boldsymbol{x}|| \ll ||\boldsymbol{r}_{2L}||$, Equation 2.15 becomes:

$$
{}^{I}\boldsymbol{\Xi}(t) = \left\{ -\left(\frac{\mu_1}{||\boldsymbol{r}_{1L}||^3} + \frac{\mu_2}{||\boldsymbol{r}_{2L}||^3} \right) \mathbf{I_3} + \frac{3\,\mu_1}{||\boldsymbol{r}_{1L}||^3} \left[\boldsymbol{e}_{1L}\ \boldsymbol{e}_{1L}{}^{\mathsf{T}} \right] \right.
$$
$$
\left. + \frac{3\,\mu_2}{||\boldsymbol{r}_{2L}||^3} \left[\boldsymbol{e}_{2L}\ \boldsymbol{e}_{2L}{}^{\mathsf{T}} \right] \right\} \tag{2.16}
$$

Note: The time variation in ${}^{I}\boldsymbol{\Xi}(t)$ are due to the relatively slow variation in the location of the Leader spacecraft relative to the two primaries of the RTBP.

For convenience, the expression for ${}^{I}\boldsymbol{\Xi}(t)$ is consolidated in terms of coefficients $c_1(t)$ and $c_2(t)$.

$$
{}^{I}\boldsymbol{\Xi}(t) = \left\{ -(c_1(t) + c_2(t)) \mathbf{I_3} + 3\,c_1(t) \left[\boldsymbol{e}_{1L}(t)\, \boldsymbol{e}_{1L}(t)^{\mathsf{T}} \right] + 3\,c_2(t) \left[\boldsymbol{e}_{2L}(t)\, \boldsymbol{e}_{2L}(t)^{\mathsf{T}} \right] \right\}
$$
$$
c_1(t) = \mu_1 ||\boldsymbol{r}_{1L}(t)||^{-3}
$$
$$
c_2(t) = \mu_2 ||\boldsymbol{r}_{2L}(t)||^{-3}
$$

$$(2.17)$$

The linearized dynamics (inertial coordinates) in matrix form are:

$$
\begin{bmatrix} \dot{\boldsymbol{x}} \\ \ddot{\boldsymbol{x}} \end{bmatrix} = \begin{bmatrix} \mathbf{0} & \mathbf{I_3} \\ {}^{I}\boldsymbol{\Xi}(t) & \mathbf{0} \end{bmatrix} \begin{bmatrix} \boldsymbol{x} \\ \dot{\boldsymbol{x}} \end{bmatrix} + \begin{bmatrix} \mathbf{0} \\ \mathbf{I_3} \end{bmatrix} \boldsymbol{u}_{thrust,F} \tag{2.18}
$$

2.1.2.1   Dynamics in Rotational Frame/Validation

It is instructive to compare the general derivation above with the (simpler) known linearized solutions for the CRTBP at a Libration Point. If valid, evaluating Equation 2.18 with the Leader located at one of the equilibrium points must yield

the same linearized dynamics. Expressing the dynamics in the rotating CRTBP frame is the first step.

Let $\boldsymbol{D}_{RI}(t)$ express the transformation of a vector from the inertial frame to the RTBP rotating frame. Assuming all terms are differentiable, the following expressions relate position, velocity and acceleration between the two frames.

$$
\begin{aligned}
{}^{I}\boldsymbol{x} &= \boldsymbol{D}_{RI}(t)^{\mathsf{T}}\,{}^{R}\boldsymbol{x} \\
{}^{I}\dot{\boldsymbol{x}} &= \dot{\boldsymbol{D}}_{RI}(t)^{\mathsf{T}}\,{}^{R}\boldsymbol{x} + \boldsymbol{D}_{RI}(t)^{\mathsf{T}}\,{}^{R}\dot{\boldsymbol{x}} \\
{}^{I}\ddot{\boldsymbol{x}} &= \ddot{\boldsymbol{D}}_{RI}(t)^{\mathsf{T}}\,{}^{R}\boldsymbol{x} + 2\,\dot{\boldsymbol{D}}_{RI}(t)^{\mathsf{T}}\,{}^{R}\dot{\boldsymbol{x}} + \boldsymbol{D}_{RI}(t)^{\mathsf{T}}\,{}^{R}\ddot{\boldsymbol{x}}
\end{aligned}
\tag{2.19}
$$

Equation 2.19 requires the kinematics of $\boldsymbol{D}_{RI}(t)$, expressed as:

$$
\begin{aligned}
\dot{\boldsymbol{D}}_{RI}(t) &= -[n\times]\boldsymbol{D}_{RI}(t) \\
\ddot{\boldsymbol{D}}_{RI}(t) &= -[\dot{n}\times]\boldsymbol{D}_{RI}(t) + [n\times][n\times]\boldsymbol{D}_{RI}(t)
\end{aligned}
\tag{2.20}
$$

$'n'$ represents the angular rate of the rotating frame, depicted in Figure 2.4. $[n\times]$ is the skew symmetric matrix formed by the vector, n, defined so that the expression $[\boldsymbol{x}\times]\,\boldsymbol{y}$, is the cross product equivalent of: $\boldsymbol{x} \times \boldsymbol{y}$.

Combining Equations 2.18 and 2.19:

$$
\begin{bmatrix} {}^{R}\dot{\boldsymbol{x}} \\[2mm] {}^{R}\ddot{\boldsymbol{x}} \end{bmatrix}
=
\begin{bmatrix} \boldsymbol{0} & \mathbf{I_3} \\[2mm] \{{}^{R}\boldsymbol{\Xi}(t) - \boldsymbol{D}_{RI}(t)\ddot{\boldsymbol{D}}_{RI}(t)^{\mathsf{T}}\} & \{-2\,\boldsymbol{D}_{RI}(t)\dot{\boldsymbol{D}}_{RI}(t)^{\mathsf{T}}\} \end{bmatrix}
\begin{bmatrix} {}^{R}\boldsymbol{x} \\[2mm] {}^{R}\dot{\boldsymbol{x}} \end{bmatrix}
$$

$$
+ \begin{bmatrix} \boldsymbol{0} \\[2mm] \mathbf{I_3} \end{bmatrix} {}^{R}\boldsymbol{u}_{thrust,F}
\tag{2.21}
$$

Where:

$$
\begin{aligned}
{}^{R}\boldsymbol{\Xi}(t) &= \{\boldsymbol{D}_{RI}(t)\,{}^{I}\boldsymbol{\Xi}(t)\,\boldsymbol{D}_{RI}(t)^{\mathsf{T}}\} \\[2mm]
&= -\left(\frac{\mu_1}{\|\boldsymbol{r_{1L}}\|^3} + \frac{\mu_2}{\|\boldsymbol{r_{2L}}\|^3}\right)\mathbf{I_3} + \frac{3\,\mu_1}{\|\boldsymbol{r_{1L}}\|^3}\left[{}^{R}\boldsymbol{e_{1L}}\;{}^{R}\boldsymbol{e_{1L}}^{\mathsf{T}}\right] \\[2mm]
&\quad + \frac{3\,\mu_2}{\|\boldsymbol{r_{2L}}\|^3}\left[{}^{R}\boldsymbol{e_{2L}}\;{}^{R}\boldsymbol{e_{2L}}^{\mathsf{T}}\right]
\end{aligned}
$$

Combining Equations 2.20 and 2.21, and noting $[n\times]^{\mathsf{T}} = -[n\times]$:

$$
\begin{bmatrix} {}^{R}\dot{\boldsymbol{x}} \\[2mm] {}^{R}\ddot{\boldsymbol{x}} \end{bmatrix}
=
\begin{bmatrix} \boldsymbol{0} & \mathbf{I_3} \\[2mm] \{{}^{R}\boldsymbol{\Xi}(t) + [\dot{n}\times] - [n\times][n\times]\} & -2\,[n\times] \end{bmatrix}
\begin{bmatrix} {}^{R}\boldsymbol{x} \\[2mm] {}^{R}\dot{\boldsymbol{x}} \end{bmatrix}
$$

$$
+ \begin{bmatrix} \boldsymbol{0} \\[2mm] \mathbf{I_3} \end{bmatrix} {}^{R}\boldsymbol{u}_{thrust,F}
\tag{2.22}
$$

For the CRTBP, $\dot{n} = 0$, simplifying Equation 2.22:

$$
\begin{bmatrix} {}^{R}\dot{\boldsymbol{x}} \\[2mm] {}^{R}\ddot{\boldsymbol{x}} \end{bmatrix}
=
\begin{bmatrix} \boldsymbol{0} & \mathbf{I_3} \\[2mm] \{{}^{R}\boldsymbol{\Xi}(t) - [n\times][n\times]\} & -2\,[n\times] \end{bmatrix}
\begin{bmatrix} {}^{R}\boldsymbol{x} \\[2mm] {}^{R}\dot{\boldsymbol{x}} \end{bmatrix}
+ \begin{bmatrix} \boldsymbol{0} \\[2mm] \mathbf{I_3} \end{bmatrix} {}^{R}\boldsymbol{u}_{thrust,F}
\tag{2.23}
$$

44

$$
{}^{R}\boldsymbol{\Xi}(t) = -\left(\frac{\mu_1}{||\boldsymbol{r_{1L}}||^3} + \frac{\mu_2}{||\boldsymbol{r_{2L}}||^3}\right)\mathbf{I_3} + \frac{3\,\mu_1}{||\boldsymbol{r_{1L}}||^3}\left[{}^{R}\boldsymbol{e_{1L}}\ {}^{R}\boldsymbol{e_{1L}}^{\mathsf{T}}\right] + \frac{3\,\mu_2}{||\boldsymbol{r_{2L}}||^3}\left[{}^{R}\boldsymbol{e_{2L}}\ {}^{R}\boldsymbol{e_{2L}}^{\mathsf{T}}\right]
$$

2.1.2.2   Linearization with Leader at a Collinear Libration Point

Using the dimensionless parameters of the CRTBP, the Leader is placed at one of the Collinear Points, $\mu_1 = (1 - \rho)$ and $\mu_2 = \rho$. Also, the unit vectors, ${}^{R}\boldsymbol{e_{1L}}$ and ${}^{R}\boldsymbol{e_{2L}}$, lie along the X-axis. The coordinates are $[X_0, 0, 0]$. Ranges to the primary masses are: $||\boldsymbol{r_{1L}}|| = X_0 - \rho$ and $||\boldsymbol{r_{2L}}|| = X_0 + 1 - \rho$. The angular rate, $'n'$, has a value of unity, and is directed along the Z-axis. Therefore:

$$
\left[{}^{R}\boldsymbol{e_{1L}}\ {}^{R}\boldsymbol{e_{1L}}^{\mathsf{T}}\right] = \left[{}^{R}\boldsymbol{e_{2L}}\ {}^{R}\boldsymbol{e_{2L}}^{\mathsf{T}}\right] = \begin{bmatrix} 1 & 0 & 0 \\ 0 & 0 & 0 \\ 0 & 0 & 0 \end{bmatrix} ; [n\times][n\times] = \begin{bmatrix} -1 & 0 & 0 \\ 0 & -1 & 0 \\ 0 & 0 & 0 \end{bmatrix}
$$

$$
\sigma \equiv \left(\frac{\mu_1}{||\boldsymbol{r_{1L}}||^3} + \frac{\mu_2}{||\boldsymbol{r_{2L}}||^3}\right) = \left(\frac{(1-\rho)}{(X_0-\rho)^3} + \frac{\rho}{(X_0+1-\rho)^3}\right)
$$

Substituting the expressions into Equation 2.23, and neglecting the control force, yields:

$$
\begin{bmatrix} \dot{x} \\ \dot{y} \\ \dot{z} \\ \ddot{x} \\ \ddot{y} \\ \ddot{z} \end{bmatrix} = \begin{bmatrix} 0 & 0 & 0 & 1 & 0 & 0 \\ 0 & 0 & 0 & 0 & 1 & 0 \\ 0 & 0 & 0 & 0 & 0 & 1 \\ (2\sigma+1) & 0 & 0 & 0 & 2 & 0 \\ 0 & -(\sigma-1) & 0 & -2 & 0 & 0 \\ 0 & 0 & -(\sigma-1) & 0 & 0 & 0 \end{bmatrix} \begin{bmatrix} x \\ y \\ z \\ \dot{x} \\ \dot{y} \\ \dot{z} \end{bmatrix}
\tag{2.24}
$$

The result, Equation 2.24, is identical to the linearized dynamics at the Collinear Libration Points, expressed in Equation 2.6 for the X-Y plane motion, and Equation 2.4 for the Z-axis motion. A similar analysis demonstrates the equivalence of the linearized equations of motion near the Triangular Libration Points.

2.1.2.3 Linearization with a Single Primary Mass

Another interesting simplification verifies that the general linearized equations of relative motion, Equations 2.17 and 2.18, collapse, as a special case, to the well known Hill's (Chlohessy-Wiltshire) equations of relative motion. Hill's equations are linearized equations of motion about a reference mass in a circular orbit about a single, central mass. The coordinate frame is defined with the X-axis in the radial direction, the Y-Axis along the instantaneous velocity vector, and the Z-axis completes the triad of the right-handed coordinate frame. Equation 2.23 provides an appropriate starting point, repeated here for reference.

$$
\begin{bmatrix} {}^{R}\dot{\boldsymbol{x}} \\ {}^{R}\ddot{\boldsymbol{x}} \end{bmatrix} = \begin{bmatrix} \mathbf{0} & \mathbf{I_3} \\ \{{}^{R}\boldsymbol{\Xi}(t) - [n\times][n\times]\} & -2\,[n\times] \end{bmatrix} \begin{bmatrix} {}^{R}\boldsymbol{x} \\ {}^{R}\dot{\boldsymbol{x}} \end{bmatrix} + \begin{bmatrix} \mathbf{0} \\ \mathbf{I_3} \end{bmatrix} {}^{R}\boldsymbol{u}_{thrust,F}
$$

$$
{}^{R}\boldsymbol{\Xi}(t) = -\left(\frac{\mu_1}{\|\boldsymbol{r_{1L}}\|^3} + \frac{\mu_2}{\|\boldsymbol{r_{2L}}\|^3} \right) \mathbf{I_3} + \frac{3\,\mu_1}{\|\boldsymbol{r_{1L}}\|^3} \left[{}^{R}\boldsymbol{e_{1L}} \, {}^{R}\boldsymbol{e_{1L}}^{\mathsf{T}} \right] + \frac{3\,\mu_2}{\|\boldsymbol{r_{2L}}\|^3} \left[{}^{R}\boldsymbol{e_{2L}} \, {}^{R}\boldsymbol{e_{2L}}^{\mathsf{T}} \right]
$$

Transform the equation by setting $\mu_2 = 0$, and define $'n'$ as the orbital rate, $n = \sqrt{\frac{\mu_1}{||\boldsymbol{r_{1L}}||^3}}$. Then:

$$\begin{bmatrix} ^R\dot{\boldsymbol{x}} \\ \\ ^R\ddot{\boldsymbol{x}} \end{bmatrix} = \begin{bmatrix} \mathbf{0} & \mathbf{I_3} \\ \\ \{^R\boldsymbol{\Xi}(t) - [n\times][n\times]\} & -2\,[n\times] \end{bmatrix} \begin{bmatrix} ^R\boldsymbol{x} \\ \\ ^R\dot{\boldsymbol{x}} \end{bmatrix} + \begin{bmatrix} \mathbf{0} \\ \\ \mathbf{I_3} \end{bmatrix} {}^R\boldsymbol{u}_{thrust,F}$$

$$^R\boldsymbol{\Xi}(t) = -n^2\,\mathbf{I_3} + 3n^2\,[{}^R\boldsymbol{e_{1L}}\ {}^R\boldsymbol{e_{1L}}{}^\mathsf{T}]$$

With:

$$[{}^R\boldsymbol{e_{1L}}\ {}^R\boldsymbol{e_{1L}}{}^\mathsf{T}] = \begin{bmatrix} 1 & 0 & 0 \\ 0 & 0 & 0 \\ 0 & 0 & 0 \end{bmatrix} ; [n\times] = \begin{bmatrix} 0 & -n & 0 \\ n & 0 & 0 \\ 0 & 0 & 0 \end{bmatrix} ; [n\times][n\times] = \begin{bmatrix} -n^2 & 0 & 0 \\ 0 & -n^2 & 0 \\ 0 & 0 & 0 \end{bmatrix}$$

Consolidating the expression yields Hill's (Chlohessy-Wiltshire) Equations, as expected.

$$\begin{bmatrix} \dot{x} \\ \dot{y} \\ \dot{z} \\ \ddot{x} \\ \ddot{y} \\ \ddot{z} \end{bmatrix} = \begin{bmatrix} 0 & 0 & 0 & 1 & 0 & 0 \\ 0 & 0 & 0 & 0 & 1 & 0 \\ 0 & 0 & 0 & 0 & 0 & 1 \\ 3n^2 & 0 & 0 & 0 & 2n & 0 \\ 0 & 0 & 0 & -2n & 0 & 0 \\ 0 & 0 & -n^2 & 0 & 0 & 0 \end{bmatrix} \begin{bmatrix} x \\ y \\ z \\ \dot{x} \\ \dot{y} \\ \dot{z} \end{bmatrix} \tag{2.25}$$

2.1.3 Dynamics of the Earth/Moon-Sun System

As introduced at the beginning of this section, the goal is to model the dynamics of a two spacecraft formation operating in the gravity environment of

the Earth/Moon-Sun, Figure 2.5. The Leader spacecraft is assumed to follow a ballistic trajectory with infrequent control for orbit maintenance. Control is applied to the Follower spacecraft to maintain a specified trajectory relative to the Leader spacecraft.
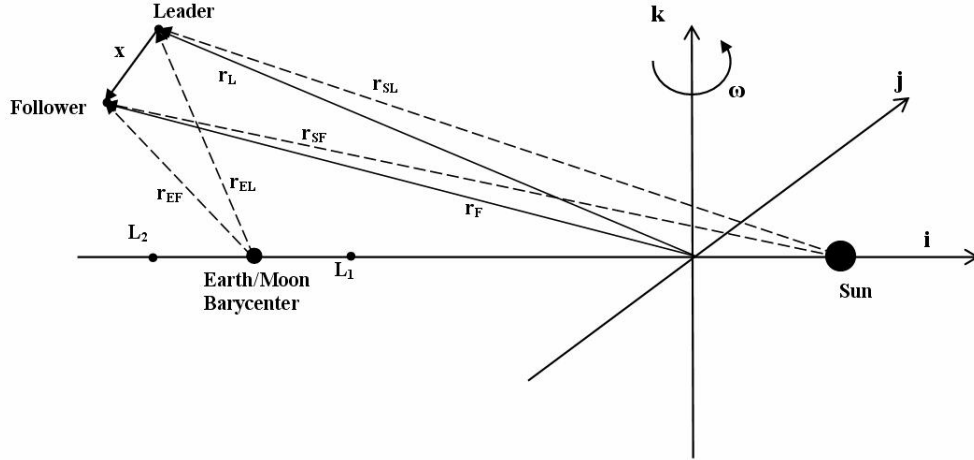
Figure 2.5: Two Spacecraft Orbiting in the Earth/Moon - Sun Rotating Frame

2.1.3.1   Unperturbed Model

The principal gravitational sources are the Earth/Moon system and the Sun. Perturbing forces, introduced by differential solar pressure and other gravitational sources, are neglected for the moment. Based on reference vectors shown in Figure 2.5 and Equation 2.7, the relative dynamics of the Follower spacecraft referenced to the Leader are given by:

$$\ddot{\boldsymbol{x}} = -\left\{\frac{\mu_{em}}{||\boldsymbol{r_{EF}}||^3} + \frac{\mu_s}{||\boldsymbol{r_{SF}}||^3}\right\}\boldsymbol{x} - \mu_{em}\left\{\frac{1}{||\boldsymbol{r_{EF}}||^3} - \frac{1}{||\boldsymbol{r_{EL}}||^3}\right\}\boldsymbol{r_{EL}}$$
$$-\mu_s\left\{\frac{1}{||\boldsymbol{r_{SF}}||^3} - \frac{1}{||\boldsymbol{r_{SL}}||^3}\right\}\boldsymbol{r_{SL}} + \boldsymbol{u_{thrust,F}}$$

$$(2.26)$$

Where:

$\boldsymbol{r}_{\#\#}$ –   Position vectors, depicted in Figure 2.5

μ_{em} –   Gravitational Parameter for Earth/Moon

μ_s –   Gravitational Parameter for Sun

$\boldsymbol{u_{thrust,F}}$ –   External control force per unit mass applied to Follower

         spacecraft

Equation (2.26) provides an exact expression of the dynamics of unperturbed relative motion between the Follower and Leader spacecraft.

2.1.3.2 Perturbed Model

As mentioned, the dynamics represented by Equation (2.26) are perturbed by forces associated with differential solar pressure and other gravitational sources.

Solar radiation generates a net force and torque on a spacecraft dependent on the spacecraft geometry and surface reflectivity. In the most general case the net force and torque are dependent on the spacecraft attitude. However for this analysis the center of solar pressure is assumed to be aligned with the spacecraft center of mass, resulting in zero net torque. Thus, a detailed discussion of solar torque is omitted. Also, the spacecraft profile, and thus the solar pressure force, are assumed attitude independent. The net force per unit mass generated by solar pressure is

expressed as:

$$\boldsymbol{f_{Solar}} = \frac{F_{Solar}}{S/C\ Mass} = Cr\ \frac{S/C\ Area}{S/C\ Mass}\ (SolarFlux)\ \boldsymbol{e_{Sun\ to\ S/C}} \qquad (2.27)$$

Where:

Cr –   Spacecraft Coefficient of Reflectivity,

1 - perfectly absorbing, 2 - perfectly reflective

$(SolarFlux)$ –   Solar flux at spacecraft position, $(4.5 \times 10^{-6}N/m^2)/D^2$,

D - distance from Sun in astronomical units.

$\boldsymbol{e_{Sun\ to\ S/C}}$ –   Unit vector point from the Sun to the S/C position

The differential acceleration due to solar pressure of the Follower spacecraft relative to the Leader is expressed as:

$$\boldsymbol{\Delta f_{solar}} = \boldsymbol{f_{solar,Follower}} - \boldsymbol{f_{solar,Leader}} \qquad (2.28)$$

The other principal perturbing force is generated by unmodeled gravitational sources, i.e. the other planets. The full n-body gravitational model for relative motion is expressed as:

$$\begin{aligned}
\ddot{\boldsymbol{r}}_F &= -\mu_1 \frac{\boldsymbol{r_{1F}}}{||\boldsymbol{r_{1F}}||^3} - \mu_2 \frac{\boldsymbol{r_{2F}}}{||\boldsymbol{r_{2F}}||^3} - \sum_{i=3}^{n} \mu_i \frac{\boldsymbol{r_{iF}}}{||\boldsymbol{r_{iF}}||^3} + \boldsymbol{u_{thrust,F}} \\
\ddot{\boldsymbol{r}}_L &= -\mu_1 \frac{\boldsymbol{r_{1L}}}{||\boldsymbol{r_{1L}}||^3} - \mu_2 \frac{\boldsymbol{r_{2L}}}{||\boldsymbol{r_{2L}}||^3} - \sum_{i=3}^{n} \mu_i \frac{\boldsymbol{r_{iL}}}{||\boldsymbol{r_{iL}}||^3} \\
\ddot{\boldsymbol{x}} &= -\mu_1 \left(\frac{\boldsymbol{r_{1F}}}{||\boldsymbol{r_{1F}}||^3} - \frac{\boldsymbol{r_{1L}}}{||\boldsymbol{r_{1L}}||^3} \right) - \mu_2 \left(\frac{\boldsymbol{r_{2F}}}{||\boldsymbol{r_{2F}}||^3} - \frac{\boldsymbol{r_{2L}}}{||\boldsymbol{r_{2L}}||^3} \right) \\
&\quad - \sum_{i=3}^{n} \mu_i \left(\frac{\boldsymbol{r_{iF}}}{||\boldsymbol{r_{iF}}||^3} - \frac{\boldsymbol{r_{iL}}}{||\boldsymbol{r_{iL}}||^3} \right) + \boldsymbol{u_{thrust,F}}
\end{aligned} \qquad (2.29)$$

Comparing Equations 2.7 and 2.29, the unmodeled differential gravitational acceleration is given by:

$$\boldsymbol{\Delta f}_{pert} \quad = \quad -\sum_{i=0}^{n} \mu_i \left(\frac{\boldsymbol{r}_{iF}}{||\boldsymbol{r}_{iF}||^3} - \frac{\boldsymbol{r}_{iL}}{||\boldsymbol{r}_{iL}||^3} \right) \tag{2.30}$$

Alternatively, the linearized model can be extended to include the full n-body gravitational model. Following the derivation of Equations 2.15 and 2.16 the linearized dynamics for the n-body problem are expressed as:

$$
\begin{aligned}
\ddot{\boldsymbol{x}} \;&= -\sum_{i=1}^{n} \mu_i \left(\frac{\boldsymbol{r}_{iF}}{||\boldsymbol{r}_{iF}||^3} - \frac{\boldsymbol{r}_{iL}}{||\boldsymbol{r}_{iL}||^3} \right) + \boldsymbol{u}_{thrust,F} \\
&= -\sum_{i=1}^{n} \mu_i \left\{ \left(\frac{\boldsymbol{r}_{iF}}{||\boldsymbol{r}_{iF}||^3} - \frac{\boldsymbol{r}_{iL}}{||\boldsymbol{r}_{iF}||^3} \right) \right\} - \sum_{i=1}^{n} \left\{ \mu_i \left(\frac{\boldsymbol{r}_{iL}}{||\boldsymbol{r}_{iL}||^3} - \frac{\boldsymbol{r}_{iL}}{||\boldsymbol{r}_{iF}||^3} \right) \right\} + \boldsymbol{u}_{thrust,F} \\
&= -\sum_{i=1}^{n} \mu_i \left\{ \frac{1}{||\boldsymbol{r}_{iF}||^3} \right\} \boldsymbol{x} - \sum_{i=1}^{n} \left\{ \mu_i \left(\frac{1}{||\boldsymbol{r}_{iL}||^3} - \frac{1}{||\boldsymbol{r}_{iF}||^3} \right) \boldsymbol{r}_{iL} \right\} + \boldsymbol{u}_{thrust,F} \\
&\approx {}^{I}\boldsymbol{\Xi}(t)\, \boldsymbol{x} + \boldsymbol{u}_{thrust,F}
\end{aligned}
\tag{2.31}
$$

Where:

$${}^{I}\boldsymbol{\Xi}(t) \;= -\sum_{i=1}^{n} \left\{ \frac{\mu_i}{||\boldsymbol{r}_{iL}||^3} \right\} \mathbf{I_3} + 3 \sum_{i=1}^{n} \left\{ \frac{\mu_i}{||\boldsymbol{r}_{iL}||^3} \left[\boldsymbol{e}_{iL}\ \boldsymbol{e}_{iL}{}^{\mathsf{T}} \right] \right\}$$

Referring ahead to Section 5.3, the magnitude of the third body gravitational effects are small compared to the gravity field of the two primary masses. Therefore, due to the computational expense associated with directly incorporating n-body effects in the linearized model, these effects are treated as a perturbation in the dynamic model.

The unmodeled effects of solar pressure and gravitational perturbations in Equation 2.7, yields modified dynamics expressed as:

$$
\begin{aligned}
\ddot{\boldsymbol{x}} &= -\Big\{ \frac{\mu_{em}}{\|\boldsymbol{r_{EF}}\|^3} + \frac{\mu_s}{\|\boldsymbol{r_{SF}}\|^3} \Big\} \boldsymbol{x} - \mu_{em} \Big\{ \frac{1}{\|\boldsymbol{r_{EF}}\|^3} - \frac{1}{\|\boldsymbol{r_{EL}}\|^3} \Big\} \boldsymbol{r_{EL}} \\
&\quad - \mu_s \Big\{ \frac{1}{\|\boldsymbol{r_{SF}}\|^3} - \frac{1}{\|\boldsymbol{r_{SL}}\|^3} \Big\} \boldsymbol{r_{SL}} + \boldsymbol{\Delta f}_{solar} + \boldsymbol{\Delta f}_{pert} + \boldsymbol{u}_{thrust,F}
\end{aligned}
\tag{2.32}
$$

The nature and magnitude of effects associated with differential solar pressure and unmodeled gravity sources is further discussed in Section 5.1.

Equation 2.32 provides an exact expression of the dynamics of relative motion between the Follower and Leader spacecraft. From Equations 2.17 and 2.18, the linearized dynamics in matrix form are:

$$
\begin{bmatrix} \dot{\boldsymbol{x}} \\ \ddot{\boldsymbol{x}} \end{bmatrix} = \begin{bmatrix} \boldsymbol{0} & \boldsymbol{I_3} \\ {}^{I}\boldsymbol{\Xi}(t) & \boldsymbol{0} \end{bmatrix} \begin{bmatrix} \boldsymbol{x} \\ \dot{\boldsymbol{x}} \end{bmatrix} + \begin{bmatrix} \boldsymbol{0} \\ \boldsymbol{I_3} \end{bmatrix} (\boldsymbol{u}_{thrust,F}) + Perturbations
$$

$$
\tag{2.33}
$$

$$
Pertubations = \begin{bmatrix} \boldsymbol{0} \\ \boldsymbol{I_3} \end{bmatrix} (\boldsymbol{\Delta f}_{solar} + \boldsymbol{\Delta f}_{pert})
$$

2.2 Attitude Dynamics

Spacecraft attitude dynamics and control is the topic of many texts, including [67, 68]. This section provides a general review of rigid body dynamics for completeness.

2.2.1 Dynamics, rigid body - no wheels

The rotational dynamics of a rigid body spacecraft without reaction wheels is given by:

$$\boldsymbol{H_R}\,\dot{\boldsymbol{\omega}} - [\boldsymbol{H_R}\,\boldsymbol{\omega}\times]\,\boldsymbol{\omega}\ = \boldsymbol{\tau} \tag{2.34}$$

Where:

$\boldsymbol{\omega}$ – True Spacecraft Angular Rate

$\boldsymbol{H_R}$ – Spacecraft Moment of Inertia, constant

$\boldsymbol{\tau}$ – Control torque applied to spacecraft

2.2.2 Kinematics

The kinematic equation of motion for a rotating body is given by:

$$\dot{\boldsymbol{q}} = \frac{1}{2}\,\boldsymbol{Q}(\boldsymbol{q})\,\boldsymbol{\omega_{aug}} \tag{2.35}$$

Where:

$\boldsymbol{q} = [\boldsymbol{\varepsilon}\ \eta]^{\mathsf{T}}$ – True Spacecraft Attitude Quaternion

$\boldsymbol{\varepsilon}$ – Vector Component of Attitude Quaternion

η – Scalar Component of Attitude Quaternion

$\boldsymbol{\omega_{aug}} = [\boldsymbol{\omega}\ 0]^{\mathsf{T}}$ – Augmented Rate Vector, Matches Quaternion Dimension

$$\boldsymbol{Q}(\boldsymbol{q}) \quad = \begin{bmatrix} \eta\,\mathbf{I_3} + [\boldsymbol{\varepsilon}\times] & \boldsymbol{\varepsilon} \\[2mm] -\boldsymbol{\varepsilon}^{\mathsf{T}} & \eta \end{bmatrix}$$

2.2.3 Attitude Error

Attitude error is the difference between a true orientation and an actual orientation of a body. Computing the attitude error is not as simple as differencing the quaternions representing the true versus desired attitude. The computation requires quaternion multiplication, $\tilde{q} = [\tilde{\varepsilon} \; \tilde{\eta}]^\mathsf{T} = q \otimes q_d^{-1}$, evaluated as:

$$\tilde{q} = Q(q_d)^\mathsf{T} \, q \tag{2.36}$$

2.2.4 Linearized Equations of Motion

With small body rates and attitude errors, the equations of motion can be expressed in a linear form.

For $\boldsymbol{\omega} \approx 0$, the term $[\boldsymbol{H}_R \, \boldsymbol{\omega} \times] \, \boldsymbol{\omega}$ is neglected as a second order effect, simplifying Equation 2.34 as:

$$\boldsymbol{\tau} = \boldsymbol{H}_R \, \dot{\boldsymbol{\omega}} - [\boldsymbol{H}_R \, \boldsymbol{\omega} \times] \, \boldsymbol{\omega} \approx \boldsymbol{H}_R \, \dot{\boldsymbol{\omega}} \tag{2.37}$$

The next goal is to reduce the kinematic expression of the attitude error to a linear form.

From Equation 2.35 the attitude error kinematics are:

$$\dot{\tilde{q}} = \frac{1}{2} \, Q(\tilde{q}) \, \tilde{\boldsymbol{\omega}}_{aug}$$

Assuming the attitude error is small, the magnitude of the vector component of $\tilde{q}$ is small, $||\tilde{\varepsilon}|| << 1$. Also, the scalar component is approximately one, $\tilde{\eta} \approx 1$. Therefore, for small attitude errors $\boldsymbol{Q}(\tilde{\boldsymbol{q}}) \approx \mathbf{I_4}$, allowing approximation of the attitude kinematics as:

$$\dot{\tilde{q}} \approx \tfrac{1}{2} \tilde{\boldsymbol{\omega}}_{aug} = \tfrac{1}{2} \{\boldsymbol{\omega}_{aug} - \boldsymbol{\omega}_{d,aug}\} \tag{2.38}$$

Equivalently:

$$\dot{\tilde{\varepsilon}} \approx \tfrac{1}{2} \tilde{\boldsymbol{\omega}} = \tfrac{1}{2} \{\boldsymbol{\omega} - \boldsymbol{\omega}_d\}$$

$$\dot{\tilde{\eta}} \approx 0 \tag{2.39}$$

Under the stated assumptions of small rates and small attitude errors, combining Equations 2.37 and 2.39 yields the linearized equations for the error dynamics of rotational motion:

$$\begin{bmatrix} \dot{\tilde{\varepsilon}} \\ \dot{\tilde{\omega}} \end{bmatrix} = \begin{bmatrix} \mathbf{0} & \tfrac{1}{2}\mathbf{I_3} \\ \mathbf{0} & \mathbf{0} \end{bmatrix} \begin{bmatrix} \tilde{\varepsilon} \\ \tilde{\omega} \end{bmatrix} + \begin{bmatrix} \mathbf{0} \\ \boldsymbol{H_R}^{-1} \end{bmatrix} \boldsymbol{\tau} \tag{2.40}$$

2.3   Coupled Orbit and Attitude Dynamics

Control implementation potentially introduces coupling between orbit and attitude dynamics. While an ideal design allows independent orbit and attitude control, real systems experience coupling due to imperfect actuation. For this discussion actuator selection is limited to thrusters, fixed within the body frame of the spacecraft with fully throttleable output. Net thrust and torque on the

spacecraft based on thruster output is expressed as:

$$^{b}U = \begin{bmatrix} \mathbf{R(q)} \, (^{I}\mathbf{u_{thrust,F}}) \\ \\ \boldsymbol{\tau} \end{bmatrix} = B_{thrust} \, F_{thrust} \tag{2.41}$$

Where:

^{b}U – Combined, translation and rotation control in body coordinates

$\mathbf{R(q)}$ – Transformation from inertial to body coordinates

B_{thrust} – Control sensitivity matrix, defined in Equation 2.42

F_{thrust} – Thruster output, $[f_1, f_2, ..., f_n]^T$

$$B_{thrust} = \begin{bmatrix} t_1 & t_2 & \cdots & t_i & \cdots & t_n \\ \\ d_1 \times t_1 & d_2 \times t_2 & \cdots & d_i \times t_i & \cdots & d_n \times t_n \end{bmatrix} \tag{2.42}$$

Where:

t_i – Unit vector in pointing direction of ith thruster, expressed in

S/C body coordinates

d_i – Position vector of ith thruster relative to the S/C center of mass,

expressed in S/C body coordinates

Given a desired, ^{b}U , computation of the corresponding spacecraft thruster output, F_{thrust}, is required. With a sufficient quantity of properly placed thrusters the control sensitivity matrix, B_{thrust}, will have rank six, and thus have a pseudo inverse.

The inverse mapping of Equation 2.41 from $\boldsymbol{B}_{thrust}$ to $\boldsymbol{F}_{thrust}$ is expressed as:

$$\boldsymbol{F}_{thrust} = \boldsymbol{B}_{thrust}^{\mathsf{T}}(\boldsymbol{B}_{thrust}\,\boldsymbol{B}_{thrust}^{\mathsf{T}})^{-1}\,{}^{\mathsf{b}}\mathbf{U} \qquad (2.43)$$

In general, Equation 2.43 yields a thrust vector, $\boldsymbol{F}_{thrust}$, with negative values. However, implementation constrains each element of $\boldsymbol{F}_{thrust}$ be non-negative, assuming fixed thrusters. Therefore, it is necessary to bias the thruster output to guarantee non-negative thrust commands. The topic of thruster biasing is deferred to section 3.4.

Chapter 3

Linear and Nonlinear Nonadaptive Control Theory and Design

Building on the foundation of the dynamics for precision formation flying in Chapter 2, this chapter develops control strategies based both on classical linear control and nonlinear Lyapunov based control theory. As mentioned, the goal is to design a coupled six-degree of freedom (6DOF) control law, addressing both orbital trajectory control and attitude control. Section 3.1 reviews the theoretical basis for various control design methods. Control strategies for formation flying are developed in Sections 3.2 and 3.3. Section 3.2 develops a control algorithm based on linear control theory. Section 3.3 develops a control algorithm based on nonlinear control theory. Control strategies are designed separately for orbit and attitude dynamics. Section 3.4 discusses implementing the combined control laws with a common set of actuators (thrusters).

3.1   Control Theory

This section summarizes basic concepts of both linear and nonlinear control theory. The summary is not exhaustive, nor is it possible to acknowledge the volumes of material published on this topic. Basic texts on linear control theory include: [9, 31, 49, 51, 69]. Texts on the control of nonlinear systems include [29, 33, 58].

3.1.1 Linear Systems

Although real systems manifest nonlinear dynamics, control engineers commonly base designs on linearized dynamics, taking advantage of the strong heritage and rich set of design methods and analysis tools available through linear systems theory. The discussion begins with linear dynamic models followed by a brief discussion of linear control design techniques.

3.1.1.1 State-Space Model

For the general case a dynamic system is represented by the following state space model [51]:

$$\dot{\boldsymbol{x}} = f(\boldsymbol{x}, \boldsymbol{u}, t), \quad \boldsymbol{x}(t_0) = \boldsymbol{x}_0 \tag{3.1}$$

$$\boldsymbol{y} = h(\boldsymbol{x}, \boldsymbol{u}, t) \tag{3.2}$$

Equation (3.1) is the system state equation. Equation (3.2) is the system output equation.

In the case $f(\boldsymbol{x}, \boldsymbol{u}, t)$ and $h(\boldsymbol{x}, \boldsymbol{u}, t)$ are linear functions, the state space model has the form:

$$\dot{\boldsymbol{x}} = \boldsymbol{A}(t)\, \boldsymbol{x} + \boldsymbol{B}(t)\, \boldsymbol{u}, \quad \boldsymbol{x}(t_0) = \boldsymbol{x}_0 \tag{3.3}$$

$$\boldsymbol{y} = \boldsymbol{C}(t)\, \boldsymbol{x} + \boldsymbol{D}(t)\, \boldsymbol{u} \tag{3.4}$$

Real physical systems are most accurately represented by state space models with the form of Equations (3.1) and (3.2). However, the control designer, seeking the advantage of the extensive set of linear control design tools, often prefers a

linear model in the form of Equations (3.3) and (3.4). Therefore, it is necessary to linearize Equations (3.1) and (3.2) about a desired operating point, generating a system model with the form of Equations (3.3) and (3.4). A full discussion of this procedure is provided in [51]. Assuming the system has an equilibrium point for $\boldsymbol{x} = \boldsymbol{0}$ and $\boldsymbol{u} = \boldsymbol{0}$, i.e. $\dot{\boldsymbol{x}} = f(\boldsymbol{0}, \boldsymbol{0}, t) = \boldsymbol{0}$, choose $\boldsymbol{x} = \boldsymbol{0}$ and $\boldsymbol{u} = \boldsymbol{0}$ as a nominal operating state. Form $\boldsymbol{A}(t)$, $\boldsymbol{B}(t)$, $\boldsymbol{C}(t)$ and $\boldsymbol{D}(t)$ with the following Jacobian matrices:

$$\boldsymbol{A}(t) = \left.\frac{\partial f(\boldsymbol{x}, \boldsymbol{u}, t)}{\partial \boldsymbol{x}}\right|_{\boldsymbol{x}=\boldsymbol{0},\ \boldsymbol{u}=\boldsymbol{0}} \qquad \boldsymbol{B}(t) = \left.\frac{\partial f(\boldsymbol{x}, \boldsymbol{u}, t)}{\partial \boldsymbol{u}}\right|_{\boldsymbol{x}=\boldsymbol{0},\ \boldsymbol{u}=\boldsymbol{0}} \tag{3.5}$$

$$\boldsymbol{C}(t) = \left.\frac{\partial h(\boldsymbol{x}, \boldsymbol{u}, t)}{\partial \boldsymbol{x}}\right|_{\boldsymbol{x}=\boldsymbol{0},\ \boldsymbol{u}=\boldsymbol{0}} \qquad \boldsymbol{D}(t) = \left.\frac{\partial h(\boldsymbol{x}, \boldsymbol{u}, t)}{\partial \boldsymbol{u}}\right|_{\boldsymbol{x}=\boldsymbol{0},\ \boldsymbol{u}=\boldsymbol{0}} \tag{3.6}$$

As a further simplification, time dependence of the coefficient matrices is removed by assuming a nominal value, i.e. $\boldsymbol{A} = \boldsymbol{A}(t_0)$, $\boldsymbol{B} = \boldsymbol{B}(t_0)$, $\boldsymbol{C} = \boldsymbol{C}(t_0)$, $\boldsymbol{D} = \boldsymbol{D}(t_0)$. A system with constant coefficients is termed autonomous.

3.1.1.2 Linear System Control Theory

The state space model for an autonomous (time invariant) linear system is expressed as:

$$\dot{\boldsymbol{x}} = \boldsymbol{A}\,\boldsymbol{x} + \boldsymbol{B}\,\boldsymbol{u}, \quad \boldsymbol{x}(t_0) = \boldsymbol{x}_0 \tag{3.7}$$

$$\boldsymbol{y} = \boldsymbol{C}\,\boldsymbol{x} + \boldsymbol{D}\,\boldsymbol{u} \tag{3.8}$$

$\boldsymbol{A}$, $\boldsymbol{B}$, $\boldsymbol{C}$, $\boldsymbol{D}$ are constant.

Numerous complete texts discuss control design methods for linear time invariant (LTI) systems. For this research one method is sufficient to define a

performance baseline for evaluating nonlinear control techniques. The method selected for this discussion is an optimal control technique, linear quadratic control. Again, much is published on this topic. References [13, 31] are the principle sources for this discussion.

The Linear Quadratic Regulator (LQR) design specifies the control input that minimizes a quadratic cost function. Given a time invariant system modeled by Equations (3.7) and (3.8), the cost function is defined as:

$$\mathcal{J}_{cost} = \int_0^T (\tilde{\boldsymbol{x}}^\mathsf{T} \boldsymbol{Q} \tilde{\boldsymbol{x}} \,+\, \boldsymbol{u}^\mathsf{T} \boldsymbol{R} \boldsymbol{u}) dt \tag{3.9}$$

The LQR method specifies the control input, $\boldsymbol{u}$, that minimizes Equation (3.9), based on the design parameters: $\boldsymbol{Q}$ and $\boldsymbol{R}$. These matrices serve as weighting factors for desired system performance. The matrix $\boldsymbol{Q}$ weights the tracking error, $\tilde{\boldsymbol{x}}$. The matrix $\boldsymbol{R}$ weights the control effort. Both, $\boldsymbol{R}$ and $\boldsymbol{Q}$ are symmetric, positive definite matrices. The solution specifies $\boldsymbol{u}$ as:

$$\boldsymbol{u} = -\boldsymbol{K}\,\tilde{\boldsymbol{x}}, \qquad \boldsymbol{K} = \boldsymbol{R}^{-1}\,\boldsymbol{B}^\mathsf{T}\,\boldsymbol{M} \tag{3.10}$$

Where $\boldsymbol{M}$ solves the following algebraic matrix Riccati equation:

$$\boldsymbol{M}\,\boldsymbol{A} + \boldsymbol{A}^\mathsf{T}\,\boldsymbol{M} - \boldsymbol{M}\,\boldsymbol{B}\,\boldsymbol{R}^{-1}\,\boldsymbol{B}^\mathsf{T}\,\boldsymbol{M} = -\boldsymbol{Q} \tag{3.11}$$

The existence of the solution depends on the characteristics of the system model. Specifically, the system must be stabilizable and detectable.[13] A system is stabilizable and detectable if all unstable modes are controllable and observable. Controllability implies that a control input can be specified to drive the system to any state within a finite time. Observability implies the system output contains

sufficient information to determine the state of the system. Formal definition of these terms appear in most of the cited texts on linear control theory.

3.1.2 Lyapunov Based Nonlinear Control

Nonlinear control strategy exploits the natural form of the system dynamics, derived from either Hamiltonian or Euler-Lagrange dynamics. Lyapunov based nonlinear control generates a linear response to the error dynamics while capitalizing on the natural form of system dynamics. Lyapunov theory provides the framework for analyzing the system response and stability for the control design. For a detailed discussion of this method refer to [58].

3.1.2.1 Dynamics Model

The dynamics and kinematics for most physical systems can be expressed in the following form, based on Hamiltonian or Euler-Lagrange dynamics.

$$\text{Dynamics: } \boldsymbol{H}(\boldsymbol{\xi})\, \dot{\boldsymbol{\nu}} + \boldsymbol{C}(\boldsymbol{\xi}, \boldsymbol{\nu})\, \boldsymbol{\nu} + \boldsymbol{E}(\boldsymbol{\xi}, \boldsymbol{\nu}) = \boldsymbol{u} \tag{3.12}$$

$$\text{Kinematics: } \dot{\boldsymbol{\xi}} = \boldsymbol{J}(\boldsymbol{\xi})\, \boldsymbol{\nu} \tag{3.13}$$

Where:

$\boldsymbol{\xi}$ - General Position Variable

$\boldsymbol{\nu}$ - General Velocity Variable

$\boldsymbol{H}(\boldsymbol{\xi})$ - Mass properties, $\boldsymbol{H}(\boldsymbol{\xi}) = \boldsymbol{H}(\boldsymbol{\xi})^\mathsf{T} > \boldsymbol{0}, \forall\, \boldsymbol{\xi}$

$\boldsymbol{C}(\boldsymbol{\xi}, \boldsymbol{\nu})$ - Rotational Forces

$\boldsymbol{E}(\boldsymbol{\xi}, \boldsymbol{\nu})$ - Environmental/Damping Forces

$\boldsymbol{u}$ - Input forces/torques

$H(\xi)$ and $C(\xi, \nu)$ are subject to the constraint $[\dot{H}(\xi) - 2\,C(\xi, \nu)]$ is skew, which is a consequence of the law of energy conservation.

With the simplifying assumption, $\dot{\xi} = \nu$, combine Equations 3.12 and 3.13:

$$H(\xi)\,\ddot{\xi} + C(\xi, \dot{\xi})\,\dot{\xi} + E(\xi, \dot{\xi}) = u \tag{3.14}$$

3.1.2.2 Control Design Theory

The control design goal is to specify u, such that the system tracks a desired trajectory, $\xi_d(t)$. The following metrics are defined:

$\tilde{\xi} = (\xi - \xi_d)$, position tracking error

Λ - Design parameter, specified so $\Lambda = \Lambda^{\mathsf{T}} > 0$

$\dot{\xi}_r(t) = \dot{\xi}_d(t) - \Lambda\,\tilde{\xi}$, reference velocity

$s(t) = \dot{\tilde{\xi}} + \Lambda\,\tilde{\xi} = \dot{\xi} - \dot{\xi}_r$, error metric

Then the control law is specified as:

$$u = H(\xi)\,\ddot{\xi}_r + C(\xi, \dot{\xi})\,\dot{\xi}_r + E(\xi, \dot{\xi}) - K_D s$$

$$\text{With the design parameter, } K_D = K_D^{\mathsf{T}} > 0 \tag{3.15}$$

Equating Equations 3.14 and 3.15 yields:

$$u = H(\xi)\,\ddot{\xi}_r + C(\xi, \dot{\xi})\,\dot{\xi}_r + E(\xi, \dot{\xi}) - K_D s = H(\xi)\,\ddot{\xi} + C(\xi, \dot{\xi})\,\dot{\xi} + E(\xi, \dot{\xi})$$

$$\Rightarrow \quad H(\xi)\,[\ddot{\xi} - \ddot{\xi}_r] + C(\xi, \dot{\xi})\,[\dot{\xi} - \dot{\xi}_r] + K_D s = 0$$

$$\Rightarrow \quad H(\xi)\,\dot{s} + C(\xi, \dot{\xi})\,s + K_D s = 0$$

$$\Rightarrow \quad H(\xi)\,\dot{s} = -[C(\xi, \dot{\xi}) + K_D]\,s \tag{3.16}$$

The closed-loop dynamics, Equation 3.16, drive the tracking error, $\tilde{\xi}$, to zero.

Before proceeding with the proof, it is beneficial to recall the following corollary to

Barbalat's Lemma [58].

If a scalar function $V(\boldsymbol{x}, t)$ satisfies the following conditions, then
$\dot{V}(\boldsymbol{x}, t) \to 0$, *as* $t \to \infty$

- $V(\boldsymbol{x}, t)$ *is lower bounded*

- $\dot{V}(\boldsymbol{x}, t)$ *is negative semidefinite*

- $\dot{V}(\boldsymbol{x}, t)$ *is uniformly continuous in time*

Note: The third condition is met if $\ddot{V}(\boldsymbol{x}, t)$ *is bounded*

The proof that $\tilde{\boldsymbol{\xi}} \to 0$ is based on Lyapunov analysis [58]. Consider the

following Lyapunov function, and its derivative.

$$\text{Define: } V(\boldsymbol{s}, t) = \frac{1}{2}\boldsymbol{s}^{\mathsf{T}}\boldsymbol{H}(\boldsymbol{\xi})\boldsymbol{s} \geq 0 \tag{3.17}$$

$\Rightarrow \quad \dot{V}(\boldsymbol{s}, t) = \boldsymbol{s}^{\mathsf{T}}\boldsymbol{H}(\boldsymbol{\xi})\dot{\boldsymbol{s}} + \frac{1}{2}\boldsymbol{s}^{\mathsf{T}}\dot{\boldsymbol{H}}(\boldsymbol{\xi})\boldsymbol{s}$

Substitute: $\boldsymbol{H}(\boldsymbol{\xi})\,\dot{\boldsymbol{s}} = -[\boldsymbol{C}(\boldsymbol{\xi}, \dot{\boldsymbol{\xi}}) + \boldsymbol{K_D}]\,\boldsymbol{s}$, from Equation 3.16

$\Rightarrow \quad \dot{V}(\boldsymbol{s}, t) = -\boldsymbol{s}^{\mathsf{T}}[\boldsymbol{C}(\boldsymbol{\xi}, \dot{\boldsymbol{\xi}}) + \boldsymbol{K_D}]\,\boldsymbol{s} + \frac{1}{2}\boldsymbol{s}^{\mathsf{T}}\dot{\boldsymbol{H}}(\boldsymbol{\xi})\boldsymbol{s}$

$\Rightarrow \quad \dot{V}(\boldsymbol{s}, t) = -\boldsymbol{s}^{\mathsf{T}}\boldsymbol{K_D}\boldsymbol{s} + \frac{1}{2}\boldsymbol{s}^{\mathsf{T}}[\dot{\boldsymbol{H}}(\boldsymbol{\xi}) - 2\,\boldsymbol{C}(\boldsymbol{\xi}, \dot{\boldsymbol{\xi}})]\boldsymbol{s}$

$[\dot{\boldsymbol{H}}(\boldsymbol{\xi}) - 2\,\boldsymbol{C}(\boldsymbol{\xi}, \dot{\boldsymbol{\xi}})]$ is skew $\Rightarrow \quad \frac{1}{2}\boldsymbol{s}^{\mathsf{T}}[\dot{\boldsymbol{H}}(\boldsymbol{\xi}) - 2\,\boldsymbol{C}(\boldsymbol{\xi}, \dot{\boldsymbol{\xi}})]\boldsymbol{s} = 0$

$$\Rightarrow \quad \dot{V}(\boldsymbol{s}, t) = -\boldsymbol{s}^{\mathsf{T}}\boldsymbol{K_D}\boldsymbol{s} < 0 \;\forall\; \boldsymbol{s} \neq \boldsymbol{0}, \text{ given: } \boldsymbol{K_D} = \boldsymbol{K_D}^{\mathsf{T}} > \boldsymbol{0} \tag{3.18}$$

Since $\boldsymbol{H}(\boldsymbol{\xi})$ is positive definite, $V(\boldsymbol{s}, t)$, Equation ??. $\dot{V}(\boldsymbol{s}, t)$ is negative

semidefinite, Equation 3.18. $\boldsymbol{\xi}(t)$ and $\boldsymbol{\xi_d}(t)$ are assumed at least twice differentiable.

Therefore, $\dot{V}(\boldsymbol{s}, t)$ is uniformly continuous in time. Thus, Barbalat's Lemma

64

guarantees $\dot{V}(\boldsymbol{s}, t) \to 0$ as $t \to 0$, implying $\boldsymbol{s}(t) \to 0$ as $t \to 0$. To prove stable

tracking, consider $\tilde{\boldsymbol{\xi}}(t)$ as the output of the stable linear system, $\boldsymbol{s}(t) = \dot{\tilde{\boldsymbol{\xi}}}(t) + \boldsymbol{\Lambda}\, \tilde{\boldsymbol{\xi}}(t)$,

with $\boldsymbol{s}(t)$ as the input. It follows that $\boldsymbol{s}(t) \to 0$ implies $\tilde{\boldsymbol{\xi}}(t) \to 0$, concluding the

proof. The control specified in Equation 3.15 guarantees global asymptotic tracking

stability for a system modeled by Equation 3.14. A similar procedure and proof

applies for certain systems with the more general form of kinematics expressed in

Equation 3.13.

This approach assumes perfect knowledge of the system dynamics and perfect

measurement of the system state, $\boldsymbol{\xi}(t)$ and $\dot{\boldsymbol{\xi}}(t)$. This ideal is not encountered in

the control of real systems. Compensating for uncertainty in the system dynamics

is the topic of the next chapter.

3.2   Formation Flying at L_2, Linear Control Design

3.2.1   Linearized Dynamics

This subsection summarizes the linearized dynamics of relative motion

associated with the formation flying problem, as developed in chapter 2.

3.2.1.1   Linearized Translation Dynamics

Neglecting disturbances, Equation 2.18 represents the linearized dynamics of

relative motion in regions governed by Restricted Three Body Problem dynamics.

The equation, applicable to the region surrounding a libration point, is expressed in matrix form as:

$$\dot{\boldsymbol{\xi}} = {}^{\mathbf{I}}\mathbf{A}(t)\,\boldsymbol{\xi} + \boldsymbol{B}\,(\boldsymbol{u}_{thrust,F} - \boldsymbol{u}_{thrust,L}) \tag{3.19}$$

Where:

$$\boldsymbol{\xi} = \begin{bmatrix} \boldsymbol{x} \\ \dot{\boldsymbol{x}} \end{bmatrix} ; \quad {}^{\mathbf{I}}\mathbf{A}(t) = \begin{bmatrix} \mathbf{0} & \mathbf{I_3} \\ {}^{I}\boldsymbol{\Xi}(t) & \mathbf{0} \end{bmatrix} ; \quad \boldsymbol{B} = \begin{bmatrix} \mathbf{0} \\ \mathbf{I_3} \end{bmatrix}$$

The thrust, $\boldsymbol{u}_{thrust,L}$, command for the Leader spacecraft is included for completeness, but is considered zero. The expression for ${}^{I}\boldsymbol{\Xi}(t)$ is:

$$
\begin{aligned}
{}^{I}\boldsymbol{\Xi}(t) &= \left\{ -(c_1 + c_2)\,\mathbf{I_3} + 3\,c_1\,[\boldsymbol{e}_{EL}(t)\,\boldsymbol{e}_{EL}(t)^{\mathsf{T}}] + 3\,c_2\,[\boldsymbol{e}_{SL}(t)\,\boldsymbol{e}_{SL}(t)^{\mathsf{T}}] \right\} \\
c_1 &= \mu_{em}||\boldsymbol{r}_{EL}(t)||^{-3} \\
c_2 &= \mu_s||\boldsymbol{r}_{SL}(t)||^{-3}
\end{aligned}
$$

3.2.2 Linear Translation Control

Equation 3.19 provides the basic translational dynamics for a linear control system. However, there are two important issues to address in the design process. First, the dynamics, although linear, are time varying. Can an LQR design, based on linear time-invariant systems, be successfully implemented? Second, the dynamics are linearized about the Leader spacecraft position, so the position/set point for the Follower is offset from the system equilibrium point (Leader position). Therefore, the controller must compensate for the gravity gradient between the spacecraft positions in addition to other disturbances. The issues are addressed in reverse order. A

66

controller design, including gravity gradient compensation, is developed based on the time invariant assumption. The robustness of the design is tested against the true time varying nature of the dynamics. Note that the control design assumes accurate knowledge of the relative position and velocity of the formation spacecraft. Also, implementation of gain scheduling requires periodic update of the absolute position of the Leader spacecraft.

3.2.2.1 PID Control Design

The controller is required to counteract the gravity gradient associated with a setpoint offset between the Leader and Follower positions. Based on the mission profiles discussed in Chapter 1, the offset is expected to remain fixed in inertial coordinates during science observations. The thrust required to maintain the offset position will follow a slowly changing dynamic profile. Therefore, adding a sufficiently fast integrator to the control algorithm provides effective compensation for the required offset thrust, as well as other steady state disturbances.

Including an integrator in the control design is accomplished by augmented error dynamics evaluated at t_0:

$$
\begin{aligned}
\dot{\boldsymbol{\xi}}_{aug} &= \boldsymbol{A}_{aug} \, \boldsymbol{\xi}_{aug} + \boldsymbol{B}_{aug} \, (\boldsymbol{u}_{thrust,F}) \\
\boldsymbol{\xi} &= \boldsymbol{C}_{aug} \, \boldsymbol{\xi}_{aug}
\end{aligned}
\tag{3.20}
$$

Where:

$$\boldsymbol{\xi}_{aug} = \begin{bmatrix} v \\ \boldsymbol{\xi} \end{bmatrix} = \begin{bmatrix} v \\ \tilde{\boldsymbol{x}} \\ \dot{\tilde{\boldsymbol{x}}} \end{bmatrix} ; \quad \boldsymbol{A}_{aug} = \begin{bmatrix} \mathbf{0} & \mathbf{I_3} & \mathbf{0} \\ \mathbf{0} & \mathbf{0} & \mathbf{I_3} \\ \mathbf{0} & {}^{I}\boldsymbol{\Xi}(t_0) & \mathbf{0} \end{bmatrix} ; \quad \boldsymbol{B}_{aug} = \begin{bmatrix} \mathbf{0} \\ \mathbf{0} \\ \mathbf{I_3} \end{bmatrix}$$

3.2.2.2   Linear Controller Design

Using the time invariant augmented dynamics, the control law development follows the Linear Quadratic Regulator (LQR) design, as discussed in Section 3.1.1.2. The cost function is defined as:

$$\boldsymbol{\mathcal{J}}_{cost} = \int_0^T \left\{ [\boldsymbol{\xi}_{aug}]^\mathsf{T} \, \boldsymbol{Q} \, \boldsymbol{\xi}_{aug} \; + \; [\boldsymbol{u}_{thrust,F}]^\mathsf{T} \, \boldsymbol{R} \, \boldsymbol{u}_{thrust,F} \right\} \, dt \tag{3.21}$$

The solution which minimizes $\boldsymbol{\mathcal{J}}_{cost}$ is specified $\boldsymbol{u}_{thrust,F}$ as:

$$\boldsymbol{u}_{thrust,F} = -\boldsymbol{K} \, \boldsymbol{\xi}_{aug}, \qquad \boldsymbol{K} = \boldsymbol{R}^{-1} \, \boldsymbol{B}_{aug}^{\mathsf{T}} \, \boldsymbol{M} \tag{3.22}$$

Where $\boldsymbol{M}$ solves the following algebraic matrix Riccati equation:

$$\boldsymbol{M} \, \boldsymbol{A}_{aug} + \boldsymbol{A}_{aug}^{\mathsf{T}} \, \boldsymbol{M} - \boldsymbol{M} \, \boldsymbol{B}_{aug} \, \boldsymbol{R}^{-1} \, \boldsymbol{B}_{aug}^{\mathsf{T}} \, \boldsymbol{M} = -\boldsymbol{Q} \tag{3.23}$$

Following classical linear feedback control conventions, the negative of the tracking error is defined as the input for the controller dynamics. The Follower control is defined as the output. The controller dynamics and output equation are expressed as:

$$\begin{aligned} \dot{v} &= \boldsymbol{A}_{cntrl} \, v \; + \boldsymbol{B}_{cntrl} \, (-\boldsymbol{\xi}) \\ \boldsymbol{u}_{thrust,F} &= \boldsymbol{C}_{cntrl} \, v \; + \boldsymbol{D}_{cntrl} \, (-\boldsymbol{\xi}) \end{aligned} \tag{3.24}$$

Where:

$$\boldsymbol{A}_{cntrl} = [\, \mathbf{0}\,]; \qquad\qquad \boldsymbol{B}_{cntrl} = [\, \mathbf{I_3}\ \ \mathbf{0}\,]$$

$$\boldsymbol{C}_{cntrl} = -\boldsymbol{K} \begin{bmatrix} \mathbf{I_3} \\ \\ \mathbf{0}_{6\times3} \end{bmatrix} \qquad \boldsymbol{D}_{cntrl} = \boldsymbol{K} \begin{bmatrix} \mathbf{0}_{3\times6} \\ \\ \mathbf{I_6} \end{bmatrix}$$

The compensator transfer function is expressed as:

$$\boldsymbol{G}_c(\boldsymbol{s}) \ = \boldsymbol{C}_{cntrl}\, (\boldsymbol{s}\mathbf{I})^{-1}\, \boldsymbol{B}_{cntrl} + \boldsymbol{D}_{cntrl} = \boldsymbol{K} \begin{bmatrix} -(\boldsymbol{s}\,\mathbf{I_3})^{-1} & \mathbf{0}_{3\times3} \\ \\ \mathbf{I_3} & \mathbf{0}_{3\times3} \\ \\ \mathbf{0}_{3\times3} & \mathbf{I_3} \end{bmatrix} \qquad (3.25)$$

Define the plant model transfer function, $\boldsymbol{G}_m(\boldsymbol{s})$, based on Equation 3.19 with $\boldsymbol{A}(t)$ evaluated at t_0. An explicit expression for $\boldsymbol{G}_m(\boldsymbol{s})$ is derived in the next section, reference equation 3.29. Based on the block diagram in Figure 3.1, the closed-loop transfer function with the input/output defined as position vectors is expressed as:

$$\boldsymbol{G}_{CL}(\boldsymbol{s}) \ = [\mathbf{I_3}\ \ \mathbf{0}]\, \{\boldsymbol{G}_m(\boldsymbol{s})\boldsymbol{G}_c(\boldsymbol{s})(\mathbf{I} + \boldsymbol{G}_m(\boldsymbol{s})\boldsymbol{G}_c(\boldsymbol{s}))^{-1}\}\, [\mathbf{I_3}\ \ \boldsymbol{s}\mathbf{I_3}]^{\mathsf{T}} \qquad (3.26)$$
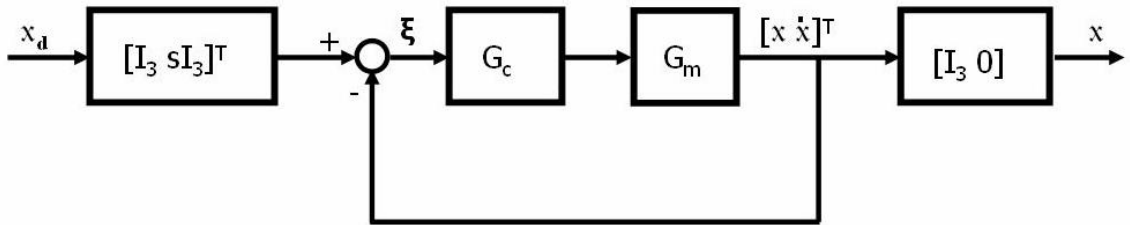
Figure 3.1: Closed-Loop Control Block Diagram

69

Using the specific design parameters discussed in Chapter 5, the control law yields the closed-loop gain profile similar to that in Figure 3.2. Note: the profile is identical for all channels.
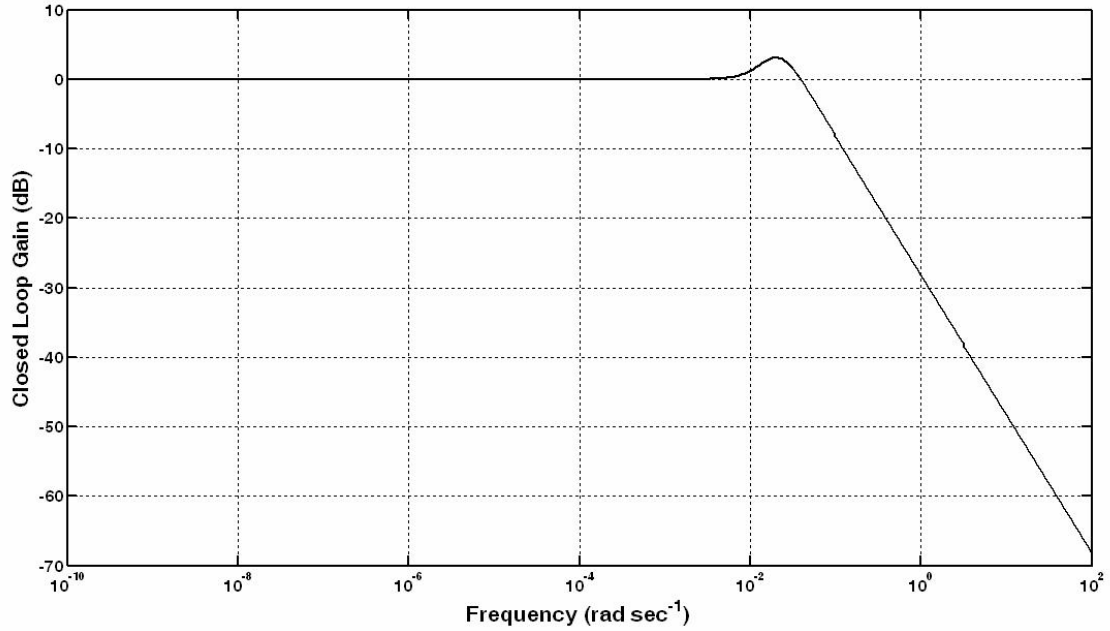
Figure 3.2: Closed-Loop Gain, all-channels, for $\boldsymbol{G}_{CL}(\boldsymbol{s})$

3.2.2.3   Robustness of Time Invariant Assumption

The time invariant assumption introduces a modeling error, expressed as a multiplicative uncertainty in terms of the nominal plant model defined at t_0, $\boldsymbol{G}_m(\boldsymbol{s})$; the plant uncertainty, $\boldsymbol{\Delta}(\boldsymbol{s}, \boldsymbol{t})$; and the time dependent plant model, $\boldsymbol{G}(\boldsymbol{s}, \boldsymbol{t})$.

$$\boldsymbol{G}(s, t) = (\mathbf{I} + \boldsymbol{\Delta}(s, t))\, \boldsymbol{G}_m(s) \tag{3.27}$$

70

Based on Equation 3.19, $G(s, t)$ is evaluated as:

$$
\begin{aligned}
G(s, t) \ &= C \left(s\mathbf{I} - A(t) \right)^{-1} B \\
&= \begin{bmatrix} \mathbf{I_3} & \mathbf{0} \end{bmatrix} \left(\begin{bmatrix} s\mathbf{I} & -\mathbf{I_3} \\ -{}^{I}\Xi(t) & s\mathbf{I} \end{bmatrix} \right)^{-1} \begin{bmatrix} \mathbf{0} \\ \mathbf{I_3} \end{bmatrix} \\
&= \begin{bmatrix} \mathbf{I_3} & \mathbf{0} \end{bmatrix} \begin{bmatrix} s(s^2\,\mathbf{I} - {}^{I}\Xi(t))^{-1} & (s^2\,\mathbf{I} - {}^{I}\Xi(t))^{-1} \\ {}^{I}\Xi(t)(s^2\,\mathbf{I} - {}^{I}\Xi(t))^{-1} & s(s^2\,\mathbf{I} - {}^{I}\Xi(t))^{-1} \end{bmatrix} \begin{bmatrix} \mathbf{0} \\ \mathbf{I_3} \end{bmatrix} \\
&= (s^2\,\mathbf{I} - {}^{I}\Xi(t))^{-1}
\end{aligned}
$$

$$(3.28)$$

Likewise, the nominal plant employed in the compensator design is expressed as:

$$
G_m(s) \ = (s^2\,\mathbf{I} - {}^{I}\Xi(t_0))^{-1} \tag{3.29}
$$

The modeling uncertainty is computed as:

$$
\begin{aligned}
\Delta(s, t) \ &= G(s, t) G_m(s)^{-1} - \mathbf{I} \\
&= (s^2\,\mathbf{I} - {}^{I}\Xi(t))^{-1} (s^2\,\mathbf{I} - {}^{I}\Xi(t_0)) - \mathbf{I}
\end{aligned}
$$

$$(3.30)$$

Paraphrasing Theorem 2.4.4 of reference [24]: Given a plant modeled as Equation 3.27 with a stabilizing controller $G_c(s)$, the closed-loop system is well-posed and internally stable for all $\Delta(s, t)$ with $\frac{1}{\overline{\sigma}(\Delta)} > \overline{\sigma}(G_{CL})$, provided $\Delta(s, t)$ is a rational transfer function such that $G(s, t)$ and $G_m(s)$ have the same number of poles in the closed-right-half plane. G_{CL} is the closed-loop gain of the nominal plant from Equation 3.26.
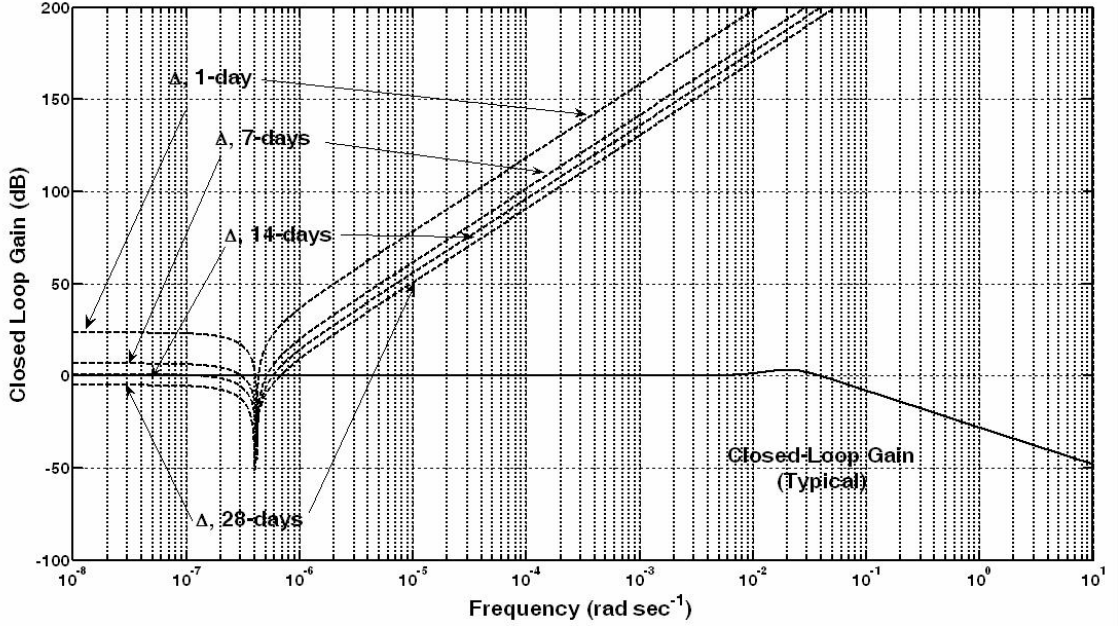
Figure 3.3: Maximum Singular Value Comparison: Inverse Model Uncertainty $\frac{1}{\overline{\sigma}(\Delta)}$ and Closed-Loop Gain

Based on the mission profile and control design presented in Chapter 5, Figure 3.3 superimposes the various gain profiles for $\frac{1}{\overline{\sigma}(\Delta)}$ with the closed-loop gain from Figure 3.2. $\overline{\sigma}(\Delta)$ is evaluated after holding the plant model, $\boldsymbol{G_m(s)}$, fixed for 1 day, 7 days, 14 days, and 28 days, as shown. The plot demonstrates the condition, $\frac{1}{\overline{\sigma}(\Delta)} > \overline{\sigma}(\boldsymbol{G_{CL}})$, is met for all three cases for frequencies above 10^{-6} rad/sec. For the 14 day case the gain at the lowest frequencies is approximately 0.77. The condition is violated in all cases for a frequency of $\approx 4 \times 10^{-7}$ rad/sec. This frequency represents the natural harmonic motion of the formation. For frequencies less than 10^{-7} rad/sec, the condition, $\frac{1}{\overline{\sigma}(\Delta)} > \overline{\sigma}(\boldsymbol{G_{CL}})$, is met for 14 days without a plant model update, representing an upper bound on the required update interval.

In a strict sense the time invariant assumption does not guarantee a stable

72

closed-loop system. The problem is associated with the natural harmonic motion between the Leader and Follower spacecraft. Examination of Equation 3.30 reveals that $G(s,t)$ is unbounded when s^2 matches the eigenvalues of $^I\Xi(t)$. The natural motion has a period of approximately 6 months for missions stationed near the Earth/Moon-Sun L_2 point. Although the analysis is insufficient to guarantee robustness against uncertainty, the results suggest the performance of the controller would benefit with gain scheduled updates within a 15 day period. The time interval between required updates is mission dependent. Mission specific analysis is required to determine appropriate update intervals. Further analysis in Section 3.2.2.5 demonstrates the controller is robustly stable.

3.2.2.4   Robustness of Double Integrator Dynamic Model Assumption

As discussed in Section 1.4, references [45, 59, 65] employ double integrator dynamics, i.e. zero gravity, for translation control design. Using the multiplicative model, the plant uncertainty is depicted in Figure 3.4, evaluated at the end of 1 day of propagation. The plant uncertainty profile is nearly identical when computed after 0.1 days through 28 days of propagation. The condition, $\frac{1}{\overline{\sigma}(\Delta)} > \overline{\sigma}(G_{CL})$, is met only for frequencies above $\approx 6 \times 10^{-7}$ rad sec^{-1}. Therefore, as above, analysis does not guarantee robust stability. However, the results show inclusion of the gravity model in the control design improves system robustness.
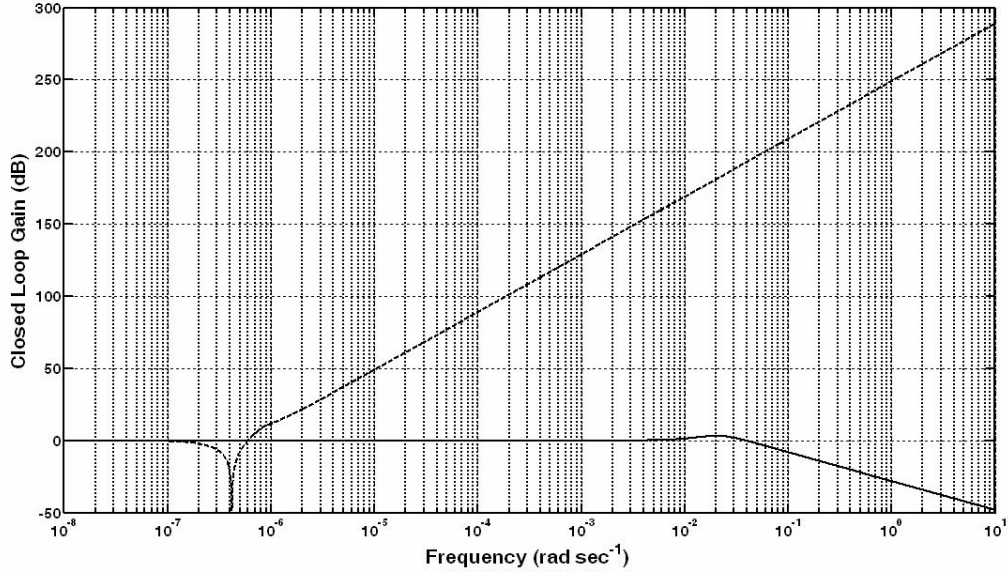
Figure 3.4: Maximum Singular Value Comparison: Inverse Model Uncertainty, $\frac{1}{\bar{\sigma}(\Delta)}$, for a Double Integrator Dynamics Model and Closed-Loop Gain, $\boldsymbol{G}_{CL}(\boldsymbol{s})$

3.2.2.5   Lyapunov Based Robustness Analysis

Analysis in Sections 3.2.2.3 and 3.2.2.4 shows the robustness criteria is met for frequencies above the natural harmonic motion of the spacecraft formation. However, the test fails for frequencies near (and below for some cases) the natural system harmonic. Lyapunov theory provides an alternate test for robustness.

The closed-loop dynamics for the formation control problem are expressed in terms of the augmented dynamics and controller design presented in Sections 3.2.2.1 and 3.2.2.2. The closed-loop dynamics are:

$$\dot{\boldsymbol{\xi}}_{aug}(t) \; = \boldsymbol{A}_{aug}(t)\,\boldsymbol{\xi}_{aug}(t) - \boldsymbol{B}_{aug}\,\boldsymbol{K}\,\boldsymbol{\xi}_{aug}(t) \tag{3.31}$$

Define $\tilde{\boldsymbol{A}}_{aug}(t) \equiv \boldsymbol{A}_{aug}(t) - \boldsymbol{A}_{aug}(t_0)$, then rewrite Equation 3.31 as:

74

$$\dot{\boldsymbol{\xi}}_{aug}(t) = \boldsymbol{A}_{aug}(t_0)\,\boldsymbol{\xi}_{aug}(t) - \boldsymbol{B}_{aug}\,\boldsymbol{K}\,\boldsymbol{\xi}_{aug}(t) + \tilde{\boldsymbol{A}}_{aug}(t)\,\boldsymbol{\xi}_{aug}(t)$$

$$= \boldsymbol{A}_{CL}(t_0)\,\boldsymbol{\xi}_{aug}(t) + \tilde{\boldsymbol{A}}_{aug}(t)\,\boldsymbol{\xi}_{aug}(t) \tag{3.32}$$

$$= \left[\boldsymbol{A}_{CL}(t_0) + \tilde{\boldsymbol{A}}_{aug}(t)\right]\,\boldsymbol{\xi}_{aug}(t)$$

Where: $\boldsymbol{A}_{CL}(t_0) \equiv \boldsymbol{A}_{aug}(t_0) - \boldsymbol{B}_{aug}\,\boldsymbol{K}$

Robust stability is established with Lyapunov analysis. Define the Lyapunov function $V(\boldsymbol{\xi}_{aug}, t) = \boldsymbol{\xi}_{aug}{}^{\mathsf{T}}\,\boldsymbol{P}\,\boldsymbol{\xi}_{aug}$ with $\boldsymbol{P} = \boldsymbol{P}^{\mathsf{T}} > \boldsymbol{0}$, such that $\boldsymbol{P} = \boldsymbol{P}^{\mathsf{T}} > \boldsymbol{0}$ satisfies:

$$\boldsymbol{A}_{CL}(t_0)^{\mathsf{T}}P + P\boldsymbol{A}_{CL}(t_0) = -\mathbf{I_9} \tag{3.33}$$

Equation 3.32 is asymptotically stable if the derivative of the Lyapunov function is strictly negative. In fact, based on the quadratic nature of the defined $V(\boldsymbol{\xi}_{aug}, t)$, exponential stability is established by Theorem 4.10 from [33], if $\dot{V}(\boldsymbol{\xi}_{aug}, t) < -k||\boldsymbol{\xi}_{aug}||^2$, where k is a positive constant.

Compute the Lyapunov function derivative.

$$\dot{V}(\boldsymbol{\xi}_{aug}, t) = \dot{\boldsymbol{\xi}}_{aug}{}^{\mathsf{T}}\,\boldsymbol{P}\,\boldsymbol{\xi}_{aug} + \boldsymbol{\xi}_{aug}{}^{\mathsf{T}}\,\boldsymbol{P}\,\dot{\boldsymbol{\xi}}_{aug} \tag{3.34}$$

Combine Equations 3.32 and 3.34.

$$\dot{V}(\boldsymbol{\xi}_{aug}, t) = \boldsymbol{\xi}_{aug}{}^{\mathsf{T}}\left[\boldsymbol{A}_{CL}(t_0) + \tilde{\boldsymbol{A}}_{aug}(t)\right]^{\mathsf{T}}\boldsymbol{P}\,\boldsymbol{\xi}_{aug}$$

$$+\boldsymbol{\xi}_{aug}{}^{\mathsf{T}}\,\boldsymbol{P}\left[\boldsymbol{A}_{CL}(t_0) + \tilde{\boldsymbol{A}}_{aug}(t)\right]\boldsymbol{\xi}_{aug}$$

$$= \boldsymbol{\xi}_{aug}{}^{\mathsf{T}}\left[\boldsymbol{A}_{CL}(t_0)^{\mathsf{T}}\boldsymbol{P} + \boldsymbol{P}\boldsymbol{A}_{CL}(t_0)\right]\boldsymbol{\xi}_{aug} \tag{3.35}$$

$$+\boldsymbol{\xi}_{aug}{}^{\mathsf{T}}\left[\tilde{\boldsymbol{A}}_{aug}(t)^{\mathsf{T}}\boldsymbol{P} + \boldsymbol{P}\tilde{\boldsymbol{A}}_{aug}(t)\right]\boldsymbol{\xi}_{aug}$$

Combine Equations 3.33 and 3.35.

$$\dot{V}(\boldsymbol{\xi}_{aug}, t) \;\; = -\boldsymbol{\xi}_{aug}{}^\mathsf{T}\, \boldsymbol{\xi}_{aug} \;+ \boldsymbol{\xi}_{aug}{}^\mathsf{T} \left[\tilde{\boldsymbol{A}}_{aug}(t)^\mathsf{T} \boldsymbol{P} + \boldsymbol{P} \tilde{\boldsymbol{A}}_{aug}(t) \right] \boldsymbol{\xi}_{aug}$$
$$= -||\boldsymbol{\xi}_{aug}||^2 \;+\; 2\, \boldsymbol{\xi}_{aug}{}^\mathsf{T}\, \boldsymbol{P}\, \tilde{\boldsymbol{A}}_{aug}(t)\, \boldsymbol{\xi}_{aug} \tag{3.36}$$

From the Cauchy-Schwartz Inequality:

$$\boldsymbol{\xi}_{aug}{}^\mathsf{T}\, \boldsymbol{P}\, \tilde{\boldsymbol{A}}_{aug}(t)\, \boldsymbol{\xi}_{aug} \;\; \le \;\; ||\boldsymbol{\xi}_{aug}||^2\, ||\boldsymbol{P}||\, ||\tilde{\boldsymbol{A}}_{aug}(t)|| \tag{3.37}$$

Combine Equations 3.36 and 3.37.

$$\dot{V}(\boldsymbol{\xi}_{aug}, t) \;\; \le -||\boldsymbol{\xi}_{aug}||^2 \;+\; 2\, ||\boldsymbol{\xi}_{aug}||^2\, ||\boldsymbol{P}||\, ||\tilde{\boldsymbol{A}}_{aug}(t)||$$
$$= -||\boldsymbol{\xi}_{aug}||^2 \;+\; 2\, ||\boldsymbol{\xi}_{aug}||^2\, \bar{\sigma}\{\boldsymbol{P}\}\, \bar{\sigma}\{\tilde{\boldsymbol{A}}_{aug}(t)\} \tag{3.38}$$
$$= \left(-1 + 2\, \bar{\sigma}\{\boldsymbol{P}\}\, \bar{\sigma}\{\tilde{\boldsymbol{A}}_{aug}(t)\} \right)\, ||\boldsymbol{\xi}_{aug}||^2$$

Where $\bar{\sigma}\{\boldsymbol{P}\}$ represents the maximum singular value of $\boldsymbol{P}$. Therefore, $2\,\bar{\sigma}\{\boldsymbol{P}\}\,\bar{\sigma}\{\tilde{\boldsymbol{A}}_{aug}(t)\} \;<\; 1 \;\;\Rightarrow\;\; \dot{V}(\boldsymbol{\xi}_{aug}, t_0) \;<\; 0$. Based on the benchmark mission scenario, defined in Chapter 4, $\left[2\, \bar{\sigma}\{\boldsymbol{P}\}\, \bar{\sigma}\{\tilde{\boldsymbol{A}}_{aug}(t)\} \right] \;\in\; [0 \quad 1.5 \times 10^{-4}]$ for $t \;\in\; [0 \quad 60 \text{ days}]$. Therefore, the controller design is robustly stable against variations in $\boldsymbol{A}_{aug}(t)$.

The controller design based on double integrator dynamics exhibits similar robustness characteristics with the variations in $\left[2\, \bar{\sigma}\{\boldsymbol{P}\}\, \bar{\sigma}\{\tilde{\boldsymbol{A}}_{aug}(t)\} \right]$ in the range $[9 \times 10^{-5} \quad 1.5 \times 10^{-4}]$ throughout the same 60-day period.

Based on this analysis, the Lyapunov function derivative is upper bounded by $-k||\boldsymbol{\xi}_{aug}||^2$ with $0 < k \le .999$. Therefore, Equation 3.31 is exponentially stable. Note, this analysis supports the validity of formulating a controller design based on double integrator dynamics. However, it is important to consider compensation

for the real gravity gradient between spacecraft, which is accomplished with the integrator component of the PID controller.

3.2.3   Linear Attitude Control

3.2.3.1   Linearized Attitude Dynamics

From Chapter 2, linearized attitude dynamics are developed with assumed small body rates and small attitude errors. Assuming the output is equivalent to the attitude state, from Equation 2.40 the dynamics are expressed in the form of Equations 3.7 and 3.8 with:

$$
\boldsymbol{A} \;=\; \begin{bmatrix} \boldsymbol{0} & \frac{1}{2}\mathbf{I_3} \\ \boldsymbol{0} & \boldsymbol{0} \end{bmatrix} \;;\quad \boldsymbol{B} = \begin{bmatrix} \boldsymbol{0} \\ \boldsymbol{H_R}^{-1} \end{bmatrix} \;;\quad \boldsymbol{C} = \mathbf{I_6}; \quad \boldsymbol{D} = \boldsymbol{0} \tag{3.39}
$$

3.2.3.2   Linear Attitude Control

The attitude control law is designed using the LQR method described in Section 3.1.1.2 with the values of $\boldsymbol{A}$ and $\boldsymbol{B}$ shown above. The control law is expressed as:

$$
\boldsymbol{\tau} \;=\; -\boldsymbol{K} \begin{bmatrix} \tilde{\boldsymbol{q}} \\ \tilde{\boldsymbol{\omega}} \end{bmatrix} \;\text{with:}\; \boldsymbol{K} = \boldsymbol{R}^{-1} \boldsymbol{B}^{\mathsf{T}} \boldsymbol{M} \tag{3.40}
$$

Note: The attitude control design does not include an integrator based on the assumed absence of disturbing torques. An integrator would serve to compensate for a constant disturbance torque.

3.3   Formation Flying at L_2, Nonlinear Control Design

Considering the available nonlinear control design techniques, the Lyapunov based approach discussed in Section 3.1.2 is selected.

3.3.1   Summary of Spacecraft Dynamics

This subsection summarizes the linearized dynamics of relative motion associated with the formation flying problem, as developed in chapter 2.

3.3.1.1   Translation

From Equation 2.7 the relative motion (translation) of two spacecraft operating in the vicinity of a libration point is expressed as:

$$\ddot{\boldsymbol{x}} = -\left\{\frac{\mu_{em}}{\|\boldsymbol{r}_{EF}\|^3} + \frac{\mu_s}{\|\boldsymbol{r}_{SF}\|^3}\right\}\boldsymbol{x} - \mu_{em}\left\{\frac{1}{\|\boldsymbol{r}_{EF}\|^3} - \frac{1}{\|\boldsymbol{r}_{EL}\|^3}\right\}\boldsymbol{r}_{EL}$$

(3.41)

$$-\mu_s\left\{\frac{1}{\|\boldsymbol{r}_{SF}\|^3} - \frac{1}{\|\boldsymbol{r}_{SL}\|^3}\right\}\boldsymbol{r}_{SL} + \Delta\boldsymbol{f}_{solar} + \Delta\boldsymbol{f}_{pert} + \boldsymbol{u}_{thrust,F}$$

3.3.1.2 Attitude Dynamics

The rotational dynamics of a rigid body spacecraft without reaction wheels is given by:

$$\boldsymbol{H_R}\,\dot{\boldsymbol{\omega}} - [\boldsymbol{H_R}\,\boldsymbol{\omega}\times]\,\boldsymbol{\omega} = \boldsymbol{\tau} \tag{3.42}$$

Where:

$\quad\quad\boldsymbol{\omega}$ – True Spacecraft Angular Rate

$\quad\quad\boldsymbol{H_R}$ – Spacecraft Moment of Inertia, constant

3.3.1.3 Kinematics

The kinematic equation of motion for a rotating body is given by:

$$\dot{\boldsymbol{q}} = \frac{1}{2}\begin{bmatrix} \eta\,\mathbf{I_3} + [\boldsymbol{\varepsilon}\times] \\ -\boldsymbol{\varepsilon}^\mathsf{T} \end{bmatrix}\boldsymbol{\omega} \tag{3.43}$$

Where:

$\quad\quad\boldsymbol{q}= [\boldsymbol{\varepsilon}\,\eta]^\mathsf{T}$ – True Spacecraft Attitude Quaternion

$\quad\quad\boldsymbol{\varepsilon}$ – Vector Component of Attitude Quaternion

$\quad\quad\eta$ – Scalar Component of Attitude Quaternion

3.3.2 Control Design

The control strategy is developed based on Lyapunov theory. Implementation requires knowledge of the true (inertial reference) state of the Follower spacecraft, including the absolute position of each spacecraft, the relative velocity, and the

spacecraft attitude and rate. As a minimum, the absolute position of the Leader spacecraft is required. Additional state information may be required in the definition of the desired state of the Follower. The control design assumes the Leader spacecraft is following a ballistic trajectory, meaning there is no applied thrust. Also, the design neglects unmodeled disturbances, and assumes perfect knowledge of the spacecraft mass properties.

3.3.2.1 Translation

Comparing the form of Equation 3.12, and the dynamics expressed in Equation 3.41, provides:

$$\boldsymbol{\xi} = \boldsymbol{x}$$

$$\boldsymbol{\nu} = \dot{\boldsymbol{x}}$$

$$\boldsymbol{H(\xi)} = \mathbf{I}_3$$

$$\boldsymbol{C(\xi, \nu)} = \mathbf{0}$$

$$\boldsymbol{E(\xi, \nu)} = -\left\{ \frac{\mu_{em}}{||\boldsymbol{r_{EF}}||^3} + \frac{\mu_s}{||\boldsymbol{r_{SF}}||^3} \right\} \boldsymbol{\xi} - \mu_{em} \left\{ \frac{1}{||\boldsymbol{r_{EF}}||^3} - \frac{1}{||\boldsymbol{r_{EL}}||^3} \right\} \boldsymbol{r_{EL}}$$
$$- \mu_s \left\{ \frac{1}{||\boldsymbol{r_{SF}}||^3} - \frac{1}{||\boldsymbol{r_{SL}}||^3} \right\} \boldsymbol{r_{SL}}$$

The control design follows from Equation 3.15, and is specified as:

$$\boldsymbol{u} = \mathbf{I}_3 \, \ddot{\boldsymbol{x}}_r - \left\{ \frac{\mu_{em}}{||\boldsymbol{r_{EF}}||^3} + \frac{\mu_s}{||\boldsymbol{r_{SF}}||^3} \right\} \boldsymbol{x} - \mu_{em} \left\{ \frac{1}{||\boldsymbol{r_{EF}}||^3} - \frac{1}{||\boldsymbol{r_{EL}}||^3} \right\} \boldsymbol{r_{EL}}$$
$$- \mu_s \left\{ \frac{1}{||\boldsymbol{r_{SF}}||^3} - \frac{1}{||\boldsymbol{r_{SL}}||^3} \right\} \boldsymbol{r_{SL}} - \boldsymbol{K_D} \boldsymbol{s}$$

(3.44)

$$\boldsymbol{K_D} \; - \; \text{Design parameter, specified so } \boldsymbol{K_D} = \boldsymbol{K_D}^\mathsf{T} > \boldsymbol{0}$$

$$\tilde{\boldsymbol{x}} \; = \; (\boldsymbol{x} \; - \; \boldsymbol{x_d}), \text{ position tracking error}$$

$$\dot{\boldsymbol{x}}_{\boldsymbol{r}}(t) \; = \; \dot{\boldsymbol{x}}_{\boldsymbol{d}}(t) - \boldsymbol{\Lambda} \, \tilde{\boldsymbol{x}}, \text{ reference velocity}$$

$$\boldsymbol{\Lambda} \; - \; \text{Design parameter, specified so} \boldsymbol{\Lambda} = \boldsymbol{\Lambda}^\mathsf{T} > \boldsymbol{0}$$

$$\boldsymbol{s}(t) \; = \; \dot{\tilde{\boldsymbol{x}}} \; + \; \boldsymbol{\Lambda} \, \tilde{\boldsymbol{x}} \; = \; \dot{\boldsymbol{x}} \; - \; \dot{\boldsymbol{x}}_{\boldsymbol{r}}, \text{ error metric}$$

3.3.2.2 Attitude

A globally stable control scheme based on Lyapunov control theory is provided by [14]. The nonadaptive case is discussed in Section 3.1.2 of this document. The adaptive case is discussed in Section 5.3.2 of this document. For the nonadaptive case the control law is defined as:

$$\boldsymbol{\tau} = \boldsymbol{H_R}\dot{\boldsymbol{\omega}}_{\boldsymbol{r}} - [\boldsymbol{H_R}\,\boldsymbol{\omega}\times]\boldsymbol{\omega}_{\boldsymbol{r}} - \boldsymbol{K_R}\boldsymbol{s_R} \tag{3.45}$$

Where:

$\boldsymbol{q_d} = [\boldsymbol{\varepsilon_d}\,\eta_d]^\mathsf{T}$ – Desired Spacecraft Attitude Quaternion

$\tilde{\boldsymbol{q}}$ $\qquad\qquad - [\tilde{\boldsymbol{\varepsilon}}\,\tilde{\eta}]^\mathsf{T} = \boldsymbol{q} \otimes \boldsymbol{q_d}^{-1}$, error quaternion

$\boldsymbol{\omega_d}$ $\qquad\qquad$ – Desired Spacecraft Angular Rate

$\boldsymbol{\omega_r}$ $\qquad\qquad - (\boldsymbol{\omega_d} - \boldsymbol{\Lambda_R}\,\tilde{\boldsymbol{\varepsilon}})$, reference angular rate

$\boldsymbol{s_R}$ $\qquad\qquad - (\boldsymbol{\omega} - \boldsymbol{\omega_r})$, angular rate error metric

$\boldsymbol{\Lambda_R}$ $\qquad\qquad$ – Design parameter, constant, symmetric, positive definite matrix

$\boldsymbol{K_R}$ $\qquad\qquad$ – Design parameter, symmetric, uniformly positive definite matrix

3.4 Combined Translation/Attitude Control Law

As discussed in Section 2.3, with proper thruster placement the control sensitivity matrix, $\boldsymbol{B}_{thrust}$, will have a pseudo inverse.

The desired thruster commands are computed using Equations 2.41 and 2.43, repeated here for reference:

$$\boldsymbol{F}_{thrust} = \boldsymbol{B}_{thrust}{}^{\mathsf{T}} (\boldsymbol{B}_{thrust} \, \boldsymbol{B}_{thrust}{}^{\mathsf{T}})^{-1} \, {}^{\mathbf{b}}\mathbf{U}$$

Where:

$$
{}^{\mathbf{b}}\boldsymbol{U} = \begin{bmatrix} \mathbf{R(q)} \, ({}^{\mathbf{I}}\mathbf{u}_{\mathbf{thrust,F}}) \\[2em] \boldsymbol{\tau} \end{bmatrix}
$$

Assuming $\boldsymbol{B}_{thrust}$ represents the exact performance of the thrusters, this algorithm generates thruster commands for the desired net thrust and torque for translation and rotation control. However, the computation does not ensure the thruster commands are non-negative, necessary for implementation. This problem is overcome by biasing the thruster output with a command that generates zero net thrust and torque. The bias command is designed such that $\boldsymbol{B}_{thrust}\boldsymbol{F}_{bias} = \boldsymbol{0}$, which implies $\boldsymbol{F}_{bias}$ lies in the null space of $\boldsymbol{B}_{thrust}$. Successful implementation of this strategy requires a thruster configuration which meets two criteria.

First, as previously noted, thruster placement must result in a control sensitivity matrix, $\boldsymbol{B}_{thrust}$, with a pseudo inverse. For this coupled six degree of freedom control application, $\boldsymbol{B}_{thrust}$ is required to have rank six.

Second, there must exist scalable thruster output levels such that the net force and torque on the spacecraft is zero. As a simple example consider a configuration

with pairs of thrusters placed about a spacecraft. Simultaneous firing of each thruster within a pair will generate zero net torque and force on the spacecraft. In a more general design thrusters may be paired with different locations or configured in larger subgroups. The important design consideration allows simultaneous firing of the entire group and/or subgroups of thrusters with zero net force and torque on the spacecraft. As noted above, these commands lie in the null space of $\boldsymbol{B}_{thrust}$. The set of all firing configurations, $\boldsymbol{F}_{bias}$, that satisfy $\boldsymbol{B}_{thrust}\boldsymbol{F}_{bias} = \boldsymbol{0}$, can be reduced to a set of basis vectors that spans the null space of $\boldsymbol{B}_{thrust}$. The null space is also determined as the space spanned by the eigenvectors associated with a zero eigenvalue for the matrix, $\boldsymbol{B}_{thrust}{}^{\mathsf{T}}\boldsymbol{B}_{thrust}$.

Formally stated, the requirements are:

1) $(\boldsymbol{B}_{thrust}\,\boldsymbol{B}_{thrust}{}^{\mathsf{T}})$ is invertible.

2) There exists a basis, $(\boldsymbol{v_1}, \boldsymbol{v_2}, \ldots, \boldsymbol{v_m})$ for the null space of $\boldsymbol{B}_{thrust}$

   such that the elements of each basis vector, $\boldsymbol{v_i}$, are non-negative. i.e. $v_{ij} \geq 0$

Note: The basis vectors, $\boldsymbol{v_i}$, represent a logical thruster grouping for biasing thrust commands.

As a final comment, selection of $\boldsymbol{F}_{bias}$ requires consideration of fuel efficiency. The bias with minimum $||\boldsymbol{F}_{bias}||$ which generates a vector $(\boldsymbol{F}_{thrust} + \boldsymbol{F}_{bias})$ with all non-negative terms is generally best.

Chapter 4

Simulation Results and Analysis for Linear and Nonadaptive Control

This chapter presents simulation results characterizing the performance of the linear and nonlinear control algorithms presented in Chapter 3. Section 4.1 details the simulation architecture. Section 4.2 discusses the scenario specific control design. Section 4.3 presents simulation results for the distant formation with a nominal 100 kilometer range. Section 4.4 presents results for the close formation with a nominal 50 meter range. Section 4.5 discusses the effects of perturbations on the performance of the linear and nonlinear methods.

4.1 Simulation Architecture

The simulation is designed to model a realistic dynamic environment for testing and comparing the performance of various formation flying control strategies. The simulation is constructed in MATLAB. Details of the simulation architecture follow.

4.1.1 Dynamic Environment

The dynamic environment model is limited to gravity and solar pressure. The gravity field is generated using point mass models for the Sun, Earth, Moon and the other planets. Higher order gravity models are not required due to the sufficiently large range between the formation and each gravity source. Position vectors are

defined in the standard inertial, Earth centered J2000 coordinate system. The positions of the Sun, Moon and other planets are computed from DE200 planetary ephemeris data. The DE200 ephemeris file is maintained and published by NASA's Jet Propulsion Laboratory (JPL). Ephemeris data is stored as sets of Chebychev polynomial coefficients associated with defined time intervals. Time intervals are specified in Ephemeris Time. The process steps for computing position data are: 1) Convert spacecraft time to Ephemeris Time, 2) Find the corresponding set of Chebychev coefficients for the Sun, Moon, and each planet, and 3) Evaluate polynomials based on the computed Ephemeris Time. DE200 position data is specified in J2000 coordinates with the origin at the solar system barycenter. Therefore, it is necessary to transform the position data to an Earth centered coordinate frame. The DE200 file also contains the astronomical data used to generate the ephemeris data, including the gravitational parameters for each body. The gravity field contributions for all planets are included in the simulation for completeness, recognizing some have negligible influence. [30]

Solar pressure effects are included, except for simulated results presented in Section 4.3 and 4.4, and as noted. The solar pressure model is based on a mean solar energy flux of 1358 watts/meter^2 at one astronomical unit (AU). The astronomical unit definition is based on the nominal distance between the Earth and Sun. The radiation flux at the spacecraft position is determined using an inverse-square rule based on the spacecraft to Sun range. The force exerted on each spacecraft is aligned along the Sun-spacecraft range vector, and is proportional to the cross-sectional

86

area/mass ratio, specified for each spacecraft. The cross-sectional area is assumed attitude independent. Solar pressure is assumed torque-free, i.e., the center of solar pressure is aligned through the spacecraft center of mass.

4.1.2 Propagation

Each spacecraft position is propagated using a fourth-order Runga-Kutta numerical integrator with a step size of 1 second. Propagation is based on the full nonlinear equations of motion, including gravity, solar pressure and commanded thrust. The gravitational acceleration is determined as the summation of the contributions of each celestial body, computed using the inverse-square law for point masses. Earth-centered J2000 coordinates represent an accelerated frame. Therefore, the total acceleration is biased with the acceleration of the Earth relative to the Sun, Moon and other planets.

4.1.2.1 Validation

The simulation model was validated against commercial software designed to model spacecraft dynamics. The specific tools were Satellite Tool Kit [52] and Freeflyer [18]. Simulations with common scenarios produced highly correlated results between this design and the commercial products. The comparison did not include closed-loop control, due to limitations in the commercial products. The algorithm for interpreting the JPL DE200 file is a simplified version of code developed by this author for flight qualified, ground system software.

4.1.3 Spacecraft Model

The spacecraft model is depicted in Figure 4.1. The propulsion system is configured with three sets of four thrusters. Each set of four provides thrust along a single body axis, and torque along a perpendicular body axis, such that thrust and torque authority are available along each of the three body axes.
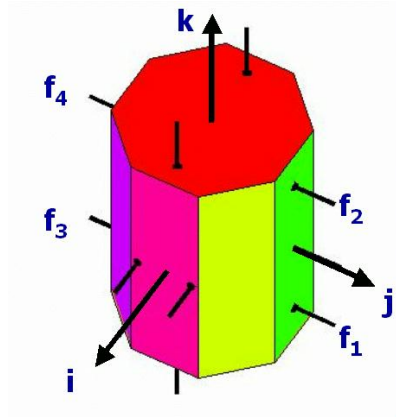
Figure 4.1: Simulation Model of Follower Spacecraft Depicting Thruster Layout

4.1.3.1 Leader Spacecraft

The Leader spacecraft is modeled with a pure ballistic trajectory, i.e. no control. The inertial mass properties are set to match the Follower spacecraft, but have no influence on the simulation results. The Leader has a mass of 1100 kilograms. The cross-sectional area for determining solar pressure is 6 meters^2 with a reflectivity of 1.4.

4.1.3.2 Follower Spacecraft

The Follower mass is 2200 kilograms. The cross-sectional area for determining solar pressure is 8 meters^2 with a reflectivity of 1.4. Thruster positions and orientations are depicted Figure 4.1 and detailed in Table 4.1.

The inertia matrix for the Follower is given by:

$$\boldsymbol{H_R} = \begin{bmatrix} 200 & 10 & 5 \\ 10 & 300 & 15 \\ 5 & 15 & 200 \end{bmatrix} \text{kg m}^2 \tag{4.1}$$

Table 4.1: Simulation Model Thruster Firing Direction and Location

Thruster Number	Firing Direction	Thruster Location (meters)		
		X-Axis	Y-Axis	Z-Axis
F1	-Y-axis	0	+0.5	-0.5
F2	-Y-axis	0	+0.5	+0.5
F3	+Y-axis	0	-0.5	-0.5
F4	+Y-axis	0	-0.5	+0.5
F5	-X-axis	+0.5	-0.5	0
F6	-X-axis	+0.5	+0.5	0
F7	+X-axis	-0.5	-0.5	0
F8	+X-axis	-0.5	+0.5	0
F9	-Z-axis	-0.5	0	+0.5
F10	-Z-axis	+0.5	0	+0.5
F11	+Z-axis	-0.5	0	-0.5
F12	+Z-axis	+0.5	0	-0.5

4.1.4 Thruster Biasing

As discussed in Section 3.4, the thruster layout must meet two criteria. For this design the control sensitivity matrix is defined as:

$$
\boldsymbol{B}_{thrust} =
\begin{bmatrix}
0 & 0 & 0 & 0 & -1 & -1 & 1 & 1 & 0 & 0 & 0 & 0 \\
-1 & -1 & 1 & 1 & 0 & 0 & 0 & 0 & 0 & 0 & 0 & 0 \\
0 & 0 & 0 & 0 & 0 & 0 & 0 & 0 & -1 & -1 & 1 & 1 \\
-0.5 & 0.5 & 0.5 & -0.5 & 0 & 0 & 0 & 0 & 0 & 0 & 0 & 0 \\
0 & 0 & 0 & 0 & 0 & 0 & 0 & 0 & -0.5 & 0.5 & 0.5 & -0.5 \\
0 & 0 & 0 & 0 & -0.5 & 0.5 & 0.5 & -0.5 & 0 & 0 & 0 & 0
\end{bmatrix}
$$

It is straight forward to show $(\boldsymbol{B}_{thrust}\, \boldsymbol{B}_{thrust}{}^{\mathsf{T}})$ is invertible.

One set of conforming basis vectors for $\boldsymbol{F}_{bias}$ is:

$$[\ 1\ 0\ 1\ 0\ 0\ 0\ 0\ 0\ 0\ 0\ 0\ 0\ ]^{\mathsf{T}}$$

$$[\ 0\ 1\ 0\ 1\ 0\ 0\ 0\ 0\ 0\ 0\ 0\ 0\ ]^{\mathsf{T}}$$

$$[\ 0\ 0\ 0\ 0\ 1\ 0\ 1\ 0\ 0\ 0\ 0\ 0\ ]^{\mathsf{T}}$$

$$[\ 0\ 0\ 0\ 0\ 0\ 0\ 1\ 0\ 1\ 0\ 0\ 0\ 0\ ]^{\mathsf{T}}$$

$$[\ 0\ 0\ 0\ 0\ 0\ 0\ 0\ 0\ 1\ 0\ 1\ 0\ ]^{\mathsf{T}}$$

$$[\ 0\ 0\ 0\ 0\ 0\ 0\ 0\ 0\ 0\ 1\ 0\ 1\ ]^{\mathsf{T}}$$

Therefore the selected thruster configuration is suitable for implementing full 6DOF control.

4.1.5   Initial Conditions

The simulation is based on the benchmark mission defined in [5]. Analysis considers two scenarios to represent a close formation (50 meter separation) versus a distant formation (100 kilometers). The nominal formation is initialized in a stabilizable orbit about the L_2 point in the Earth/Moon-Sun system with a transverse (Y-axis) amplitude of 300,000 kilometers, and a normal (Z-axis) amplitude of 200,000 kilometers. The initial state of the Leader is defined as:

Epoch: October 1, 2004, 12 noon, (UTC)

Position (km, J2000 coordinates, Earth Equator):

[1404758.1805532565, 103765.03812730288, 262972.11578260816]

Velocity (km/sec, J2000 coordinates, Earth Equator):

[-.063208398706927252, .36421914258386690, .16244834559859272]

The Follower is initialized with the same velocity vector as the Leader with the position vector offset from the Leader position. The offset is scenario specific.

4.2   Control Design

Linear control gains are computed using MATLAB's $\mathbf{lqr}(\boldsymbol{A_{\mathrm{LQR}}}, \boldsymbol{B}, \boldsymbol{Q}, \boldsymbol{R})$ routine. The algorithm determines the gain which minimizes the cost function discussed in Section 3.1.1.2. $\boldsymbol{A}_{LQR}$ is constructed with diagonal partitions representing the translational and attitude dynamics, expressed in Equations 3.19 and 3.39, respectively.

The structure appears as:

$$
\boldsymbol{A}_{LQR} = \begin{bmatrix} \boldsymbol{A}_{translation} & \boldsymbol{0} \\ \boldsymbol{0} & \boldsymbol{A}_{attitude} \end{bmatrix}
$$

$\boldsymbol{A}_{translation}$ is computed from Equation 3.20, evaluated with initial state properties. With $\boldsymbol{Q}$ and $\boldsymbol{R}$ defined as diagonal matrices, the LQR design generates a gain matrix with five submatrices, structured as:

$$
\boldsymbol{K}_{LQR} = \begin{bmatrix} \boldsymbol{K}_{i,trans} & \boldsymbol{0} & \boldsymbol{0} & \boldsymbol{0} & \boldsymbol{0} \\ \boldsymbol{0} & \boldsymbol{K}_{p,trans} & \boldsymbol{0} & \boldsymbol{0} & \boldsymbol{0} \\ \boldsymbol{0} & \boldsymbol{0} & \boldsymbol{K}_{d,trans} & \boldsymbol{0} & \boldsymbol{0} \\ \boldsymbol{0} & \boldsymbol{0} & \boldsymbol{0} & \boldsymbol{K}_{p,att} & \boldsymbol{0} \\ \boldsymbol{0} & \boldsymbol{0} & \boldsymbol{0} & \boldsymbol{0} & \boldsymbol{K}_{d,att} \end{bmatrix}
$$

The indices i, p and d designate the integral, proportional and derivative gains, respectively.

The gains for the nonlinear controller, Equation 3.44, are computed to match the linear control gains, minimizing gain selection as a factor in the comparative analysis. Recall the nonlinear controller includes the term $\boldsymbol{K}_D \boldsymbol{s} = \boldsymbol{K}_D(\dot{\tilde{\boldsymbol{\xi}}} + \boldsymbol{\Lambda}\tilde{\boldsymbol{\xi}})$. In the nonlinear controller $\boldsymbol{K}_D$ is the equivalent derivative gain, and $\boldsymbol{K}_D\boldsymbol{\Lambda}$ is the equivalent proportional gain. Therefore, the nonlinear gains are computed as:

$$
\begin{aligned}
\boldsymbol{K}_{D,trans} &= \boldsymbol{K}_{d,trans}; & \boldsymbol{\Lambda}_T &= [\boldsymbol{K}_{d,trans}]^{-1}\boldsymbol{K}_{p,trans} \\
\boldsymbol{K}_{D,att} &= \boldsymbol{K}_{d,att}; & \boldsymbol{\Lambda}_R &= [\boldsymbol{K}_{d,att}]^{-1}\boldsymbol{K}_{p,att}
\end{aligned}
$$

Note: There is no equivalent integrator gain, $\boldsymbol{K_i}$, in the nonadaptive nonlinear controller design. Excluding perturbations, the nonadaptive nonlinear control design incorporates all the known dynamics, eliminating the need for an integrator feature. Linear control integrator gain equivalence with the adaptive nonlinear control design is discussed in Chapter 6.

The values of $\boldsymbol{Q}$ and $\boldsymbol{R}$ used in the LQR design are:

$$\boldsymbol{Q} = \begin{bmatrix} Q_{trans,I}\,\mathbf{I_3} & \mathbf{0} & \mathbf{0} & \mathbf{0} & \mathbf{0} \\ \mathbf{0} & Q_{trans,P}\,\mathbf{I_3} & \mathbf{0} & \mathbf{0} & \mathbf{0} \\ \mathbf{0} & \mathbf{0} & Q_{trans,D}\,\mathbf{I_3} & \mathbf{0} & \mathbf{0} \\ \mathbf{0} & \mathbf{0} & \mathbf{0} & Q_{att,P}\,\mathbf{I_3} & \mathbf{0} \\ \mathbf{0} & \mathbf{0} & \mathbf{0} & \mathbf{0} & Q_{att,D}\,\mathbf{I_3} \end{bmatrix}$$

$$\boldsymbol{R} = \begin{bmatrix} R_{trans}\,\mathbf{I_3} & \mathbf{0} \\ \mathbf{0} & R_{att}\,\mathbf{I_3} \end{bmatrix}$$

Where:

$Q_{trans,I} = 10^{-4}$; $Q_{trans,P} = 1$; $Q_{trans,D} = 1$; $Q_{att,P} = 10^3$; $Q_{att,D} = 10^3$

$R_{trans} = 1$; $R_{att} = 1$

The specific selection of the values for $\boldsymbol{Q}$ and $\boldsymbol{R}$ is based on a series of trial simulations. Considering the diagonal elements of $\boldsymbol{Q}$: $Q_{trans,I}$, $Q_{trans,P}$ and $Q_{trans,D}$ are the weighting on integrated position, position and velocity errors in translation,

respectively; and $Q_{att,P}$ and $Q_{att,D}$ are the weighting on the attitude error and rate error, respectively. For $\boldsymbol{R}$, R_{trans} is the weighting on the translation control; and R_{att} is the weighting on the attitude control. Position/velocity error weighting, $Q_{trans,P}$ and $Q_{trans,D}$, balance the influence of observed errors in determining the translation control. Likewise, attitude/rate error weighting, $Q_{att,P}$ and $Q_{att,D}$, balances the influence on the torque command. Weighting on the integrated translation error, $Q_{trans,P}$, is selected to provide reasonable convergence and tracking of the bias force due to gravity and solar pressure.

The LQR design algorithm is based on the values of $\boldsymbol{A}$ and $\boldsymbol{B}$ from the system dynamics model. For this design coupling of the translation and attitude dynamics is introduced only through $\boldsymbol{B}$. However, with the specific thruster design, translation/attitude coupling action has been eliminated. Translation and attitude coupling occurs only if the thrusters are misaligned. From an LQR design perspective uncoupled translation/attitude dynamics (ideal) implies the relative weighting between the translation and attitude components of $\boldsymbol{Q}$ and $\boldsymbol{R}$, has no effect on the computed value of $\boldsymbol{K_{LQR}}$.

The closed-loop gain for the linear control design is presented in Section 3.2.2.2. As discussed the system is considered well-posed and robustly stable provided the control law is updated within a 14 day period.

The closed-loop gain profiles are shown in Figures 4.2 and 4.3.

94
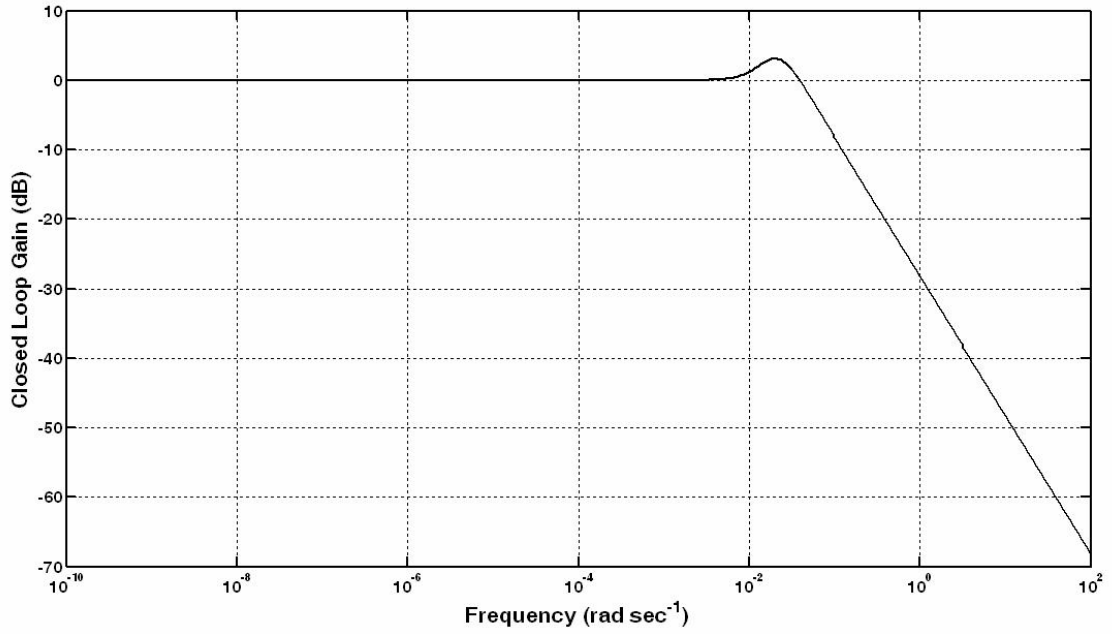
Figure 4.2: Linear Translation Control: Closed-Loop Gain, all-channels
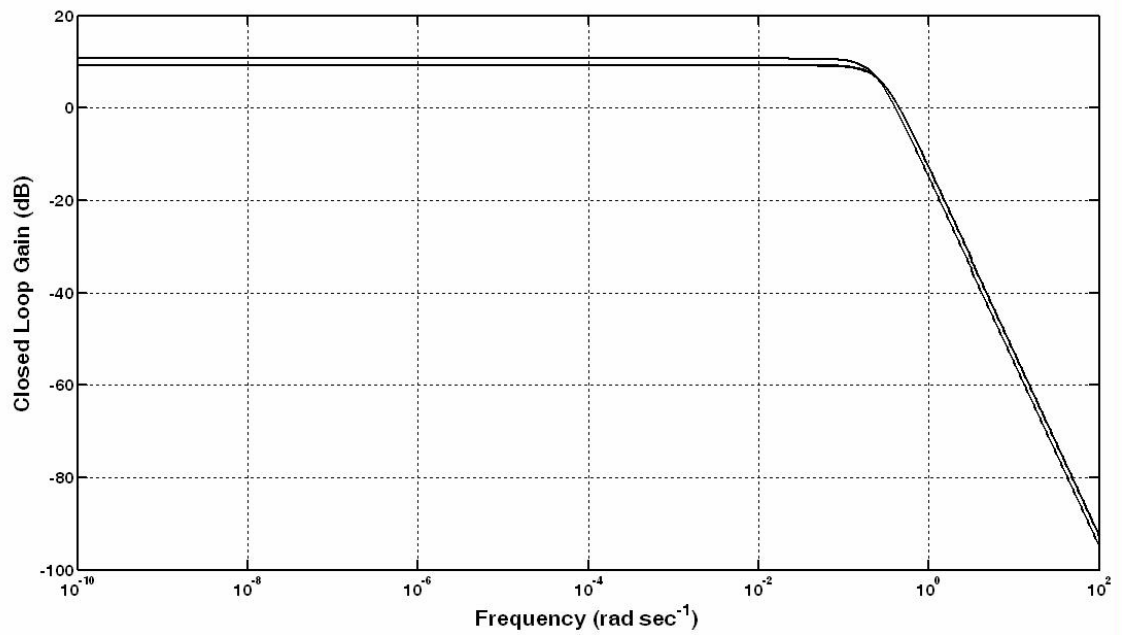
Figure 4.3: Linear Attitude Control: Closed-Loop Gain, all-channels

4.3   Scenario 1 – Distant Formation, 100 Kilometer Range

For the distant formation the Follower position is initialized with a 95 kilometer separation along the inertial X-axis. During the first segment of the simulation, control is applied to maintain the relative position and attitude at the initial values. Subsequently, three maneuvers are commanded: pure translation, pure attitude, combined translation and attitude. Translation maneuvers are along the direction of the initial range vector. Attitude maneuvers are rotations about a common Euler axis. The translation and attitude maneuver profiles are depicted in Figures 4.4 and 4.5, respectively. Excluding solar pressure effects, the ideal (perfect tracking) control effort, based on the design scenario, is included in Figures 4.4 and 4.5. Table 4.3 includes the ideal fuel requirement. Solar pressure effects are neglected in the simulation to demonstrate the unperturbed performance of each controller. The linear controller employs the integrator to compensate for unmodeled gravity sources. In contrast the nonlinear controller incorporates all gravity sources controller design. The sequence of maneuvers are detailed in the table below.

COMMANDED MANEUVER SEQUENCE

Simulation Time	Commanded Maneuver
0→5 minutes:	Maintain Steady State
5→65 minutes:	Increase Range to 100 km
65→75 minutes:	Maintain Steady State
75→95 minutes:	90 Degree Attitude Slew
95→105 minutes:	Maintain Steady State
105→165 minutes:	Decrease Range to 90 km
	-90 Degree Attitude Slew
165→175 minutes:	Maintain Steady State
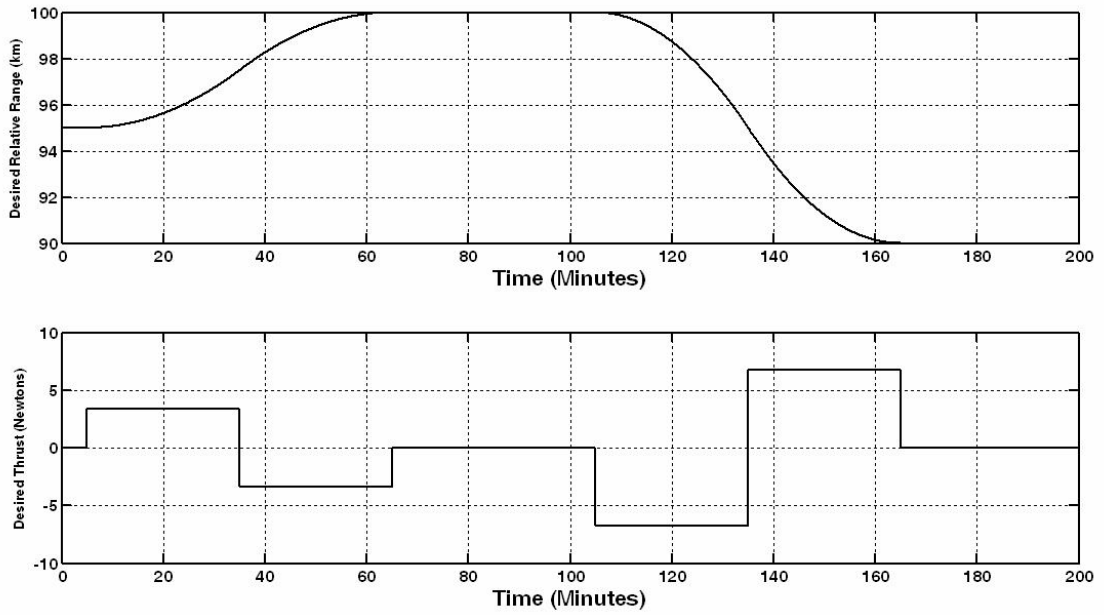
Figure 4.4: Profiles of Desired Leader/Follower Range along Separation Vector (Inertial X-axis), and Ideal (Perfect Tracking) Control
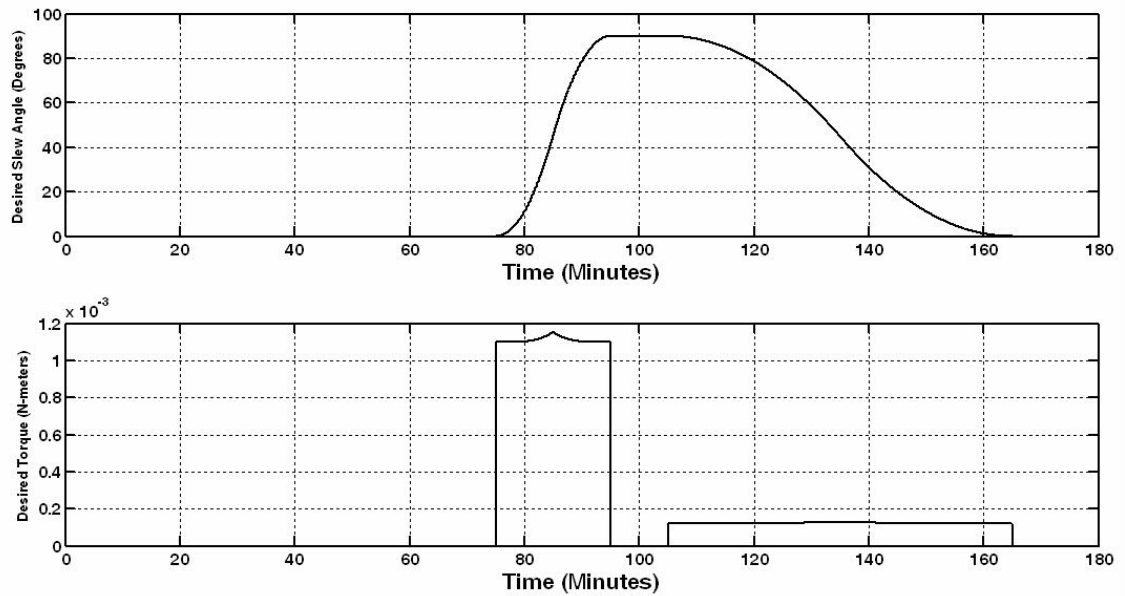
Figure 4.5: Desired Slew Angle for Follower and Ideal (Perfect Tracking) Torque Profile about Rotation Axis

The simulation demonstrates the performance advantage of the nonlinear control design. Figure 4.6 depicts the translational trajectory tracking performance. The linear controller exhibits a transient response at the beginning of each interval of planned maneuver steps. In contrast the nonlinear controller, incorporating desired state information, demonstrates significantly superior tracking, with a mean error 10^5 times smaller than the linear controller. Specific performance metrics are provided in Table 4.2. The position error fluctuations observed for the nonlinear controller during the initial 100 minutes reflect the limit of numerical precision for the simulation, approximately 10^{-8} meters. The translation tracking performance for both controller types degrades during the combined translation/attitude maneuver. This effect is attributed to the discrete nature of the simulation. Translation commands assume the spacecraft maintains a fixed attitude during each propagation interval. Discrete modeling of the simultaneous attitude maneuver has the effect of generating a thruster misalignment which degrades the tracking performance. A similar effect is observed in Figure 4.7 for attitude tracking.

Table 4.2: Scenario 1 – Controller Tracking Performance Summary

	Error			
Controller Type	Minimum	Maximum	Mean	Units
Linear Translation	$< 10^{-8}$ *	10^1	3.4×10^{-1}	meters
Nonlinear Translation	$< 10^{-8}$ *	10^{-5}	2.4×10^{-6}	meters
Linear Attitude	10^{-11}	10^1	1.9×10^0	arcsec
Nonlinear Attitude	$< 10^{-11}$ *	10^{-2}	3.8×10^{-4}	arcsec

* Reflects limit of numerical precision.
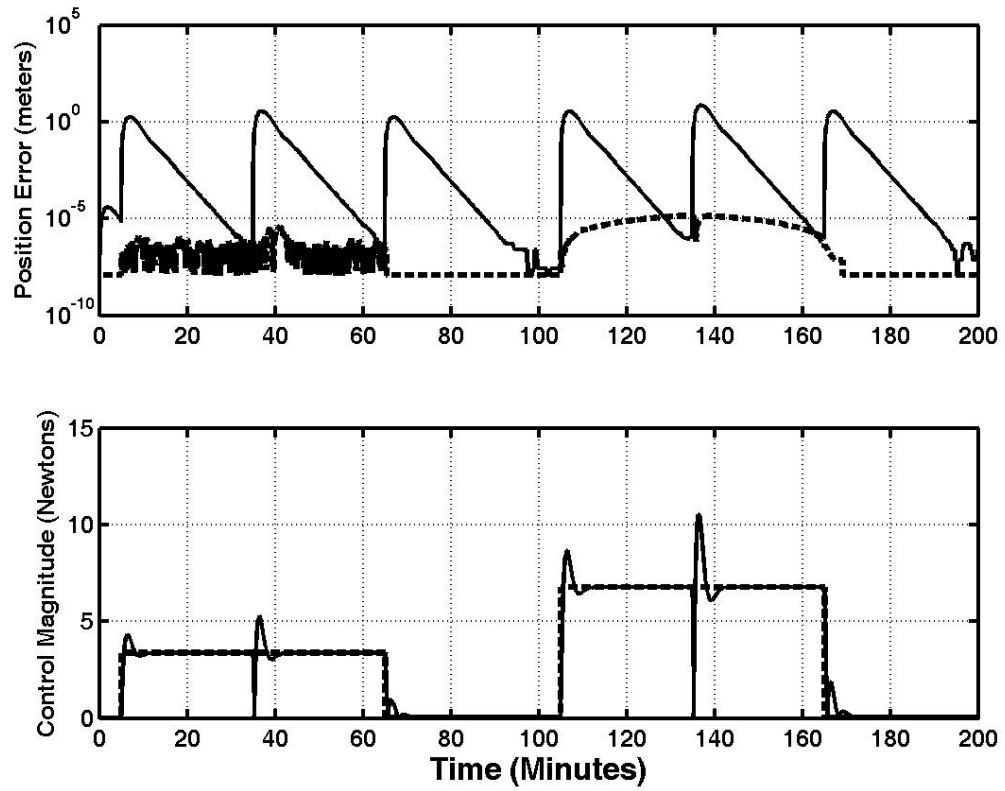
Figure 4.6: Range Error and Translation Control Profile for Linear (solid) and Nonlinear(dashed) Control Algorithms
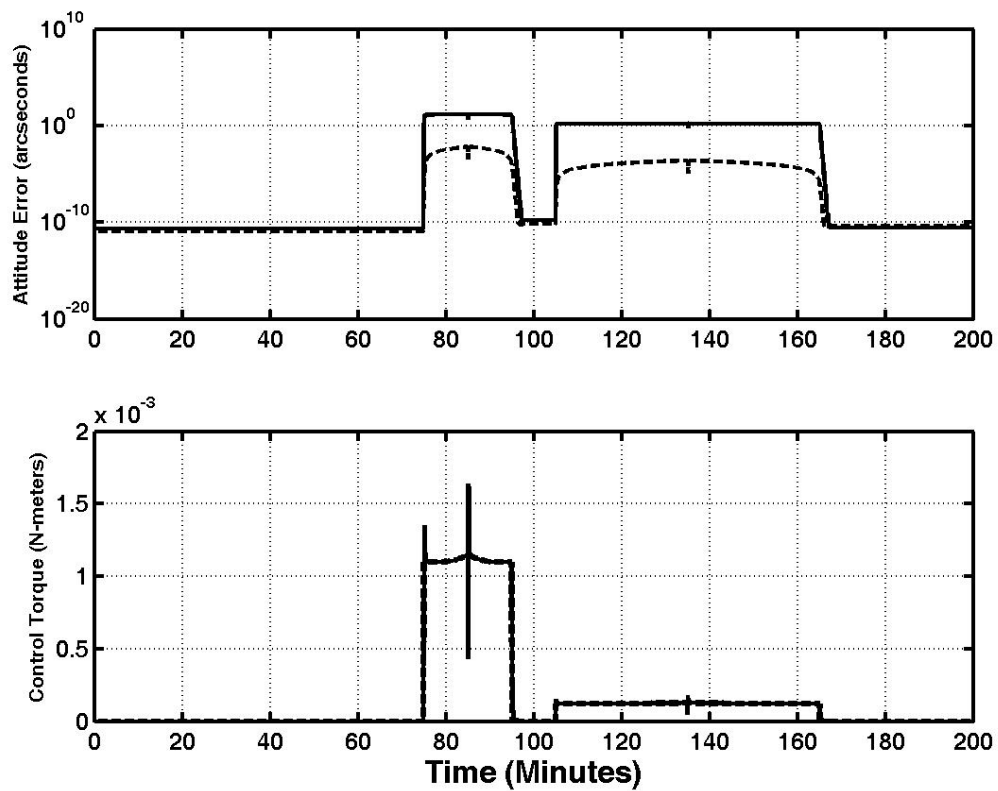
Figure 4.7: Attitude Error and Torque Control Profile for Linear (solid) and Nonlinear(dashed) Control Algorithms

Figure 4.8 and Table 4.3 compare the fuel requirement for each controller. The nonlinear controller performs with higher fuel efficiency. In fact the nonlinear controller consumes slightly less fuel than required for perfect tracking. This benefit is derived from the inability of the controller to perfectly track instantaneous changes in the velocity/attitude rate profile. The instantaneous thrust profile of the linear controller indicates the transient response is the principal factor in the degradation in fuel efficiency.
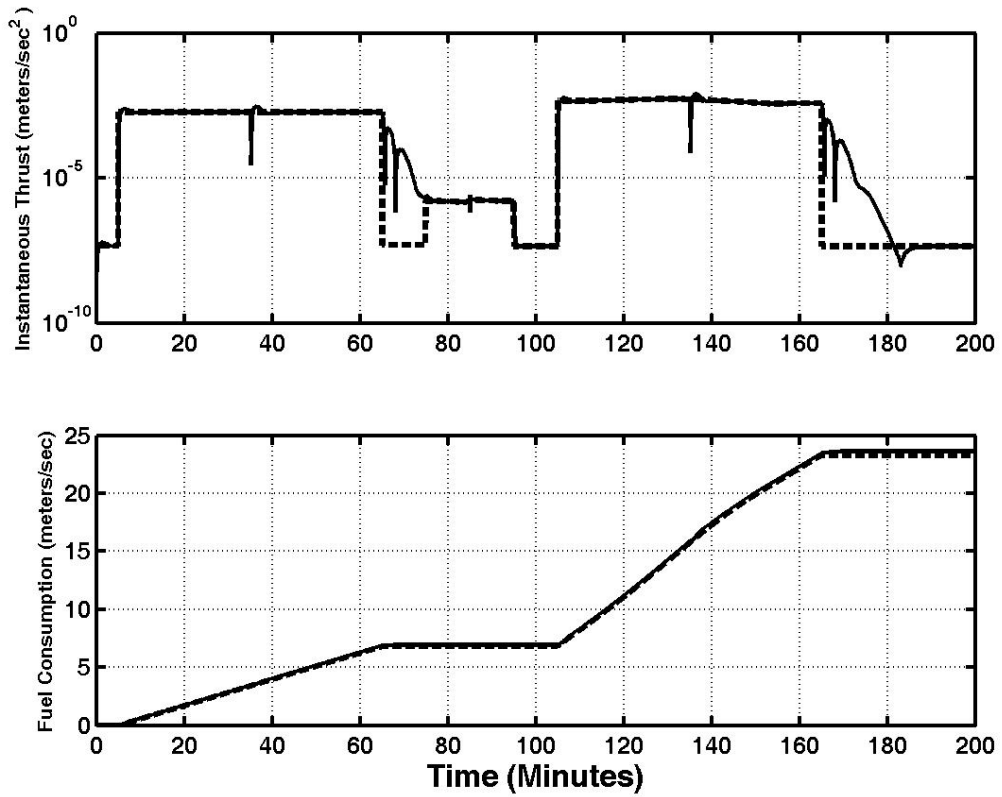
Figure 4.8: Instantaneous Thrust Level and Fuel Consumption for Linear (solid) and Nonlinear(dashed) Control Algorithms

Table 4.3: Scenario 1 – Controller Fuel Performance Summary

Controller Type	Fuel Consumption (meters/second)	Deviation from Ideal (Perfect Tracking) (Percent)
Ideal Translation/Attitude	23.25535	–
Linear Translation/Attitude	23.63285	+1.6%
Nonlinear Translation/Attitude	23.25498	-0.002%

101

4.4 Scenario 2 – Close Formation, 50 Meter Range

For the close formation the Follower is initially positioned from the Leader with a 75 meter range along the inertial X-axis. The maneuver scheme is similar to Scenario 1. The attitude maneuver, depicted in Figure 4.5, is the same for both scenarios. The translation maneuver follows the same time sequence with shorter range changes, as shown in Figure 4.9. The sequence of maneuvers for the close formation are tabulated as:

Simulation Time	Commanded Maneuver
0→5 minutes:	Maintain Steady State
5→65 minutes:	Decrease Range to 50 meters
65→75 minutes:	Maintain Steady State
75→95 minutes:	90 Degree Attitude Slew
95→105 minutes:	Maintain Steady State
105→165 minutes:	Increase Range to 100 meters
	-90 Degree Attitude Slew
165→175 minutes:	Maintain Steady State
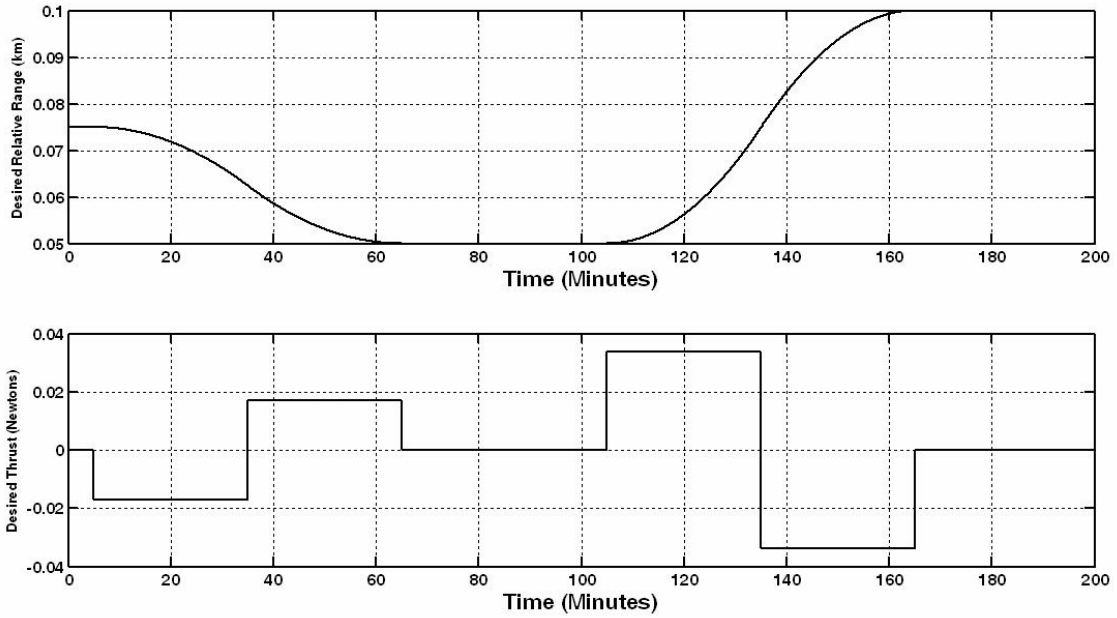
Figure 4.9: Desired Leader/Follower Range and Ideal (Perfect Tracking) Control Profile

The controller performance is shown in Figures 4.10, 4.11 and 4.12. Tables 4.4 and 4.5 provide numerical performance metrics. As expected, both controllers demonstrate improved translation trajectory tracking compared to the results in Section 4.3. Linear controller translation tracking improved by two orders of magnitude. Nonlinear translation tracking improved by one order of magnitude. The result is attributed to the significant reduction in the range change during the maneuver, 10's of meters versus kilometers. Similar degradation in translation tracking performance is observed for both controllers during the combined translation/attitude maneuver. Unaffected by relative spacecraft range, attitude tracking performance is similar for both scenarios. While the overall fuel requirement is reduced for scenario 2, both scenarios exhibit similar fuel efficiency relative to the ideal (perfect tracking), Table 4.5.

103
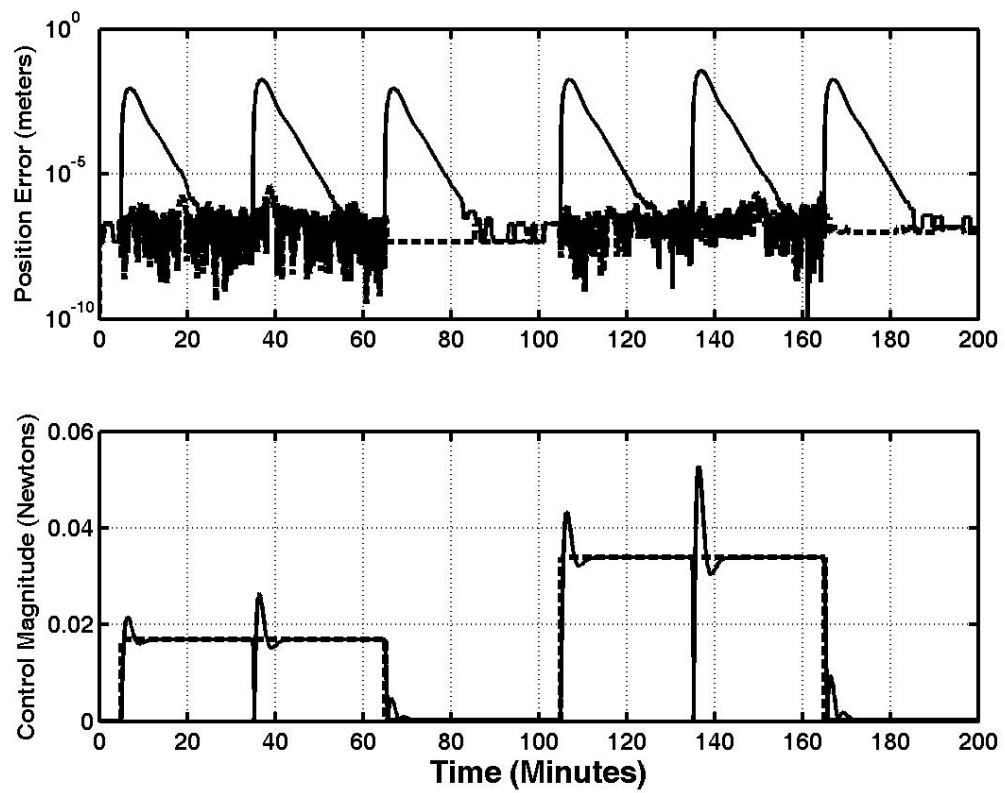
Figure 4.10: Range Error and Translation Control Profile for Linear (solid) and Nonlinear(dashed) Control Algorithms
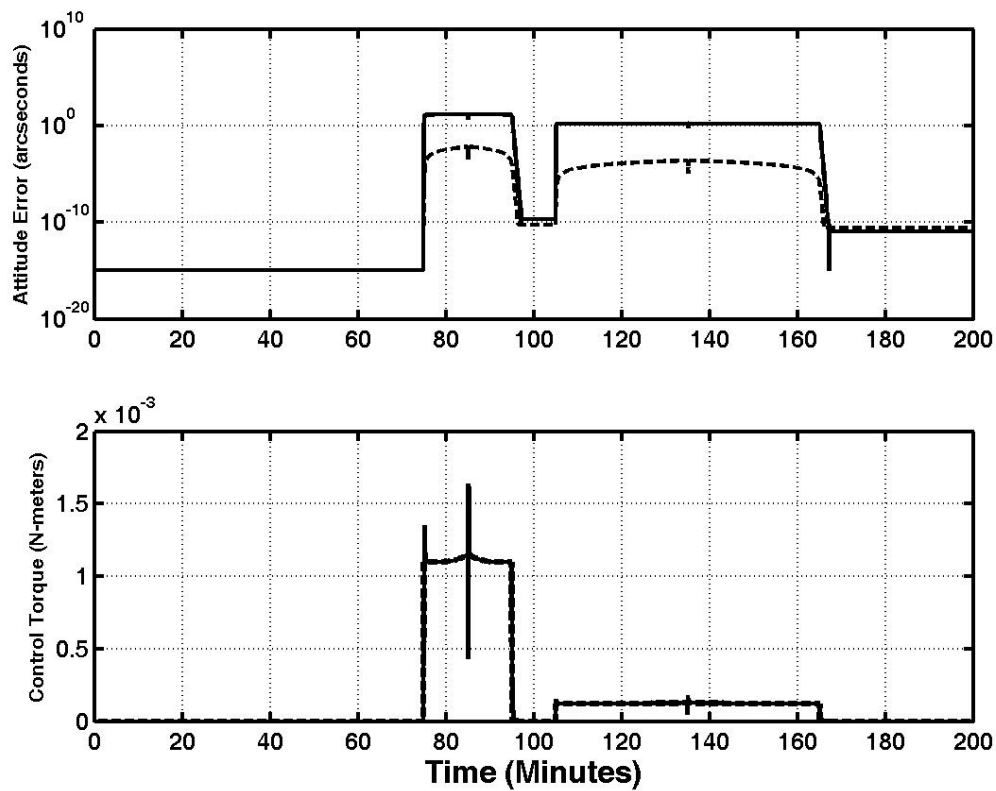
Figure 4.11: Attitude Error and Torque Control Profile for Linear (solid) and Nonlinear(dashed) Control Algorithms

Table 4.4: Scenario 2 – Controller Tracking Performance Summary

			Error	
Controller Type	Minimum	Maximum	Mean	Units
Linear Translation	$< 10^{-8}$ *	10^{-2}	1.7×10^{-3}	meters
Nonlinear Translation	$< 10^{-8}$ *	10^{-6}	2.4×10^{-7}	meters
Linear Attitude	$< 10^{-11}$	10^{1}	1.9×10^{0}	arcsec
Nonlinear Attitude	$< 10^{-11}$ *	10^{-2}	3.8×10^{-4}	arcsec

* Reflects limit of numerical precision.
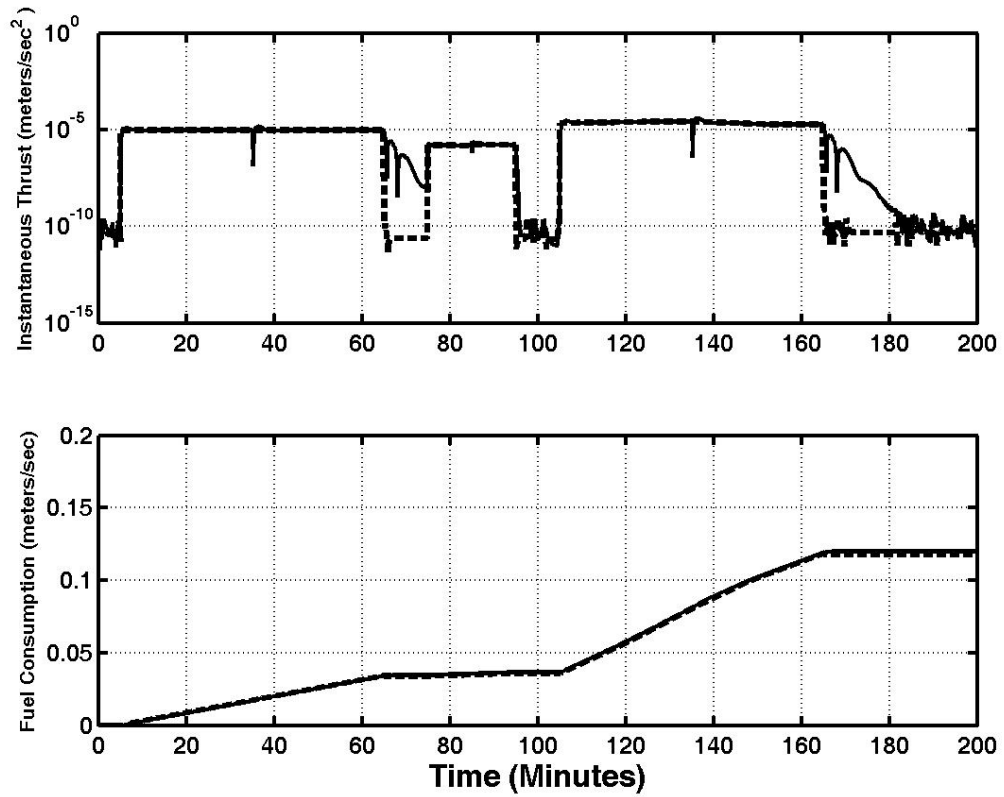
Figure 4.12: Instantaneous Thrust Level and Fuel Consumption for Linear (solid) and Nonlinear(dashed) Control Algorithms

Table 4.5: Scenario 2 – Controller Fuel Performance Summary

Controller Type	Fuel Consumption	Deviation from Ideal (Perfect Tracking)
Ideal Translation/Attitude	0.1182103	–
Linear Translation/Attitude	0.1201096	+1.6%
Nonlinear Translation/Attitude	0.1182084	-0.002%

106

4.5 Perturbations

In an ideal environment both linear and nonadaptive nonlinear control strategies provide good performance. This section examines the performance impact due to unmodeled dynamics for Scenario 1, presented in Section 4.3. Perturbation sources include: solar pressure, mass uncertainty and thruster placement/alignment uncertainty. Additionally, the impact of assumed time invariant dynamics is assessed by modeling maneuver performance 28 days after the scenario epoch. Chapter 6 details the modeling of each perturbation.

4.5.1 Compensation for Solar Pressure

Solar pressure generates an unmodeled differential acceleration between the Leader and Follower spacecraft. The position tracking performance comparison for the linear controller is presented in Figure 4.13 and Table 4.6. Compared to the results in Section 4.3, there is no perceptible difference in the performance of the linear controller with the addition of solar pressure effects. This result is attributed to the inclusion of the integrator in the linear controller. The integrator provides a generic adaptive mechanism that compensates for the differential acceleration between the two spacecraft, a combined effect of a gravitational gradient and differential solar pressure.
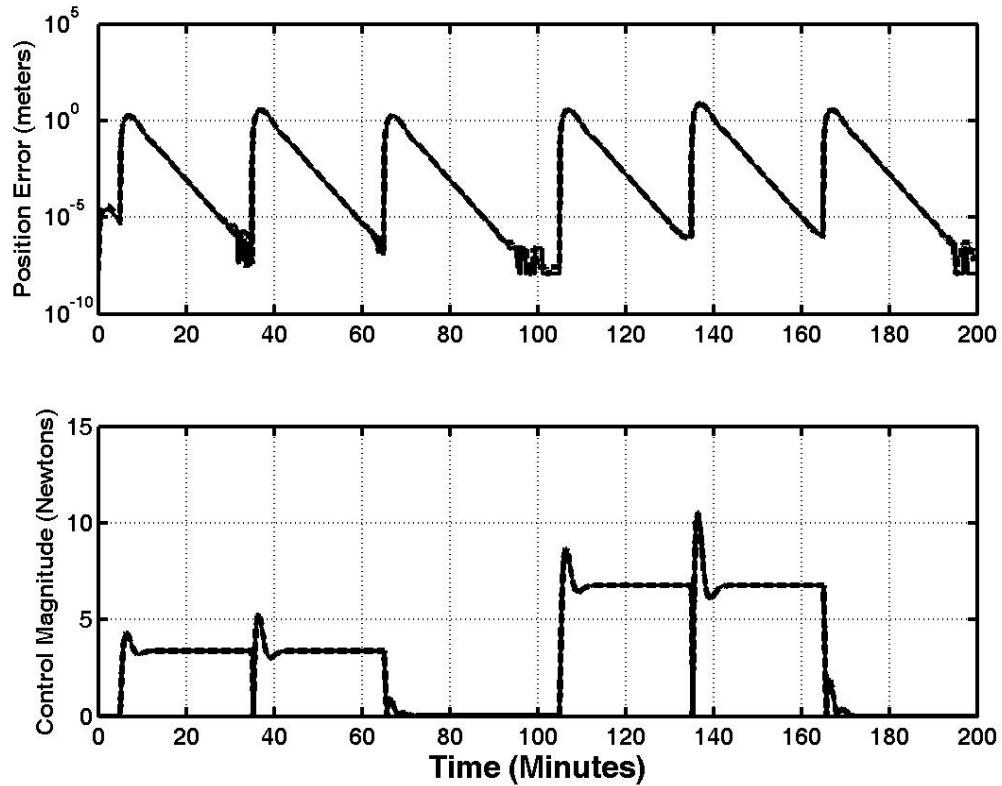
Figure 4.13: Range Error and Translation Control Profile for Linear Controller, Perturbed with Solar Pressure (solid) and Unperturbed (dashed)

In contrast there is a significant impact of the position tracking performance of the nonlinear controller as shown in Figure 4.14 and Table 4.6. An order of magnitude increase is observed in the mean translation tracking error. The nonadaptive nonlinear controller depends on a truth model of the environmental forces. The controller lacks a mechanism to compensate for unmodeled differential solar pressure effects. The nonlinear controller still outperforms the linear controller by several orders of magnitude.

Despite the performance degradation the control effort follows a similar profile

for both the perturbed and unperturbed cases. This is expected since the control effort is principally governed by the desired trajectory. Thus, with reasonable tracking performance, the actual control profile must correlate with the ideal (perfect tracking) control, Figures 4.4 and 4.5.
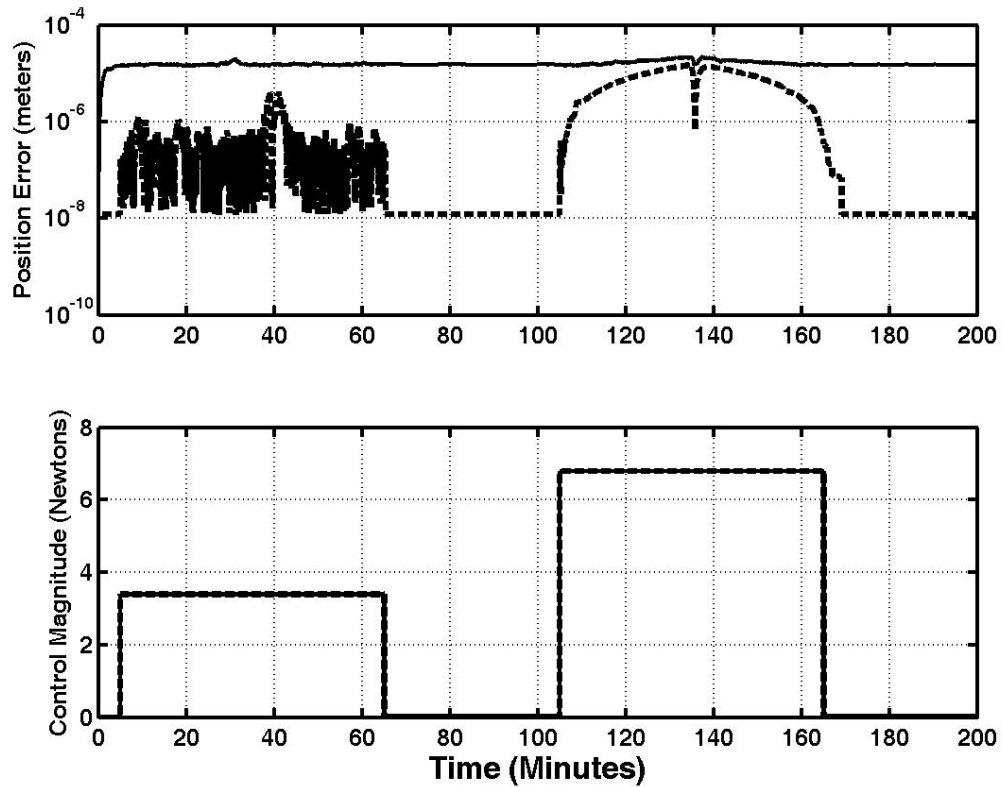
Figure 4.14: Range Error and Translation Control Profile for Nonlinear Controller, Perturbed with Solar Pressure (solid) and Unperturbed (dashed)

As modeled, there is no torque generated by solar pressure, thus the attitude tracking performance, Figure 4.14 and Table 4.6, for both the linear and nonlinear controllers is unchanged from the results presented in Section 4.3.

Table 4.6: Scenario 1 with Solar Perturbation – Controller Tracking Performance Summary

		Error		
Controller Type	Minimum	Maximum	Mean	Units
Linear Translation	$< 10^{-8}$ *	10^1	3.4×10^{-1}	meters
Nonlinear Translation	10^{-5}	10^{-5}	1.6×10^{-5}	meters
Linear Attitude	$< 10^{-11}$	10^1	1.9×10^0	arcsec
Nonlinear Attitude	$< 10^{-11}$ *	10^{-2}	3.8×10^{-4}	arcsec

* Reflects limit of numerical precision.

4.5.2   Compensation for Mass Property Uncertainty

Uncertainty in the spacecraft mass properties is introduced as an error in the overall spacecraft mass estimate, as well as the inertial properties. Modeling details for mass uncertainty are discussed in Section 6.2.2. Uncertainty in the spacecraft mass affects translation control performance, shown in Figure 4.15 and Table 4.7.

Uncertainty in the inertial mass properties affects attitude tracking performance, shown in Figure 4.16 and Table 4.7.

As with solar pressure, the linear controller exhibits the ability to compensate for mass uncertainty for both translation and attitude tracking, as evidenced by the tracking performance metrics in Table 4.6. In contrast the performance of the nonlinear controller is significantly degraded for both position and attitude tracking. Nonlinear translation mean tracking error is increased by 5 orders of

110

magnitude, attitude tracking increases by 3 orders of magnitude. However, the nonlinear controller still outperforms the linear controller based on mean tracking error. The linear controller provides superior steady state tracking error, evidenced by the minimum tracking error.
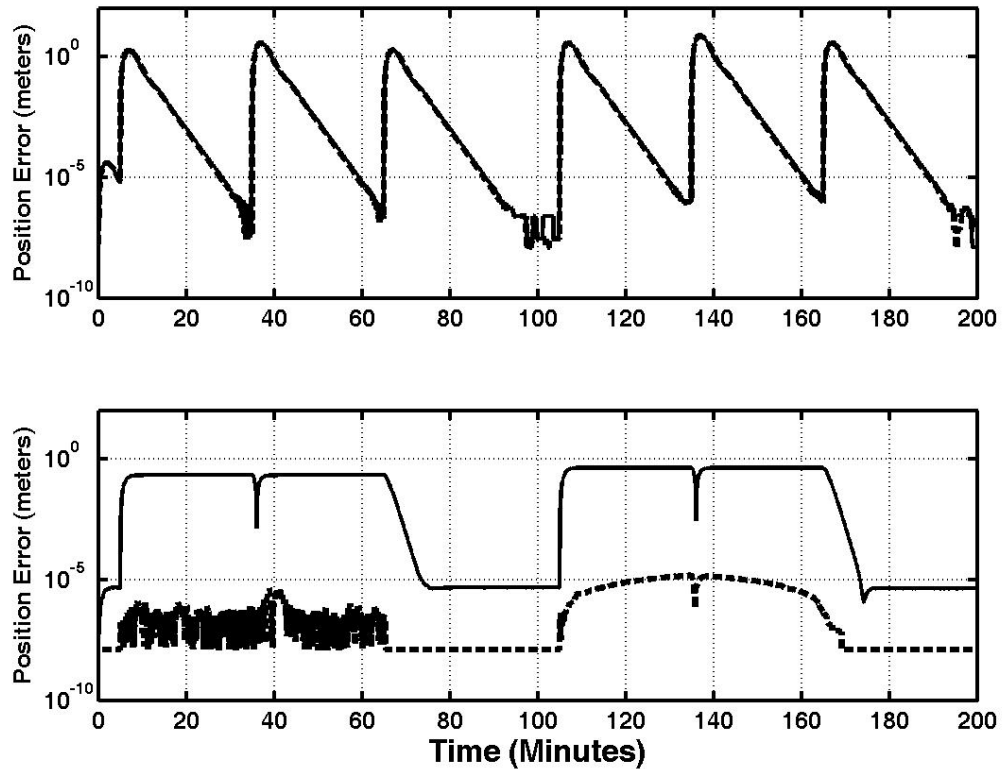
Figure 4.15: Range Error Profile Comparison with Mass Uncertainty Effects (solid) and without (dashed) for Linear (top) and Nonlinear (bottom) Control Algorithms
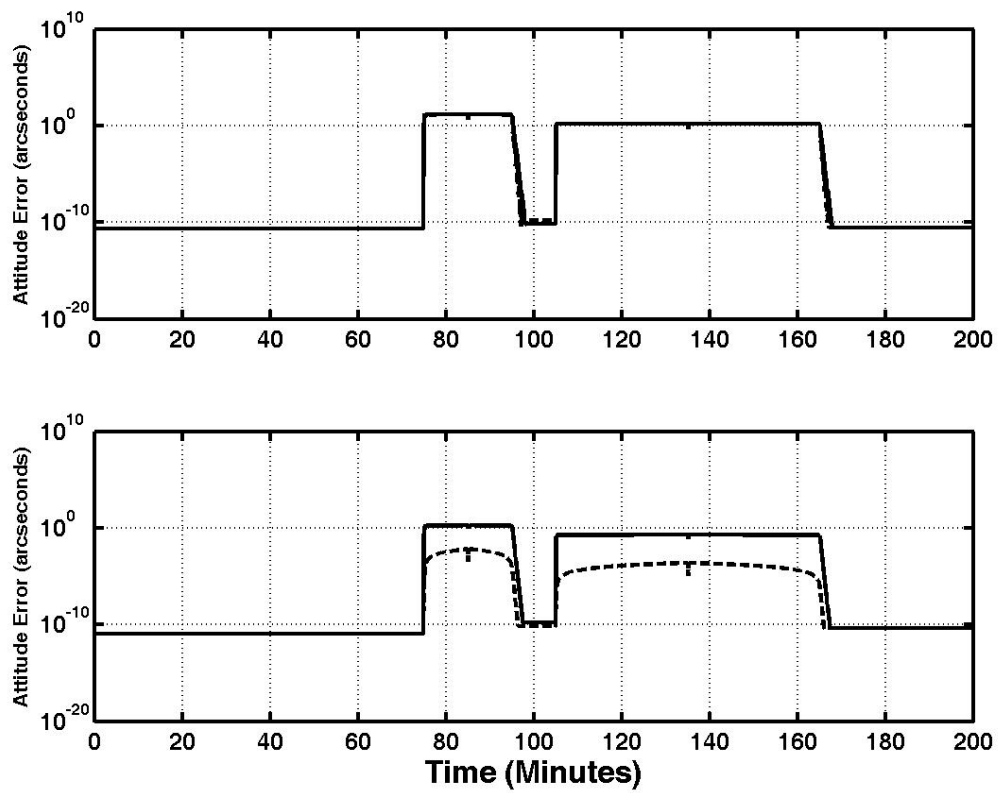
Figure 4.16: Attitude Error Profile Comparison with Mass Uncertainty Effects (solid) and without (dashed) for Linear (top) and Nonlinear (bottom) Control Algorithms

112

Table 4.7: Scenario 1 with Mass Property Uncertainty – Controller Tracking Performance Summary

	Error			
Controller Type	Minimum	Maximum	Mean	Units
Linear Translation	$< 10^{-8}$ *	10^1	3.4×10^{-1}	meters
Nonlinear Translation	10^{-6}	10^{-1}	1.9×10^{-1}	meters
Linear Attitude	10^{-11}	10^1	1.9×10^0	arcsec
Nonlinear Attitude	$< 10^{-11}$ *	10^0	2.4×10^{-1}	arcsec

* Reflects limit of numerical precision.

4.5.3 Compensation for Thruster Misalignment/Misplacement

Errors in thruster alignment and placement specifications affect the mapping of acceleration and torque control commands to thruster firing commands. As a result the actual net acceleration and torque applied to the spacecraft deviates from the desired values. Perturbed and unperturbed performance profiles for the linear and nonlinear controllers are shown in Figure 4.17. Modeling details for thruster misalignment/misplacement are discussed in Section 6.2.3.
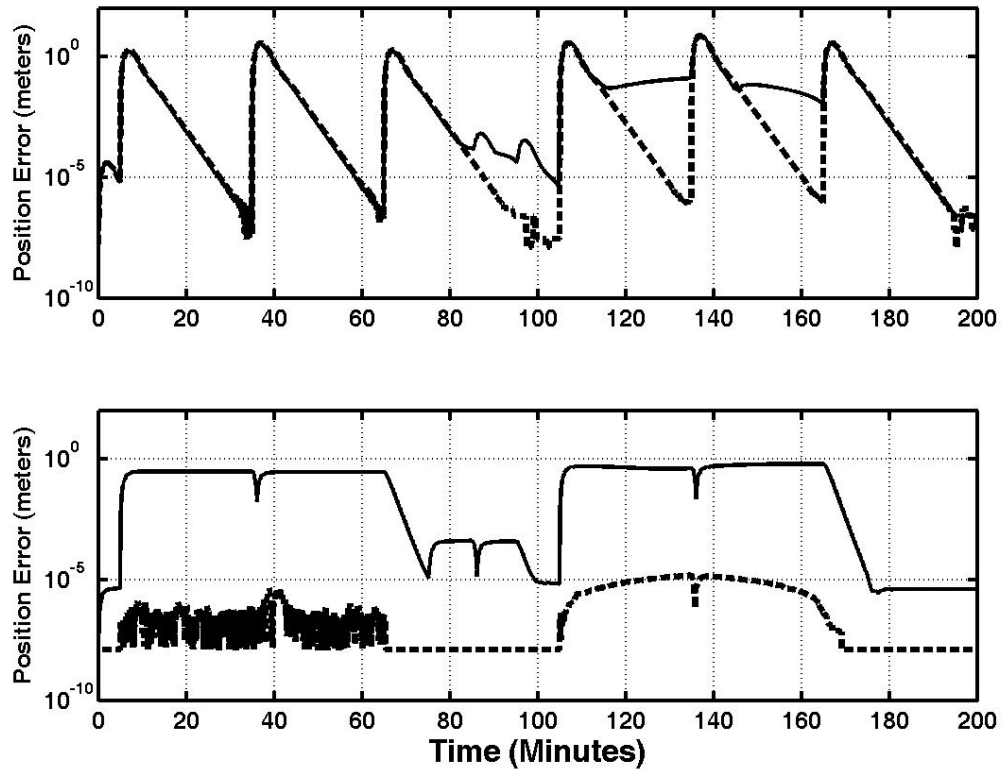
Figure 4.17: Range Error Profile Comparison with Thruster Misalignment/Performance Effects (solid) and without (dashed) for Linear (top) and Nonlinear (bottom) Control Algorithms

The linear controller effectively compensates for thruster misalignment and misplacement during the pure translation maneuver. Performance degradation is manifested during sequences involving attitude maneuvers, indicating a coupling action between translation and attitude control. The nonlinear controller performance significantly degrades during the entire sequence. Thruster misalignment/misplacement significantly impacts attitude tracking performance of both the linear and nonlinear controllers, shown in Figure 4.18. Table 4.8 provides

114

controller performance metrics. Based on the mean error, both controllers have comparable performance for both translation and attitude tracking. The linear system provides an order of magnitude better steady state tracking based on the minimum error. The maximum error for the nonlinear controller is approximately an order of magnitude better than the linear controller.
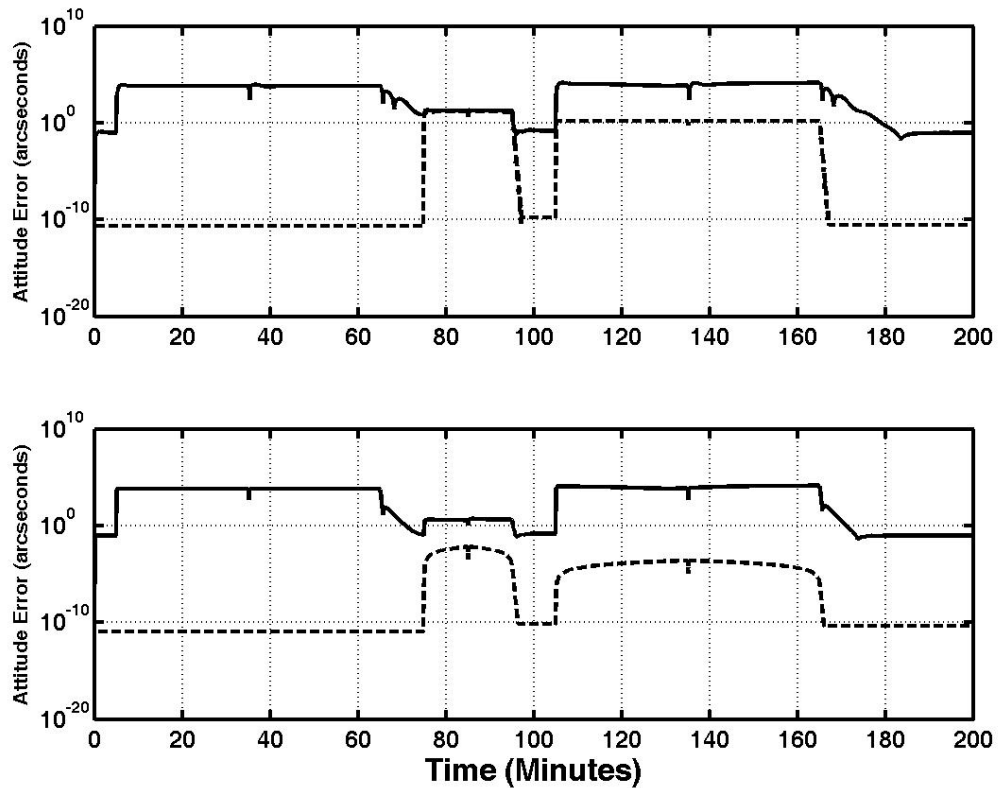
Figure 4.18: Attitude Error Profile Comparison with Thruster Misalignment/Performance Effects (solid) and without (dashed) for Linear (top) and Nonlinear (bottom) Control Algorithms

Table 4.8: Scenario 1 with Thruster Alignment Uncertainty – Controller Tracking Performance Summary

	Error			
Controller Type	Minimum	Maximum	Mean	Units
Linear Translation	10^{-7}	10^1	3.4×10^{-1}	meters
Nonlinear Translation	10^{-6}	10^0	2.3×10^{-1}	meters
Linear Attitude	10^{-2}	10^4	5.2×10^3	arcsec
Nonlinear Attitude	10^{-1}	10^4	5.1×10^3	arcsec

* Reflects limit of numerical precision.

4.5.4 Compensation for Solar Pressure, Mass Properties, Thruster Misalignment/Misplacement

For completeness, the performance of both the linear and nonlinear controllers in the presence of all modeled disturbances is shown in Figures 4.19 and 4.20, and Table 4.9. As expected from previous results, the minimum tracking error indicates the linear controller possesses greater robustness to model uncertainty for steady state tracking. Based on the mean error, the linear and nonlinear controllers have equivalent performance. Comparing results presented in Tables 4.8 and 4.9, thruster alignment/placement uncertainty is the dominant source of performance degradation.
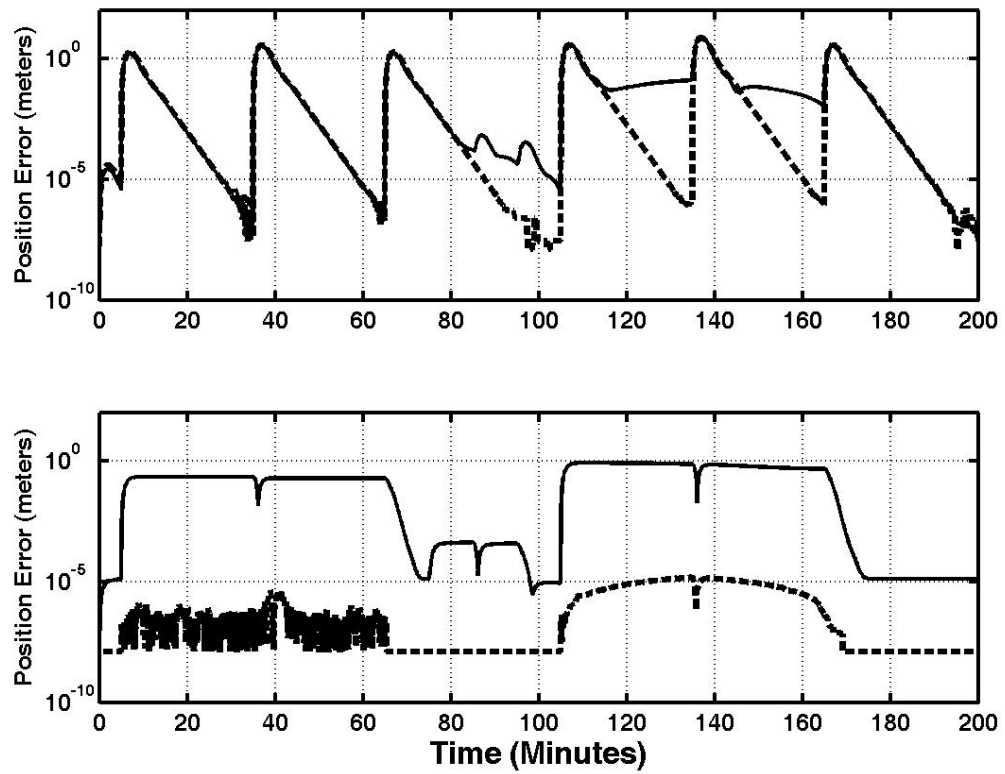
Figure 4.19: Range Error Profile Comparison with All Perturbation Effects (solid) and without (dashed) for Linear (top) and Nonlinear (bottom) Control Algorithms
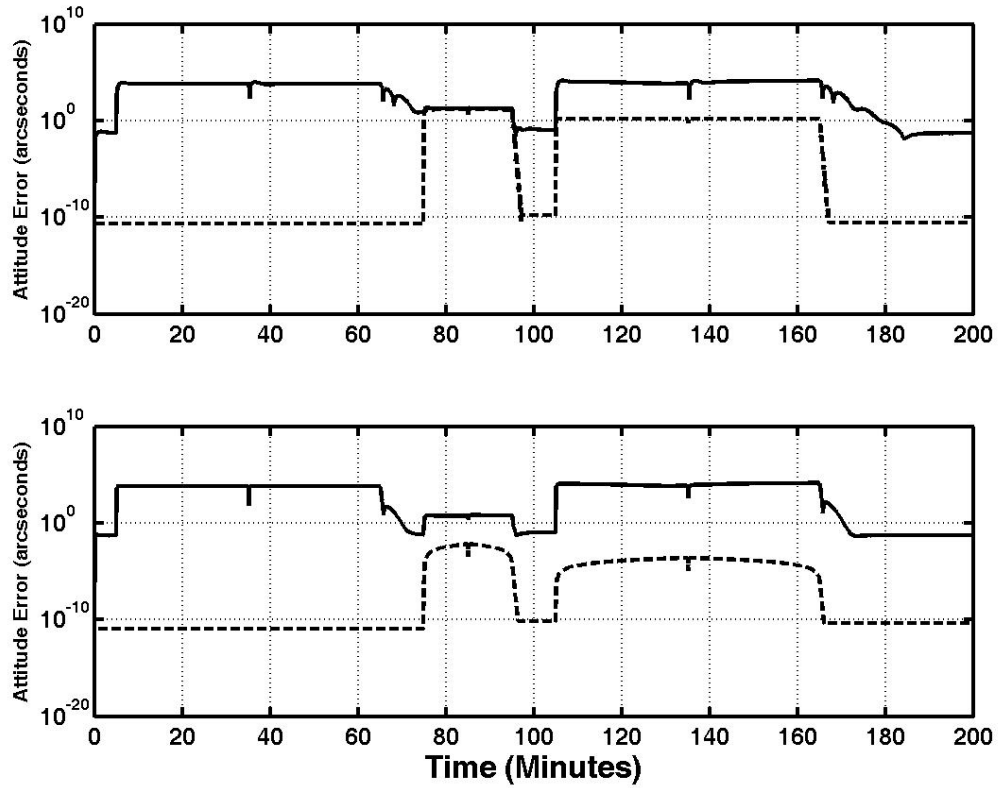
Figure 4.20: Attitude Error Profile Comparison with All Perturbation Effects (solid) and without (dashed) for Linear (top) and Nonlinear (bottom) Control Algorithms

Table 4.9: Scenario 1 with Solar Pressure, Mass Properties, Thruster Alignment/Position Uncertainty – Controller Tracking Performance Summary

Controller Type	Error			
	Minimum	Maximum	Mean	Units
Linear Translation	10^{-8}	10^{1}	3.4×10^{-1}	meters
Nonlinear Translation	10^{-6}	10^{0}	2.6×10^{-1}	meters
Linear Attitude	10^{-2}	10^{4}	5.2×10^{3}	arcsec
Nonlinear Attitude	10^{-2}	10^{4}	5.1×10^{3}	arcsec

118

4.5.5   Performance Impact of Time Invariant Dynamics Model

As discussed in Section 3.2.2.3, the dynamics model for the linear control design is assumed time invariant. The robustness analysis ensured stability provided scheduled gain updates with a frequency of 14 days, or better. However, as a practical matter, linear controller performance is not expected to degrade beyond 14 days, even without gain update. Due to the benign dynamic environment, the natural dynamics do not influence the LQR gains. The LQR design yields diagonal gain matrices for translation control. The gains are equal to those derived with assumed double integrator dynamics. To demonstrate the point, Scenario 1 (with perturbations) is initiated 28 days after the epoch for controller gain computation. Tracking performance, Table 4.10, is unchanged. There is a slight fuel penalty, shown in Table 4.11. Graphically the performance is equivalent to the results presented in Figures 4.6, 4.7, and 4.8.

Table 4.10: Scenario 1, 28 days after Epoch – Linear Controller Tracking Performance Summary

	Error			
Controller Type	Minimum	Maximum	Mean	Units
Linear Translation (delay)	$< 10^{-8}$ *	10^1	3.4×10^{-1}	meters
Linear Translation (no delay)	$< 10^{-8}$ *	10^1	3.4×10^{-1}	meters
Linear Attitude (delay)	$< 10^{-11}$ *	10^1	1.9×10^0	arcsec
Linear Attitude (no delay)	10^{-11}	10^1	1.9×10^0	arcsec

* Reflects limit of numerical precision.

Table 4.11: Scenario 1 – Linear Controller Fuel Performance Summary

Controller Type	Fuel Consumption	Deviation from Ideal (Perfect Tracking)
Ideal Translation/Attitude	23.25535	–
Linear Translation/Attitude (no delay)	23.63285	+1.6233%
Linear Translation/Attitude	23.63308	+1.6243%

4.5.6   Summary

The results in Sections 4.3 and 4.4 demonstrate the superior performance of the nonlinear control in the absence of unmodeled dynamics. In contrast, the performance characteristics for the linear and nonlinear controllers are mixed in the presence of unmodeled effects due to the presence of an integrator. The linear controller is more robust to the unmodeled dynamics. While less robust, the nonlinear controller performance degrades, but maintains superior tracking performance, except for steady state conditions. Minimum tracking error, occuring at steady state, is lower for the linear controller. The robustness of the linear controller suggests adding an integrator feature to the nonlinear controller would provide the best controller performance. This motivates the discussion of adaptive nonlinear control in the next chapter.

As a closing comment, simulating Scenario 2 with the same perturbations generates similar performance characteristics. The results are omitted for the sake of brevity.

Chapter 5

Adaptive Control System Design

Implementation of control designs developed in Chapter 3 assumes availability of spacecraft mass properties and absolute state data. As an example, although the linear control is computed with relative state measurements, computation of the dynamics matrix requires the absolute state of the Leader. Also, real systems challenge the control designer with the need to compensate for uncertainty in system properties and dynamics, as well as measurement noise. This chapter discusses nonlinear adaptive control strategies to meet these challenges. The goal is to design a 6DOF adaptive control algorithm to compensate for dynamic uncertainty, uncertainty in spacecraft mass properties, and uncertainty in thruster performance.

5.1 Model Uncertainty and Unmodeled Dynamics

This section provides a general overview of expected disturbances associated with spacecraft formation flying due to model uncertainty and dynamic disturbances. Further characterization of uncertainties and disturbances appear in section 5.3 along with specific adaptive control designs.

5.1.1 Spacecraft Parameter Uncertainty

While spacecraft properties are not completely unknown, uncertainty limits knowledge of the true values. Two principal contributors to control error are mass property uncertainty and thruster performance/alignment uncertainty. Mass properties are measured prior to launch, but are expected to change during the life of a mission. Mass property changes typically link to fuel consumption. Errors in estimated mass properties and thruster performance are not extreme. However, uncertainty impacts the performance of the control strategies developed in Chapter 3, as shown in Section 4.5.4. Adaptive control provides a mechanism to compensate for uncertainty in the spacecraft parameters.

5.1.2 Unmodeled Dynamics

Gravity and solar pressure are the principal drivers for the formation dynamics. The spacecraft dynamics, developed in Chapter 2, neglect the perturbing effect of solar pressure and unmodeled gravitational sources. Since formation control focuses on tracking desired relative states, the principal concern is the differential effects of these perturbations. Ideally, spacecraft design could eliminate, or at least minimize, differential solar pressure.

There are three principal sources of gravitational perturbations. First, while the Earth/Moon system is reasonably modeled as a single mass located at the barycenter, the true field exhibits variation in magnitude and direction matched to the orbital period of the moon. Next, planets contribute to gravitational

perturbations. The net magnitude and direction of the gravity field associated with the other planets varies as their relative orbital positions evolve. The final source is indirect. The gravity model depends on our knowledge of the formation relative to the Sun and Earth/Moon barycenter. Uncertainty in time estimates affect knowledge of the relative positions of the Sun, Earth and Moon. The position of the spacecraft is determined by Earth-based tracking data. Position tracking error is an additional source of uncertainty in the gravity field model.

While mission managers require reasonable knowledge of the absolute state of the formation, the relative states between formation elements principally drive the control system. In addition to compensating for uncertainty in the spacecraft parameters, adaptive control provides a mechanism to compensate for the gravity field model without absolute spacecraft state knowledge.

The scheme for attitude control expects each spacecraft to maintain a desired orientation referenced to inertial space. Relative attitudes are determined by differencing individual spacecraft attitudes. The basic assumption is that each spacecraft will be equipped with sensors for determining its inertial referenced attitude.

5.2   Nonlinear Adaptive Control Theory

Nonlinear adaptive control is one method employed to compensate for modeling errors. Several resources on this topic are references: [28, 34, 58].

5.2.1 Parameter/Model Uncertainty

Adaptive control provides a mechanism to adjust the system model parameters to improve the tracking response. A system lends itself to adaptive control provided the unknown dynamics are structured and can be expressed as a linear parametrization. The dynamics are assumed to have a modified form of Equation 3.12, expressed as:

$$\boldsymbol{H}(\boldsymbol{\xi})\,\dot{\boldsymbol{\nu}} + \boldsymbol{C}(\boldsymbol{\xi},\boldsymbol{\nu})\,\boldsymbol{\nu} + \boldsymbol{E}(\boldsymbol{\xi},\boldsymbol{\nu}) + \boldsymbol{\Gamma}(\boldsymbol{\xi},\boldsymbol{\nu},\boldsymbol{\xi}_r,\boldsymbol{\nu}_r)\,\boldsymbol{\theta} = \boldsymbol{u} \qquad (5.1)$$

$\boldsymbol{\Gamma}(\boldsymbol{\xi},\boldsymbol{\nu},\boldsymbol{\xi}_r,\boldsymbol{\nu}_r)$ is a matrix of known functions. $\boldsymbol{\theta}$ is a vector of uncertain constants.

Assume $\dot{\boldsymbol{\xi}} = \boldsymbol{\nu}$, and express the dynamics as:

$$\boldsymbol{H}(\boldsymbol{\xi})\,\ddot{\boldsymbol{\xi}} + \boldsymbol{C}(\boldsymbol{\xi},\dot{\boldsymbol{\xi}})\,\dot{\boldsymbol{\xi}} + \boldsymbol{E}(\boldsymbol{\xi},\dot{\boldsymbol{\xi}}) + \boldsymbol{\Gamma}(\boldsymbol{\xi},\dot{\boldsymbol{\xi}},\boldsymbol{\xi}_r,\dot{\boldsymbol{\xi}}_r)\,\boldsymbol{\theta} = \boldsymbol{u} \qquad (5.2)$$

In this case the control law, Equation 5.3, and adaptive rule, Equation 5.4, are proposed:

$$\boldsymbol{u} = \boldsymbol{H}(\boldsymbol{\xi})\,\ddot{\boldsymbol{\xi}}_r + \boldsymbol{C}(\boldsymbol{\xi},\dot{\boldsymbol{\xi}})\,\dot{\boldsymbol{\xi}}_r + \boldsymbol{E}(\boldsymbol{\xi},\dot{\boldsymbol{\xi}}) - \boldsymbol{K}_D \boldsymbol{s} + \boldsymbol{\Gamma}(\boldsymbol{\xi},\dot{\boldsymbol{\xi}},\boldsymbol{\xi}_r,\dot{\boldsymbol{\xi}}_r)\,\hat{\boldsymbol{\theta}} \qquad (5.3)$$

Where the design parameter $\boldsymbol{K}_D$ is specified with: $\boldsymbol{K}_D = \boldsymbol{K}_D{}^\mathsf{T} > \boldsymbol{0}$.

$$\dot{\tilde{\boldsymbol{\theta}}} = \dot{\hat{\boldsymbol{\theta}}} = -\,\boldsymbol{\Upsilon}\,\boldsymbol{\Gamma}(\boldsymbol{\xi},\dot{\boldsymbol{\xi}},\boldsymbol{\xi}_r,\dot{\boldsymbol{\xi}}_r)^\mathsf{T}\,\boldsymbol{s} \qquad (5.4)$$

The adaptive gain matrix, $\boldsymbol{\Upsilon}$, is specified with: $\boldsymbol{\Upsilon} = \boldsymbol{\Upsilon}^\mathsf{T} > 0$

Note: $\tilde{\boldsymbol{\theta}} = \hat{\boldsymbol{\theta}} - \boldsymbol{\theta}$, $\boldsymbol{\theta}$ constant $\Rightarrow$ $\dot{\tilde{\boldsymbol{\theta}}} = \dot{\hat{\boldsymbol{\theta}}}$

Equate the control law and dynamics:

$$\boldsymbol{u} = \boldsymbol{H}(\boldsymbol{\xi})\,\ddot{\boldsymbol{\xi}}_r + \boldsymbol{C}(\boldsymbol{\xi},\dot{\boldsymbol{\xi}})\,\dot{\boldsymbol{\xi}}_r + \boldsymbol{E}(\boldsymbol{\xi},\dot{\boldsymbol{\xi}}) + \boldsymbol{\Gamma}(\boldsymbol{\xi},\dot{\boldsymbol{\xi}},\boldsymbol{\xi}_r,\dot{\boldsymbol{\xi}}_r)\hat{\boldsymbol{\theta}} - \boldsymbol{K}_D \boldsymbol{s}$$

$$\boldsymbol{u} = \boldsymbol{H}(\boldsymbol{\xi})\,\ddot{\boldsymbol{\xi}} + \boldsymbol{C}(\boldsymbol{\xi},\dot{\boldsymbol{\xi}})\,\dot{\boldsymbol{\xi}} + \boldsymbol{E}(\boldsymbol{\xi},\dot{\boldsymbol{\xi}}) + \boldsymbol{\Gamma}(\boldsymbol{\xi},\dot{\boldsymbol{\xi}},\boldsymbol{\xi}_r,\dot{\boldsymbol{\xi}}_r)\boldsymbol{\theta}$$

$$\Rightarrow \quad \boldsymbol{H}(\boldsymbol{\xi})\,[\ddot{\boldsymbol{\xi}} - \ddot{\boldsymbol{\xi}}_r] + \boldsymbol{C}(\boldsymbol{\xi},\dot{\boldsymbol{\xi}})\,[\dot{\boldsymbol{\xi}} - \dot{\boldsymbol{\xi}}_r] - \boldsymbol{\Gamma}(\boldsymbol{\xi},\dot{\boldsymbol{\xi}},\boldsymbol{\xi}_r,\dot{\boldsymbol{\xi}}_r)\,[\hat{\boldsymbol{\theta}} - \boldsymbol{\theta}] + \boldsymbol{K}_D\,\boldsymbol{s} = 0$$

$$\Rightarrow \quad \boldsymbol{H}(\boldsymbol{\xi})\,\dot{\boldsymbol{s}} + \boldsymbol{C}(\boldsymbol{\xi},\dot{\boldsymbol{\xi}})\,\boldsymbol{s} - \boldsymbol{\Gamma}(\boldsymbol{\xi},\dot{\boldsymbol{\xi}},\boldsymbol{\xi}_r,\dot{\boldsymbol{\xi}}_r)\,\tilde{\boldsymbol{\theta}} + \boldsymbol{K}_D\,\boldsymbol{s} = 0$$

$$\Rightarrow \quad \boldsymbol{H}(\boldsymbol{\xi})\,\dot{\boldsymbol{s}} = -[\boldsymbol{C}(\boldsymbol{\xi},\dot{\boldsymbol{\xi}}) + \boldsymbol{K}_D]\,\boldsymbol{s} + \boldsymbol{\Gamma}(\boldsymbol{\xi},\dot{\boldsymbol{\xi}},\boldsymbol{\xi}_r,\dot{\boldsymbol{\xi}}_r)\,\tilde{\boldsymbol{\theta}} \qquad (5.5)$$

For the stability proof choose the candidate Lyapunov function:

$$V(\boldsymbol{s},t) = \frac{1}{2}\boldsymbol{s}^{\mathsf{T}}\boldsymbol{H}(\boldsymbol{\xi})\boldsymbol{s} + \frac{1}{2}\tilde{\boldsymbol{\theta}}^{\mathsf{T}}\boldsymbol{\Upsilon}^{-1}\tilde{\boldsymbol{\theta}} \qquad (5.6)$$

$$\Rightarrow \quad \dot{V}(\boldsymbol{s},t) = \boldsymbol{s}^{\mathsf{T}}\boldsymbol{H}(\boldsymbol{\xi})\dot{\boldsymbol{s}} + \tfrac{1}{2}\boldsymbol{s}^{\mathsf{T}}\dot{\boldsymbol{H}}(\boldsymbol{\xi})\boldsymbol{s} + \tilde{\boldsymbol{\theta}}^{\mathsf{T}}\boldsymbol{\Upsilon}^{-1}\dot{\tilde{\boldsymbol{\theta}}}$$

Substitute Equation 5.5: $\boldsymbol{H}(\boldsymbol{\xi})\,\dot{\boldsymbol{s}} = -[\boldsymbol{C}(\boldsymbol{\xi},\dot{\boldsymbol{\xi}}) + \boldsymbol{K}_D]\,\boldsymbol{s} + \boldsymbol{\Gamma}(\boldsymbol{\xi},\boldsymbol{\nu},\boldsymbol{\xi}_r,\boldsymbol{\nu}_r)\,\tilde{\boldsymbol{\theta}}$,

and the adaptive rule: $\dot{\hat{\boldsymbol{\theta}}} = -\,\boldsymbol{\Upsilon}\,\boldsymbol{\Gamma}(\boldsymbol{\xi},\dot{\boldsymbol{\xi}},\boldsymbol{\xi}_r,\dot{\boldsymbol{\xi}}_r)^{\mathsf{T}}\,\boldsymbol{s}$

$$\Rightarrow \quad \dot{V}(\boldsymbol{s},t) = -\boldsymbol{s}^{\mathsf{T}}[\boldsymbol{C}(\boldsymbol{\xi},\dot{\boldsymbol{\xi}}) + \boldsymbol{K}_D]\,\boldsymbol{s} + \tfrac{1}{2}\boldsymbol{s}^{\mathsf{T}}\dot{\boldsymbol{H}}(\boldsymbol{\xi})\boldsymbol{s} + \boldsymbol{s}^{\mathsf{T}}\,\boldsymbol{\Gamma}(\boldsymbol{\xi},\dot{\boldsymbol{\xi}},\boldsymbol{\xi}_r,\dot{\boldsymbol{\xi}}_r)\,\tilde{\boldsymbol{\theta}}$$

$$-\,\tilde{\boldsymbol{\theta}}^{\mathsf{T}}\,\boldsymbol{\Gamma}(\boldsymbol{\xi},\boldsymbol{\nu},\boldsymbol{\xi}_r,\boldsymbol{\nu}_r)^{\mathsf{T}}\,\boldsymbol{s}$$

$$\Rightarrow \quad \dot{V}(\boldsymbol{s},t) = -\boldsymbol{s}^{\mathsf{T}}\boldsymbol{K}_D\,\boldsymbol{s} + \tfrac{1}{2}\boldsymbol{s}^{\mathsf{T}}[\dot{\boldsymbol{H}}(\boldsymbol{\xi}) - 2\,\boldsymbol{C}(\boldsymbol{\xi},\dot{\boldsymbol{\xi}})]\boldsymbol{s}$$

$[\dot{\boldsymbol{H}}(\boldsymbol{\xi}) - 2\,\boldsymbol{C}(\boldsymbol{\xi},\dot{\boldsymbol{\xi}})]$ is skew $\Rightarrow \quad \tfrac{1}{2}\boldsymbol{s}^{\mathsf{T}}[\dot{\boldsymbol{H}}(\boldsymbol{\xi}) - 2\,\boldsymbol{C}(\boldsymbol{\xi},\dot{\boldsymbol{\xi}})]\boldsymbol{s} = 0$

$$\Rightarrow \quad \dot{V}(\boldsymbol{s},t) = -\boldsymbol{s}^{\mathsf{T}}\boldsymbol{K}_D\,\boldsymbol{s} < 0 \ \forall \ \boldsymbol{s} \neq \boldsymbol{0} \ \Rightarrow \boldsymbol{s} \to \boldsymbol{0} \qquad (5.7)$$

The remainder of the proof of asymptotic stability of $\tilde{\boldsymbol{\xi}}$ follows the same line of reasoning presented in the section 3.1.2. This method does not guarantee identification of the unknown parameter, $\boldsymbol{\theta}$.

5.2.2 Actuation Uncertainty

The above algorithm adaptively determines the desired control. However, implementation requires mapping the desired control to a set of actuator commands. As discussed in Sections 2.3 and 3.4, actuator commands are determined by a reverse mapping, given by:

$$\boldsymbol{F}_{thrust} = \boldsymbol{B}_{thrust}{}^{\mathsf{T}}(\boldsymbol{B}_{thrust}\,\boldsymbol{B}_{thrust}{}^{\mathsf{T}})^{-1}\,\boldsymbol{u} \tag{5.8}$$

The approach assumes knowledge of the $\boldsymbol{B}_{thrust}$ matrix, which reflects the placement, orientation and output of the individual thrusters. As with other parameters, $\boldsymbol{B}_{thrust}$ represents an estimate of the true value. Adaptive methods can be applied to compensate for the uncertainty. The control law is implemented as discussed in Section 5.2.1 with the addition of an adaptive rule for modifying $\boldsymbol{B}_{thrust}$. With $\boldsymbol{u}$ computed from Equation 5.3, the thrust command is:

$$\boldsymbol{F}_{thrust} = \hat{\boldsymbol{B}}_{thrust}{}^{\mathsf{T}}(\hat{\boldsymbol{B}}_{thrust}\,\hat{\boldsymbol{B}}_{thrust}{}^{\mathsf{T}})^{-1}\,\boldsymbol{u} \tag{5.9}$$

Compute $\boldsymbol{B}_{thrust}\boldsymbol{F}_{thrust}$ as:

$$\begin{aligned}
\boldsymbol{B}_{thrust}\boldsymbol{F}_{thrust} &= (\hat{\boldsymbol{B}}_{thrust} - \tilde{\boldsymbol{B}}_{thrust})\boldsymbol{F}_{thrust} = \hat{\boldsymbol{B}}_{thrust}\boldsymbol{F}_{thrust} - \tilde{\boldsymbol{B}}_{thrust}\boldsymbol{F}_{thrust} \\
&= \hat{\boldsymbol{B}}_{thrust}[\hat{\boldsymbol{B}}_{thrust}{}^{\mathsf{T}}(\hat{\boldsymbol{B}}_{thrust}\,\hat{\boldsymbol{B}}_{thrust}{}^{\mathsf{T}})^{-1}\,\boldsymbol{u}] - \tilde{\boldsymbol{B}}_{thrust}\boldsymbol{F}_{thrust} \\
&= \boldsymbol{u} - \tilde{\boldsymbol{B}}_{thrust}\boldsymbol{F}_{thrust}
\end{aligned}$$

The dynamics are:

$$\boldsymbol{B}_{thrust}\boldsymbol{F}_{thrust} = \boldsymbol{H}(\boldsymbol{\xi})\,\ddot{\boldsymbol{\xi}} + \boldsymbol{C}(\boldsymbol{\xi},\dot{\boldsymbol{\xi}})\,\dot{\boldsymbol{\xi}} + \boldsymbol{E}(\boldsymbol{\xi},\dot{\boldsymbol{\xi}}) + \boldsymbol{\Gamma}(\boldsymbol{\xi},\dot{\boldsymbol{\xi}},\boldsymbol{\xi}_r,\dot{\boldsymbol{\xi}}_r)\boldsymbol{\theta}$$

The control is:

$$\boldsymbol{u} = \boldsymbol{H}(\boldsymbol{\xi})\,\ddot{\boldsymbol{\xi}}_r + \boldsymbol{C}(\boldsymbol{\xi},\dot{\boldsymbol{\xi}})\,\dot{\boldsymbol{\xi}}_r + \boldsymbol{E}(\boldsymbol{\xi},\dot{\boldsymbol{\xi}}) + \boldsymbol{\Gamma}(\boldsymbol{\xi},\dot{\boldsymbol{\xi}},\boldsymbol{\xi}_r,\dot{\boldsymbol{\xi}}_r)\hat{\boldsymbol{\theta}} - \boldsymbol{K}_D\boldsymbol{s}$$

Then the closed loop dynamics are formed as:

$$\boldsymbol{u} = \boldsymbol{H}(\boldsymbol{\xi})\,\ddot{\boldsymbol{\xi}}_r + \boldsymbol{C}(\boldsymbol{\xi},\dot{\boldsymbol{\xi}})\,\dot{\boldsymbol{\xi}}_r + \boldsymbol{E}(\boldsymbol{\xi},\dot{\boldsymbol{\xi}}) + \boldsymbol{\Gamma}(\boldsymbol{\xi},\dot{\boldsymbol{\xi}},\boldsymbol{\xi}_r,\dot{\boldsymbol{\xi}}_r)\hat{\boldsymbol{\theta}} - \boldsymbol{K}_D \boldsymbol{s}$$

$$= \left\{ \boldsymbol{H}(\boldsymbol{\xi})\,\ddot{\boldsymbol{\xi}} + \boldsymbol{C}(\boldsymbol{\xi},\dot{\boldsymbol{\xi}})\,\dot{\boldsymbol{\xi}} + \boldsymbol{E}(\boldsymbol{\xi},\dot{\boldsymbol{\xi}}) + \boldsymbol{\Gamma}(\boldsymbol{\xi},\dot{\boldsymbol{\xi}},\boldsymbol{\xi}_r,\dot{\boldsymbol{\xi}}_r)\boldsymbol{\theta} \right\} + \tilde{\boldsymbol{B}}_{thrust}\boldsymbol{F}_{thrust}$$

$$\Rightarrow \quad \boldsymbol{H}(\boldsymbol{\xi})\,\dot{\boldsymbol{s}} + \boldsymbol{C}(\boldsymbol{\xi},\dot{\boldsymbol{\xi}})\,\boldsymbol{s} - \boldsymbol{\Gamma}(\boldsymbol{\xi},\dot{\boldsymbol{\xi}},\boldsymbol{\xi}_r,\dot{\boldsymbol{\xi}}_r)\,\tilde{\boldsymbol{\theta}} + \boldsymbol{K}_D \boldsymbol{s} + \tilde{\boldsymbol{B}}_{thrust}\boldsymbol{F}_{thrust} = \boldsymbol{0}$$

For the stability proof modify the candidate Lyapunov function from Equation 5.6:

$$V(\boldsymbol{s},t) = \frac{1}{2}\boldsymbol{s}^\mathsf{T}\boldsymbol{H}(\boldsymbol{\xi})\boldsymbol{s} + \frac{1}{2}\tilde{\boldsymbol{\theta}}^\mathsf{T}\boldsymbol{\Upsilon}^{-1}\tilde{\boldsymbol{\theta}} + \frac{1}{2\kappa}[\tilde{\boldsymbol{B}}_{thrust}]_{ij}[\tilde{\boldsymbol{B}}_{thrust}]_{ij} \qquad (5.10)$$

The term $[\tilde{\boldsymbol{B}}_{thrust}]_{ij}$ represents the individual elements of $\tilde{\boldsymbol{B}}_{thrust}$. The repeated indices in Equation 5.10 imply summation over all values of i and j. The derivative of the Lyapunov function is:

$$\dot{V}(\boldsymbol{s},t) = \boldsymbol{s}^\mathsf{T}\boldsymbol{H}(\boldsymbol{\xi})\dot{\boldsymbol{s}} + \tfrac{1}{2}\boldsymbol{s}^\mathsf{T}\dot{\boldsymbol{H}}(\boldsymbol{\xi})\boldsymbol{s} + \tilde{\boldsymbol{\theta}}^\mathsf{T}\boldsymbol{\Upsilon}^{-1}\dot{\tilde{\boldsymbol{\theta}}} + \tfrac{1}{\kappa}[\tilde{\boldsymbol{B}}_{thrust}]_{ij}[\dot{\tilde{\boldsymbol{B}}}_{thrust}]_{ij}$$

Substitute $\boldsymbol{H}(\boldsymbol{\xi})\,\dot{\boldsymbol{s}} = -[\boldsymbol{C}(\boldsymbol{\xi},\dot{\boldsymbol{\xi}}) + \boldsymbol{K}_D]\,\boldsymbol{s} + \boldsymbol{\Gamma}(\boldsymbol{\xi},\boldsymbol{\nu},\boldsymbol{\xi}_r,\boldsymbol{\nu}_r)\,\tilde{\boldsymbol{\theta}} - \tilde{\boldsymbol{B}}_{thrust}\boldsymbol{F}_{thrust}$, and the adaptive rule: $\dot{\hat{\boldsymbol{\theta}}} = -\boldsymbol{\Upsilon}\,\boldsymbol{\Gamma}(\boldsymbol{\xi},\dot{\boldsymbol{\xi}},\boldsymbol{\xi}_r,\dot{\boldsymbol{\xi}}_r)^\mathsf{T}\,\boldsymbol{s}$. Also, define and substitute $\dot{\hat{\boldsymbol{B}}}_{thrust} = \dot{\tilde{\boldsymbol{B}}}_{thrust} = \kappa\,\boldsymbol{s}\,[\boldsymbol{F}_{thrust}]^\mathsf{T} \Rightarrow [\dot{\tilde{\boldsymbol{B}}}_{thrust}]_{ij} = s_i[\boldsymbol{F}_{thrust}]_j$

$$\Rightarrow \quad \dot{V}(\boldsymbol{s},t) = -\boldsymbol{s}^\mathsf{T}[\boldsymbol{C}(\boldsymbol{\xi},\dot{\boldsymbol{\xi}}) + \boldsymbol{K}_D]\,\boldsymbol{s} + \tfrac{1}{2}\boldsymbol{s}^\mathsf{T}\dot{\boldsymbol{H}}(\boldsymbol{\xi})\boldsymbol{s} + \boldsymbol{s}^\mathsf{T}\boldsymbol{\Gamma}(\boldsymbol{\xi},\dot{\boldsymbol{\xi}},\boldsymbol{\xi}_r,\dot{\boldsymbol{\xi}}_r)\,\tilde{\boldsymbol{\theta}}$$

$$-\boldsymbol{s}^\mathsf{T}\tilde{\boldsymbol{B}}_{thrust}\boldsymbol{F}_{thrust} - \tilde{\boldsymbol{\theta}}^\mathsf{T}\,\boldsymbol{\Gamma}(\boldsymbol{\xi},\boldsymbol{\nu},\boldsymbol{\xi}_r,\boldsymbol{\nu}_r)^\mathsf{T}\,\boldsymbol{s} + s_i[\tilde{\boldsymbol{B}}_{thrust}]_{ij}[\boldsymbol{F}_{thrust}]_j$$

Note:

$$\boldsymbol{s}^\mathsf{T}\boldsymbol{\Gamma}(\boldsymbol{\xi},\dot{\boldsymbol{\xi}},\boldsymbol{\xi}_r,\dot{\boldsymbol{\xi}}_r)\tilde{\boldsymbol{\theta}} = \tilde{\boldsymbol{\theta}}^\mathsf{T}\boldsymbol{\Gamma}(\boldsymbol{\xi},\boldsymbol{\nu},\boldsymbol{\xi}_r,\boldsymbol{\nu}_r)^\mathsf{T}\boldsymbol{s}$$

$$\boldsymbol{s}^\mathsf{T}\tilde{\boldsymbol{B}}_{thrust}\boldsymbol{F}_{thrust} = s_i[\tilde{\boldsymbol{B}}_{thrust}]_{ij}[\boldsymbol{F}_{thrust}]_j$$

$$[\dot{\boldsymbol{H}}(\boldsymbol{\xi}) - 2\,\boldsymbol{C}(\boldsymbol{\xi},\dot{\boldsymbol{\xi}})] \text{ is skew} \Rightarrow \tfrac{1}{2}\boldsymbol{s}^\mathsf{T}[\dot{\boldsymbol{H}}(\boldsymbol{\xi}) - 2\,\boldsymbol{C}(\boldsymbol{\xi},\dot{\boldsymbol{\xi}})]\boldsymbol{s} = 0$$

Therefore: $\dot{V}(\boldsymbol{s},t) = -\boldsymbol{s}^\mathsf{T}\boldsymbol{K}_D\boldsymbol{s} < 0 \;\forall\; \boldsymbol{s} \neq \boldsymbol{0} \;\Rightarrow \boldsymbol{s} \to \boldsymbol{0}$

128

The remainder of the proof for asymptotic stability of $\tilde{\boldsymbol{\xi}}$ follows the same line of reasoning presented in the section 3.1.2. This method simultaneously estimates $\boldsymbol{B}_{thrust}$ and $\boldsymbol{\theta}$. As before, while the tracking error is asymptotically stable, identification of $\boldsymbol{B}_{thrust}$ and $\boldsymbol{\theta}$ is not guaranteed.

5.3 Parametrization for Nonlinear Adaptive Formation Control

5.3.1 Linear Parametrization for Translation Control

The development of a linear parametric dynamic model is based on the relative orbital dynamics, recall Equation 2.26. Assuming the Leader follows a ballistic trajectory, $\boldsymbol{u}_{thrust,L} = 0$, the dynamics are expressed as:

$$
\begin{aligned}
\boldsymbol{u}_{thrust,F} \quad &= \ddot{\boldsymbol{x}} + \left\{ \frac{\mu_{em}}{\|\boldsymbol{r}_{EF}\|^3} + \frac{\mu_s}{\|\boldsymbol{r}_{SF}\|^3} \right\} \boldsymbol{x} + \mu_{em} \left\{ \frac{1}{\|\boldsymbol{r}_{EF}\|^3} - \frac{1}{\|\boldsymbol{r}_{EL}\|^3} \right\} \boldsymbol{r}_{EL} \\
&\quad + \mu_s \left\{ \frac{1}{\|\boldsymbol{r}_{SF}\|^3} - \frac{1}{\|\boldsymbol{r}_{SL}\|^3} \right\} \boldsymbol{r}_{SL} + \boldsymbol{\Delta f}_{solar} + \boldsymbol{\Delta f}_{pert}
\end{aligned}
\tag{5.11}
$$

The goal is to parameterize dynamic uncertainty in the form $\boldsymbol{\Gamma}_{T}\boldsymbol{\theta}_{T}$. $\boldsymbol{\Gamma}_{T}$ is known, $\boldsymbol{\theta}_{T}$ is a constant with uncertain elements. The gravitational parameters represent the only true constants in Equation 5.11. However, for the typical formation flying mission profile, range vectors linking each spacecraft to the Earth and Sun evolve at a slow rate compared to the control cycle. While the range vector direction sweeps inertial space, the magnitude exhibits much less variation. Therefore, an adaptive mechanism will track the dynamics associated

129

with the variation in the range vector magnitude as if it were constant. The range vector direction is measured. Recall, the adaptive mechanism does not guarantee identification of $\boldsymbol{\theta}_T$.

The spacecraft are considered equipped with a suite of sensors capable of resolving the relative range, $\boldsymbol{x}$, in inertial coordinates. Also, sensors measure the inertial direction to the Earth and Sun. While the dynamics model references the position of the Earth/Moon barycenter, the position of the Earth provides a reasonable measure of the barycenter position. The barycenter lies below the surface of the Earth. Equation 5.11 is restructured as the measured vectors with constant coefficients.

$$\boldsymbol{u}_{thrust,F} = \ddot{\boldsymbol{x}} + d_1\,\boldsymbol{x} + d_2\,\boldsymbol{e}_{EL} + d_3\,\boldsymbol{e}_{SL} + \boldsymbol{\Delta f}_{solar} + \boldsymbol{\Delta f}_{pert} \tag{5.12}$$

Where:

$d_1 = \{\frac{\mu_{em}}{||\boldsymbol{r}_{EF}||^3} + \frac{\mu_s}{||\boldsymbol{r}_{SF}||^3}\}$

$d_2 = \mu_{em}\{\frac{1}{||\boldsymbol{r}_{EF}||^3} - \frac{1}{||\boldsymbol{r}_{EL}||^3}\}||\boldsymbol{r}_{EL}||$

$d_3 = \mu_s\{\frac{1}{||\boldsymbol{r}_{SF}||^3} - \frac{1}{||\boldsymbol{r}_{SL}||^3}\}||\boldsymbol{r}_{SL}||$

$\boldsymbol{e}_{EL} = \frac{\boldsymbol{r}_{EL}}{||\boldsymbol{r}_{EL}||}$, Unit vector pointing from Earth toward Leader (measured)

$\boldsymbol{e}_{SL} = \frac{\boldsymbol{r}_{SL}}{||\boldsymbol{r}_{SL}||}$, Unit vector pointing from Sun toward Leader (measured)

Expressing the gravity and solar pressure perturbation terms as a linear parametrization requires engineering judgement. The force generated by solar pressure is proportional to its coefficient of reflectivity and the {cross-sectional area

130

of incidence/mass} ratio. Balancing the acceleration due to solar pressure serves to minimize fuel requirements for formation maintenance. Assume the spacecraft configurations are designed to minimize differential solar pressure, $||\boldsymbol{\Delta f}_{solar}||$ is considered constant, possibly with a trackable, slow variation. Also, with the sun as the dominant radiation source, $\boldsymbol{\Delta f}_{solar}$ will maintain alignment with the Sun-to-spacecraft vector. Therefore, differential solar pressure is modeled as: $\boldsymbol{\Delta f}_{solar} = d_4 \boldsymbol{e}_{SL} \approx d_4 \boldsymbol{e}_{SF}$. Note: $\boldsymbol{e}_{SF} \approx \boldsymbol{e}_{SL}$ since the spacecraft range to the sun 1.5×10^8 kilometers, is much larger than the relative spacecraft ranges within a formation.
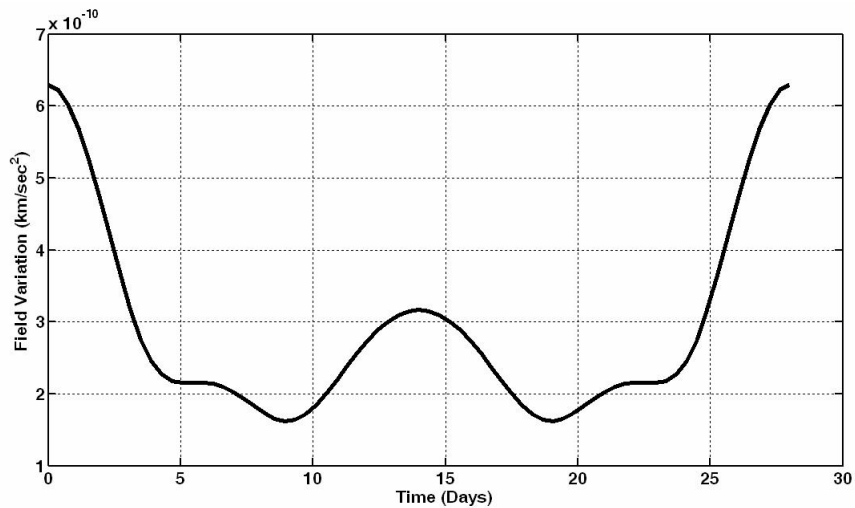
Figure 5.1: Variation in True Earth Moon Gravity Field Experienced at L_2

Perturbations in the gravity field are small, but deserve consideration. The most significant variation is associated with the treatment of the Earth/Moon system as a single point mass, versus two distinct masses. As noted in Figure 5.1, the

difference between the true field and the modeled field at L_2 is on the order of 10^{-10} kilometers/sec^2. In contrast, the gravity field due to the Earth/Moon is approximately 2×10^{-7} kilometers/sec^2, and the gravity field due to the Sun is approximately 6×10^{-6} kilometers/sec^2. These values represent the total gravity field experienced by the spacecraft, rather than the differential field across the formation, yet reflect the relative magnitude of the contribution of each source. Additional perturbations are generated by the gravity field of the other planets. At the point of closest approach, the gravity fields of Venus and Jupiter have the same order of magnitude as the variation in the Earth/Moon field. The gravity field perturbation is modeled as: $\boldsymbol{\Delta f}_{pert} = d_5 \boldsymbol{e}_{EL} \approx d_5 \boldsymbol{e}_{EF}$, recognizing $\boldsymbol{e}_{EF} \approx \boldsymbol{e}_{EL}$. The model structure recognizes the variation in the Earth/Moon field generally aligns with the direction to the Earth. Also, the field variations due to Venus and Jupiter are much slower than the 28 day cycle of the Earth/Moon field variation. Therefore, an adaptive mechanism that tracks the Earth/Moon field variations will be able to approximately track the variations due to Jupiter, Venus and the other planets.

Equation 5.12 is rewritten to reflect the linear parametrization of the perturbations, as discussed.

$$
\begin{aligned}
\boldsymbol{u}_{thrust,F} &= \ddot{\boldsymbol{x}} + d_1 \, \boldsymbol{x} + d_2 \, \boldsymbol{e}_{EL} + d_3 \, \boldsymbol{e}_{SL} + d_4 \boldsymbol{e}_{SL} + d_5 \boldsymbol{e}_{EL} \\
&= \ddot{\boldsymbol{x}} + d_1 \, \boldsymbol{x} + (d_2 + d_5) \, \boldsymbol{e}_{EL} + (d_3 + d_4) \, \boldsymbol{e}_{SL}
\end{aligned}
\tag{5.13}
$$

Expressed in matrix form:

$$
\boldsymbol{u}_{thrust,F} = \ddot{\boldsymbol{x}} + [\boldsymbol{x}|\boldsymbol{e}_{EL}|\boldsymbol{e}_{SL}]
\begin{bmatrix}
d_1 \\
(d_2 + d_4) \\
(d_3 + d_5)
\end{bmatrix}
= \boldsymbol{\Gamma}_T \, \boldsymbol{\theta}_T
\tag{5.14}
$$

As discussed, $\boldsymbol{e}_{EF} \approx \boldsymbol{e}_{EL}$ and $\boldsymbol{e}_{SF} \approx \boldsymbol{e}_{SL}$, allowing an equivalent implementation with $\boldsymbol{\Gamma}_T = [\boldsymbol{x}|\boldsymbol{e}_{EF}|\boldsymbol{e}_{SF}]$. The reference spacecraft selection in the controller is driven by the metrology architecture.

Based on Equation 5.3, the control law is expressed as:

$$\boldsymbol{u}_{thrust,F} = \ddot{\boldsymbol{x}}_r + \boldsymbol{\Gamma}_T\, \hat{\boldsymbol{\theta}}_T - \boldsymbol{K}_D \boldsymbol{s}, \text{ With: } \dot{\hat{\boldsymbol{\theta}}}_T = -\, \boldsymbol{\Upsilon}_T \, \boldsymbol{\Gamma}_T{}^{\mathsf{T}}\, \boldsymbol{s} \qquad (5.15)$$

Knowledge of the spacecraft mass is necessary to determine thrust required to generate the desired control, $\boldsymbol{u}_{thrust,F}$. Mass properties can be incorporated in the control law provided in Equation 5.15. Alternatively, the mass properties can be included in the actuator mapping matrix, $\boldsymbol{B}_{thrust}$. As discussed in section 5.2.2, compensation for actuator mapping uncertainty is achieved through a separate adaptive rule. The specific formation flying discussion on this topic is provided in section 5.3.3, addressing both translation and attitude control.

Including estimated mass properties in Equation 5.15, the modified control law is:

$$[\hat{m}_F \boldsymbol{u}_{thrust,F}] \;= \hat{m}_F \ddot{\boldsymbol{x}}_r + \hat{m}_F \boldsymbol{\Gamma}_T\, \hat{\boldsymbol{\theta}}_T - \hat{m}_F \boldsymbol{K}_D \boldsymbol{s}$$

$$= \boldsymbol{m}_F \ddot{\boldsymbol{x}}_r + [\ddot{\boldsymbol{x}}_r|\boldsymbol{x}|\boldsymbol{e}_{EL}|\boldsymbol{e}_{SL}] \begin{bmatrix} (\hat{m}_F - \boldsymbol{m}_F) \\ d_1 \\ (d_2 + d_4) \\ (d_3 + d_5) \end{bmatrix} - \hat{m}_F \boldsymbol{K}_D \boldsymbol{s} \qquad (5.16)$$

Implemented as:

$$[\hat{m}_F u_{thrust,F}] = [\ddot{\boldsymbol{x}}_r|\boldsymbol{x}|\boldsymbol{e}_{EL}|\boldsymbol{e}_{SL}] \begin{bmatrix} \hat{m}_F \\ d_1 \\ (d_2 + d_4) \\ (d_3 + d_5) \end{bmatrix} - \hat{m}_F \boldsymbol{K}_D \boldsymbol{s} \tag{5.17}$$

$$= \boldsymbol{\Gamma}_{T,m} \, \hat{\boldsymbol{\theta}}_{T,m} - \hat{m}_F \boldsymbol{K}_D \boldsymbol{s}, \text{ With: } \dot{\hat{\boldsymbol{\theta}}}_{T,m} = -\boldsymbol{\Upsilon}_T [\boldsymbol{\Gamma}_{T,m}]^\mathsf{T} \boldsymbol{s}$$

The dynamics model, Equation 5.14, is modified to include the true spacecraft mass. Equating the dynamics with the control, Equation 5.17, provides the closed loop dynamics. Asymptotic stability of the error dynamics follows from the analysis presented in Section 5.2.1.

5.3.2 Linear Parametrization for Attitude Control

Reference [14] presents an adaptive control design for the case where the inertia matrix, $\boldsymbol{H}_R$, is unknown. The method requires an expression of $\boldsymbol{H}_R \dot{\boldsymbol{\omega}}_r - [\boldsymbol{H}_R \, \boldsymbol{\omega}\times]\boldsymbol{\omega}_r$ as a linear parameterization of the form:

$$\boldsymbol{H}_R \dot{\boldsymbol{\omega}}_r - [\boldsymbol{H}_R \, \boldsymbol{\omega}\times]\boldsymbol{\omega}_r = \boldsymbol{\Gamma}_R(\omega, \omega_r, \dot{\omega}_r) \, \boldsymbol{\theta}_R(\boldsymbol{H}_R) \tag{5.18}$$

The term $\boldsymbol{\theta}_R(\boldsymbol{H}_R)$ is a constant vector formed from the unknown components of $\boldsymbol{H}_R$. The control law and adaptive rule that guarantee global stability are expressed as:

$$\text{Control Law: } \boldsymbol{\tau} = \boldsymbol{\Gamma}_R(\omega, \omega_r, \dot{\omega}_r) \, \hat{\boldsymbol{\theta}}_R - \boldsymbol{K}_R \, \boldsymbol{s}_R \tag{5.19}$$

$$\text{Adaptive Rule: } \dot{\hat{\boldsymbol{\theta}}}_R = -\boldsymbol{\Upsilon}_R \, \boldsymbol{\Gamma}_R(\omega, \omega_r, \dot{\omega}_r)^\mathsf{T} \, \boldsymbol{s}_R \tag{5.20}$$

Where:

$\boldsymbol{\Upsilon}_R$ – Design parameter, $\boldsymbol{\Upsilon}_R = \boldsymbol{\Upsilon}_R^\mathsf{T} > 0$

The parameterization for Equation 5.18 is not unique. The specific definition of $\mathbf{\Gamma}_R(\boldsymbol{\omega}, \boldsymbol{\omega}_r, \dot{\boldsymbol{\omega}}_r)$ and $\boldsymbol{\theta}_R$ applied in this work follows:

$$\text{For } \boldsymbol{H_R} = \begin{bmatrix} h_{R_{11}} & h_{R_{12}} & h_{R_{13}} \\ h_{R_{12}} & h_{R_{22}} & h_{R_{23}} \\ h_{R_{13}} & h_{R_{23}} & h_{R_{33}} \end{bmatrix}, \text{ define } \boldsymbol{\theta_R} \equiv \begin{bmatrix} h_{R_{11}} \\ h_{R_{22}} \\ h_{R_{33}} \\ h_{R_{12}} \\ h_{R_{13}} \\ h_{R_{23}} \end{bmatrix}, \text{ and}$$

$$\boldsymbol{\Gamma_R}(\boldsymbol{\omega}, \boldsymbol{\omega_r}, \dot{\boldsymbol{\omega}_r}) \equiv \begin{bmatrix} \dot{\omega}_{r_1} & -\omega_2\omega_{r_3}\, \omega_3\omega_{r_2} & \dot{\omega}_{r_2} - \omega_1\omega_{r_3} & \dot{\omega}_{r_3} + \omega_1\omega_{r_2}\, \omega_2\omega_{r_2} - \omega_3\omega_{r_3} \\ \omega_1\omega_{r_3} & \dot{\omega}_{r_2} & -\omega_3\omega_{r_1}\, \dot{\omega}_{r_1} + \omega_2\omega_{r_3}\, \omega_3\omega_{r_3} - \omega_1\omega_{r_1}\, \dot{\omega}_{r_3} - \omega_2\omega_{r_1} \\ -\omega_1\omega_{r_2}\, \omega_2\omega_{r_1} & \dot{\omega}_{r_3} & \omega_1\omega_{r_1} - \omega_2\omega_{r_2}\, \dot{\omega}_{r_1} - \omega_3\omega_{r_2}\, \dot{\omega}_{r_2} + \omega_3\omega_{r_1} \end{bmatrix}$$

Design modification allows compensation for a constant disturbance torque. Adding a disturbance torque to Equation 5.18 gives:

$$\boldsymbol{H_R}\dot{\boldsymbol{\omega}_r} - [\boldsymbol{H_R}\,\boldsymbol{\omega}\times]\boldsymbol{\omega_r} = \boldsymbol{\Gamma_R}(\boldsymbol{\omega}, \boldsymbol{\omega_r}, \dot{\boldsymbol{\omega}_r})\,\boldsymbol{\theta_R}(\boldsymbol{H_R}) + \boldsymbol{\tau}_{dist}$$

Redefine the adaptive parametrization as:

$$\boldsymbol{H_R}\dot{\boldsymbol{\omega}_r} - [\boldsymbol{H_R}\,\boldsymbol{\omega}\times]\boldsymbol{\omega_r} = \boldsymbol{\Gamma}'_R(\boldsymbol{\omega}, \boldsymbol{\omega_r}, \dot{\boldsymbol{\omega}_r})\,\boldsymbol{\theta}'_R(\boldsymbol{H_R}) \tag{5.21}$$

Where:

$$\boldsymbol{\Gamma}'_R(\boldsymbol{\omega}, \boldsymbol{\omega_r}, \dot{\boldsymbol{\omega}_r}) = [\boldsymbol{I_3}|\boldsymbol{\Gamma_R}(\boldsymbol{\omega}, \boldsymbol{\omega_r}, \dot{\boldsymbol{\omega}_r})], \ \boldsymbol{\theta}'_R = [\boldsymbol{\tau}^\mathsf{T}_{dist}|\boldsymbol{\theta_R}^\mathsf{T}]^\mathsf{T} \tag{5.22}$$

5.3.3 Linear Parametrization for Thruster Performance and Misalignment

The control sensitivity matrix, $\boldsymbol{B}_{thrust}$, expresses the mapping of the thruster outputs to the net translational acceleration and torque experienced by the spacecraft. The mathematical structure of $\boldsymbol{B}_{thrust}$ is defined as a set of column vectors representing the translational acceleration and torque generated by each individual thruster. The construction appears as: $\boldsymbol{B}_{thrust} = [b_1|b_2|b_3| \cdots |b_{(n-2)}|b_{(n-1)}|b_n|]$, with n representing the total number of thrusters.

Each b_i is comprised of six elements. By design, the first three elements form a vector in the direction of the thrust vector with a magnitude equal to the reciprocal spacecraft mass. The second set are formed as the cross product of the torque arm and the unit vector in the direction of thrust. The inertial mass properties are not included in $\boldsymbol{B}_{thrust}$, as they appear in the attitude control law.

The sources of error in $\boldsymbol{B}_{thrust}$ link to uncertainty in the spacecraft mass, thruster output, thrust direction, and thruster location (torque arm). Based on the discussion in section 5.2.2, the adaptive rule to compensate for the control sensitivity matrix uncertainty is defined as:

$$\dot{\hat{\boldsymbol{B}}}_{thrust} = \kappa \boldsymbol{s}[\boldsymbol{F}_{thrust}]^{\mathsf{T}} \tag{5.23}$$

As previously noted, the adaptive rule does not guarantee identification of $\boldsymbol{B}_{thrust}$. It neither serves to identify individual components of the uncertainty, such as the spacecraft mass. The design assumes the composition of $\boldsymbol{B}_{thrust}$ is

constant. In reality the mass of the spacecraft decreases at the rate the thrusters expel mass. However, the change is negligible for the thrust levels associated with formation maintenance. For a formation stationed in the vicinity of the Earth/Moon-Sun L_2 point, the thrust levels required to maintain a 100 kilometer separation are on the order of 10^{-7} meters/sec^2. For a spacecraft with a mass of 1,000 kilograms and a thruster $I_{sp} = 1000$ seconds, the mass flow rate is on the order of 10^{-8} kilograms/second. More significant mass changes will result from maneuvers required to stabilize the global trajectory. The interval between these impulsive maneuvers is on the order of weeks. Therefore, the adaptive mechanism is expected to effectively compensate for mass property changes during the intermediate intervals.

5.4 Parametrization for Adaptive Translation without Absolute Navigation

The translation control strategies developed in Chapter 3 require absolute spacecraft states for implementation. Section 5.3.1 presents an adaptive strategy that reduces the requirement for absolute navigation, but still depends on knowledge (measurement) of the range vector directions from the spacecraft to the Sun and Earth. This section provides a modified adaptive algorithm based on relative navigation only. Recall the parameterized dynamics from Equation 5.13:

$$\boldsymbol{u_{thrust,F}} = \ddot{\boldsymbol{x}} + d_1 \, \boldsymbol{x} + (d_2 + d_5) \, \boldsymbol{e_{EL}} + (d_3 + d_4) \, \boldsymbol{e_{SL}}$$

Consider the unit vectors e_{EL} and e_{SL} in the rotating frame of the RTBP. Based on the benchmark problem discussed in sections 1.2.1 and 4.1.5, the formation follows a halo orbit about L_2 with a nominal radius of 300,000 kilometers. The orbit period about L_2 is approximately 6 months. Assuming a perfectly circular trajectory, the velocity of the formation within the rotating frame is approximately 0.1 kilometers/second. The distance between the Earth and L_2 is approximately 1.6×10^6 kilometers. Thus, the unit vector e_{EL} has a negligible rotation rate on the order of 10^{-6} degrees/second. The rotation rate of e_{SL} is two orders of magnitude smaller. Therefore, it is reasonable to treat e_{EL} and e_{SL} as constant vectors within the rotating RTBP frame.

Recall from the discussion of the RTBP in Chapter 2, $\boldsymbol{D}_{RI}(t)$ transforms vectors from the inertial frame to the RTBP frame. Following the definition of the RTBP frame, computation of $\boldsymbol{D}_{RI}(t)$ is based on the position/velocity of the Earth/Moon barycenter relative to the Sun. An accurate measure of time with corresponding planetary ephemeris data is sufficient to determine $\boldsymbol{D}_{RI}(t)$. The parameterized translational dynamics are expressed as:

$$
\begin{aligned}
\boldsymbol{u}_{thrust,F} &= \ddot{\boldsymbol{x}} + d_1\,\boldsymbol{x} + (d_2 + d_5)\,\boldsymbol{D}_{RI}(t)^{\mathsf{T}}\,{}^{R}\boldsymbol{e}_{EL} + (d_3 + d_4)\,\boldsymbol{D}_{RI}(t)^{\mathsf{T}}\,{}^{R}\boldsymbol{e}_{SL} \\
&= \ddot{\boldsymbol{x}} + d_1\,\boldsymbol{x} + \boldsymbol{D}_{RI}(t)^{\mathsf{T}}\,[(d_2 + d_5)\,{}^{R}\boldsymbol{e}_{EL} + (d_3 + d_4)\,{}^{R}\boldsymbol{e}_{SL}] \\
&= \ddot{\boldsymbol{x}} + d_1\,\boldsymbol{x} + \boldsymbol{D}_{RI}(t)^{\mathsf{T}}\,\boldsymbol{\theta}_{T_1}
\end{aligned}
$$

(5.24)

with $\boldsymbol{\theta}_{T_1} \equiv [(d_2 + d_5)\,{}^{R}\boldsymbol{e}_{EL} + (d_3 + d_4)\,{}^{R}\boldsymbol{e}_{SL}]$, constant.

Equation 5.24 parameterizes the uncertain quantities in terms of a constant

vector in the RTBP frame. Considering some unmodeled perturbations may appear as constant disturbances within the inertial frame, an additional term, $\boldsymbol{\theta}_{T_2}$, is added to the parametrization for completeness and increased adaptive flexibility. The linear parametrization of the translation dynamics is expressed as:

$$
\begin{aligned}
\boldsymbol{u}_{thrust,F} &= \ddot{\boldsymbol{x}} + d_1\,\boldsymbol{x} + \boldsymbol{D}_{RI}(t)^\mathsf{T}\,\boldsymbol{\theta}_{T_1} + \boldsymbol{\theta}_{T_2} \\
&= \ddot{\boldsymbol{x}} + [\boldsymbol{x}|\boldsymbol{D}_{RI}(t)^\mathsf{T}|\mathbf{I_3}]\,[d_1|\boldsymbol{\theta}_{T_1}{}^\mathsf{T}|\boldsymbol{\theta}_{T_2}{}^\mathsf{T}]^\mathsf{T} \\
&= \ddot{\boldsymbol{x}} + \boldsymbol{\Gamma}_T\,\boldsymbol{\theta}_T \\
\boldsymbol{\Gamma}_T &\equiv [\boldsymbol{x}|\boldsymbol{D}_{RI}(t)^\mathsf{T}|\mathbf{I_3}] \\
\boldsymbol{\theta}_T &\equiv [d_1|\,\boldsymbol{\theta}_{T_1}{}^\mathsf{T}|\boldsymbol{\theta}_{T_2}{}^\mathsf{T}]^\mathsf{T}
\end{aligned}
\tag{5.25}
$$

With this form of the dynamics the adaptive control law and adaptive rule are expressed as:

$$
\begin{aligned}
\boldsymbol{u}_{thrust,F} &= \ddot{\boldsymbol{x}}_r + \boldsymbol{\Gamma}_T\,\hat{\boldsymbol{\theta}}_T - \boldsymbol{K}_T\,\boldsymbol{s}_T \\
\dot{\hat{\boldsymbol{\theta}}}_T &= \boldsymbol{\Upsilon}_T\boldsymbol{\Gamma}_T{}^\mathsf{T}\,\boldsymbol{s}_T
\end{aligned}
\tag{5.26}
$$

The elegance of this parametrization is the absence of any dependence on global navigation factors. Implementation of the control law only depends on relative navigation data. The rotation matrix, $\boldsymbol{D}_{RI}(t)$, is the coordinate transformation from the inertial to the rotating RTBP frame. Computation of $\boldsymbol{D}_{RI}(t)$ is based on planetary ephemeris data, and therefore easily determined based on knowledge of the ephemeris time.

Further simplification is possible if the alignment of $\boldsymbol{x}$ is known to be constant within either the RTBP or inertial frame. In this case $d_1\,\boldsymbol{x}$ can be absorbed into $\boldsymbol{\theta}_{T_1}$ or $\boldsymbol{\theta}_{T_2}$, respectively. The control is implemented as in Equation 5.26 with $\boldsymbol{\Gamma}_T \equiv [\boldsymbol{D}_{RI}(t)^\mathsf{T}|\mathbf{I_3}]$ and $\boldsymbol{\theta}_T \equiv [\boldsymbol{\theta}_{T_1}{}^\mathsf{T}|\boldsymbol{\theta}_{T_2}{}^\mathsf{T}]^\mathsf{T}$. The strategy is reasonable considering the

science for most formation flying astronomy missions requires maintaining $\boldsymbol{x}$ fixed in inertial space for long observing periods.

5.5   Combined Translation/Attitude Adaptive Control

As discussed in Sections 2.3 and 3.4 the net force and torque generated by the spacecraft thrusters is expressed as:

$$
{}^{\mathrm{b}}\boldsymbol{U} = \begin{bmatrix} {}^{\mathrm{b}}\mathbf{u}_{\mathbf{thrust,F}} \\ \\ \boldsymbol{\tau} \end{bmatrix} = \boldsymbol{B}_{thrust}\,\boldsymbol{F}_{thrust} \tag{5.27}
$$

Based on the parametrization of the translation and attitude dynamics provided in Sections 5.3 and 5.4, the 6DOF dynamics are expressed as:

$$
\begin{aligned}
{}^{\mathrm{b}}\boldsymbol{U} = \boldsymbol{B}_{thrust}\,\boldsymbol{F}_{thrust} &= \begin{bmatrix} \ddot{\boldsymbol{x}} \\ \\ \boldsymbol{0} \end{bmatrix} + \begin{bmatrix} \boldsymbol{\Gamma}_{T} & \boldsymbol{0} \\ \\ \boldsymbol{0} & \boldsymbol{\Gamma}_{R}(\boldsymbol{\omega},\boldsymbol{\omega}_r,\dot{\boldsymbol{\omega}}_r) \end{bmatrix} \begin{bmatrix} \boldsymbol{\theta}_{T} \\ \\ \boldsymbol{\theta}_{R} \end{bmatrix} \\
&= \ddot{\boldsymbol{\xi}} + \boldsymbol{\Gamma}\,\boldsymbol{\theta}
\end{aligned} \tag{5.28}
$$

The control law is implemented as:

$$
\begin{aligned}
{}^{\mathrm{b}}\boldsymbol{U} &= \ddot{\boldsymbol{\xi}}_r + \boldsymbol{\Gamma}\,\hat{\boldsymbol{\theta}} - \boldsymbol{K}_{D}\,\boldsymbol{s} \\
\boldsymbol{F}_{thrust} &= [\hat{\boldsymbol{B}}_{thrust}]^{\mathsf{T}}\,([\hat{\boldsymbol{B}}_{thrust}]\,[\hat{\boldsymbol{B}}_{thrust}]^{\mathsf{T}})^{-1}\,{}^{\mathrm{b}}\boldsymbol{U}
\end{aligned} \tag{5.29}
$$

Where:

$$
\ddot{\boldsymbol{\xi}}_r = \begin{bmatrix} \ddot{\boldsymbol{x}}_r \\ \\ \boldsymbol{0} \end{bmatrix} \;;\; \boldsymbol{s} = \begin{bmatrix} \boldsymbol{s}_{T} \\ \\ \boldsymbol{s}_{R} \end{bmatrix} \;;\; \hat{\boldsymbol{\theta}} = \begin{bmatrix} \hat{\boldsymbol{\theta}}_{T} \\ \\ \hat{\boldsymbol{\theta}}_{R} \end{bmatrix}
$$

The adaptive rules are expressed as:

$$\dot{\hat{\boldsymbol{\theta}}} = -\boldsymbol{\Upsilon}\boldsymbol{\Gamma}^{\mathsf{T}}\,\boldsymbol{s}$$

$$\dot{\hat{\boldsymbol{B}}}_{thrust} = \kappa\boldsymbol{s}\,[\boldsymbol{F}_{thrust}]^{\mathsf{T}}$$

(5.30)

Chapter 6

Model Uncertainty Effects: Simulation Results and Analysis

This chapter characterizes the performance of the nonlinear adaptive control method discussed in Chapter 5. The nonlinear control design developed in Chapter 3 serves as the baseline for comparison. The simulation architecture is the same as presented in Section 4.1. As both mission scenarios generate similar results, discussion in this chapter is limited to Scenario 1, defined in Section 4.3. Section 6.1 discusses the details of the control design. Simulation results are presented in Section 6.2. Section 6.3 provides a summary analysis of the simulation results.

6.1 Control Design

Recall from Chapter 5, the adaptive control designs are implemented as follows: Translation control from Equation 5.17:

$$[\hat{\boldsymbol{m}}_{\boldsymbol{F}}\boldsymbol{u}_{\boldsymbol{thrust,F}}] \;=\; \boldsymbol{\Gamma}_{\boldsymbol{T},m}\,\hat{\boldsymbol{\theta}}_{\boldsymbol{T},m} - \hat{\boldsymbol{m}}_{\boldsymbol{F}}\boldsymbol{K}_{\boldsymbol{D}}\boldsymbol{s}_{\boldsymbol{T}}, \; \text{With: } \dot{\hat{\boldsymbol{\theta}}}_{\boldsymbol{T},m} = -\,\boldsymbol{\Upsilon}_{\boldsymbol{T}}\,[\boldsymbol{\Gamma}_{\boldsymbol{T},m}]^{\mathsf{T}}\,\boldsymbol{s}_{\boldsymbol{T}} \quad (6.1)$$

Attitude control from Equations 5.19 and 5.20:

$$\text{Control Law: } \boldsymbol{\tau} = \boldsymbol{\Gamma}_{\boldsymbol{R}}(\boldsymbol{\omega},\boldsymbol{\omega}_r,\dot{\boldsymbol{\omega}}_r)\,\hat{\boldsymbol{\theta}}_{\boldsymbol{R}} - \boldsymbol{K}_{\boldsymbol{R}}\,\boldsymbol{s}_{\boldsymbol{R}} \quad (6.2)$$

$$\text{Adaptive Rule: } \dot{\hat{\boldsymbol{\theta}}}_{\boldsymbol{R}} = -\boldsymbol{\Upsilon}_{\boldsymbol{R}}\,\boldsymbol{\Gamma}_{\boldsymbol{R}}(\boldsymbol{\omega},\boldsymbol{\omega}_r,\dot{\boldsymbol{\omega}}_r)^{\mathsf{T}}\,\boldsymbol{s}_{\boldsymbol{R}} \quad (6.3)$$

Adaptation for thruster misalignment and performance uncertainty from Equations 5.8 and 5.23:

$$\text{Control:} \qquad \boldsymbol{F}_{thrust} = \hat{\boldsymbol{B}}_{thrust}^{\mathsf{T}}(\hat{\boldsymbol{B}}_{thrust}\,\hat{\boldsymbol{B}}_{thrust}^{\mathsf{T}})^{-1}\,\boldsymbol{u}$$

$$\text{Adaptive Rule:} \quad \dot{\hat{\boldsymbol{B}}}_{thrust} = \kappa \boldsymbol{s}[\boldsymbol{F}_{thrust}]^{\mathsf{T}}$$

The control design is based on the linear control gains presented in Section 4.2. The design goal is to implement the nonlinear adaptive control with comparable gains, removing gain selection as a factor in the performance comparison. As presented in Section 4.2, the equivalent proportional and derivative gains are computed as:

$$\boldsymbol{K}_{D,trans} = \boldsymbol{K}_{d,trans}; \qquad \boldsymbol{\Lambda}_T = [\boldsymbol{K}_{d,trans}]^{-1}\boldsymbol{K}_{p,trans}$$

$$\boldsymbol{K}_{D,att} = \boldsymbol{K}_{d,att}; \qquad \boldsymbol{\Lambda}_R = [\boldsymbol{K}_{d,att}]^{-1}\boldsymbol{K}_{p,att}$$

The adaptive mechanism for the nonlinear controller is a structured integrator built around the system dynamics. In contrast the linear control design incorporates adaptation through a simple integrator which accumulates position error, limiting gain correlation between the two designs. In fact direct correlation exists only between the gain for the linear integrator and the portion of the adaptive translation control law designed to compensate for differential gravitational and solar pressure effects.

The design goal is to specify $\boldsymbol{\Upsilon}_T$ from Equation 6.1 such that the nonlinear and linear control outputs have similar sensitivity to variations in the integrated position error. Excluding the gain associated with mass uncertainty, $\boldsymbol{\Upsilon}_T$ is specified as a

diagonal matrix with elements specified as:

$$\boldsymbol{\Upsilon_T}(i,i) \;\; = \overline{\boldsymbol{\sigma}}_{SingularValue}(\boldsymbol{K}_{i,trans}\;[\boldsymbol{\Lambda_T}]^{-1}) \tag{6.4}$$

The remaining control gains are specified based on engineering judgement and testing. The adaptive gains for mass uncertainty and thruster misalignment and performance have no direct counterpart in the linear control design. The gains specified to compensate for mass uncertainty are:

Translation Control, Mass Uncertainty Adaptive Gain: 10^6 kg/m

Attitude Control, Mass Uncertainty Adaptive Gain: 10^{11} kg-m^2/rad

For thruster misalignment and performance uncertainty the adaptive gain, κ, from Equation 5.23 is specified as 0.15 (N-m)$^{-1}$.

6.2   Simulation Results

This section compares the performance of the adaptive and nonadaptive nonlinear control designs under a varied set of model uncertainties. Model uncertainty is introduced as solar pressure effects, mass property uncertainty, and thruster misalignment/performance uncertainty. Adaptive controller performance is also simulated with a 28-day delay from the scenario epoch. Performance is independently characterized for each source of model uncertainty. The final simulation includes all sources of uncertainty. As a baseline, the simulation is run without perturbations. Results are presented in Figure 6.1 and Table 6.1. Fuel consumption for both cases is: 23.25498 meter/second. As expected the results are

nearly identical. The nonadaptive controller performance without perturbations is the benchmark for characterizing the adaptive controller tracking performance with unmodeled dynamics. Fuel consumption is compared to the ideal/perfect tracking model, discussed in Section 4.3.
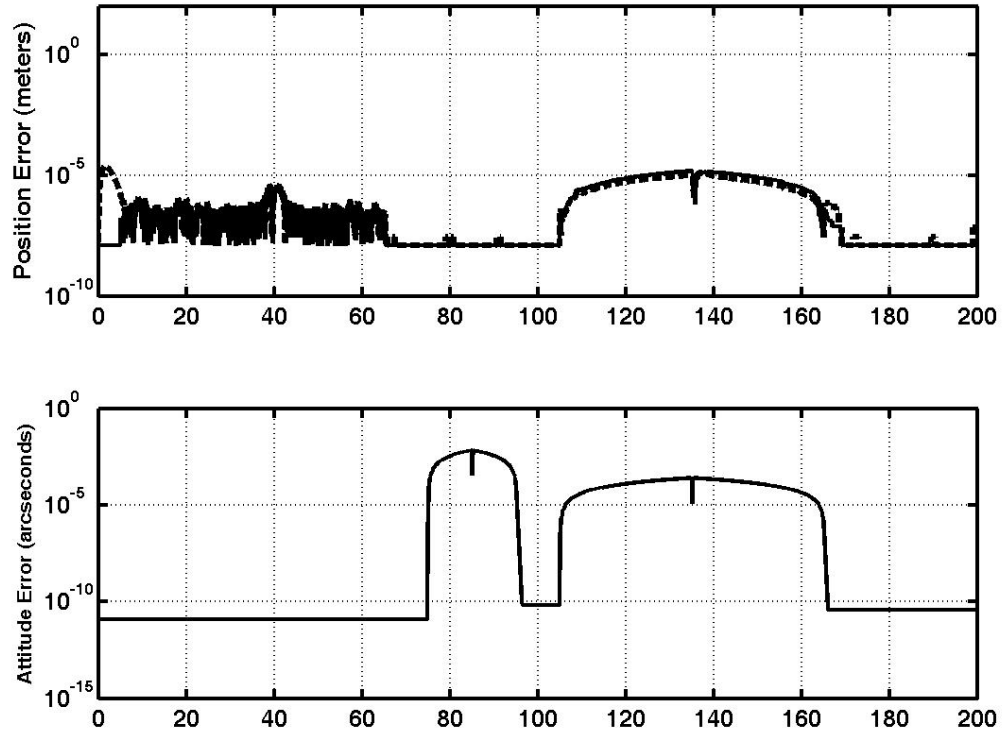

Figure 6.1: Translation/Attitude Error Profile Comparison with No Perturbation Effects for Nonlinear Nonadaptive (solid) and Adaptive (dashed) Control Algorithms

Table 6.1: Scenario 1 with No Perturbations – Nonlinear Controller Tracking Performance Comparison

Nonlinear Controller	Error			
Mode/Type	Minimum	Maximum	Mean	Units
Translation/Nonadaptive	$< 10^{-8}$ *	1.5×10^{-5}	2.4×10^{-6}	meters
Translation/Adaptive	$< 10^{-8}$ *	2.2×10^{-5}	2.0×10^{-6}	meters
Attitude/Nonadaptive	$< 10^{-11}$ *	6.8×10^{-2}	3.8×10^{-4}	arcsec
Attitude/Adaptive	$< 10^{-11}$ *	6.8×10^{-2}	3.8×10^{-4}	arcsec

* Reflects limit of numerical precision.

6.2.1 Compensation for Solar Pressure

As discussed in Section 4.1, solar pressure generates unmodeled differential acceleration between the two spacecraft. For the simulation, the solar pressure area is treated as attitude independent. The net force due to solar pressure is assumed to act at the spacecraft center of mass, resulting in zero net torque. Results are presented in Figures 6.2 and 6.3, and Tables 6.2 and 6.3. As presented in Section 5.5, the nonadaptive nonlinear controller shows approximately an order of magnitude performance degradation in the presence of solar pressure effects. In contrast, the adaptive controller exhibits equivalent performance to the baseline results. As noted in Figure 6.2 and Table 6.2, the nonlinear adaptive controller recovers the baseline nonlinear control performance presented in Section 5.3. Since the solar pressure

146

effects are modeled as torque free, the attitude performance is not affected, as shown in Figure 6.3 and Table 6.2. From Table 6.3 fuel consumption is similar for both the nonadaptive and adaptive controller.
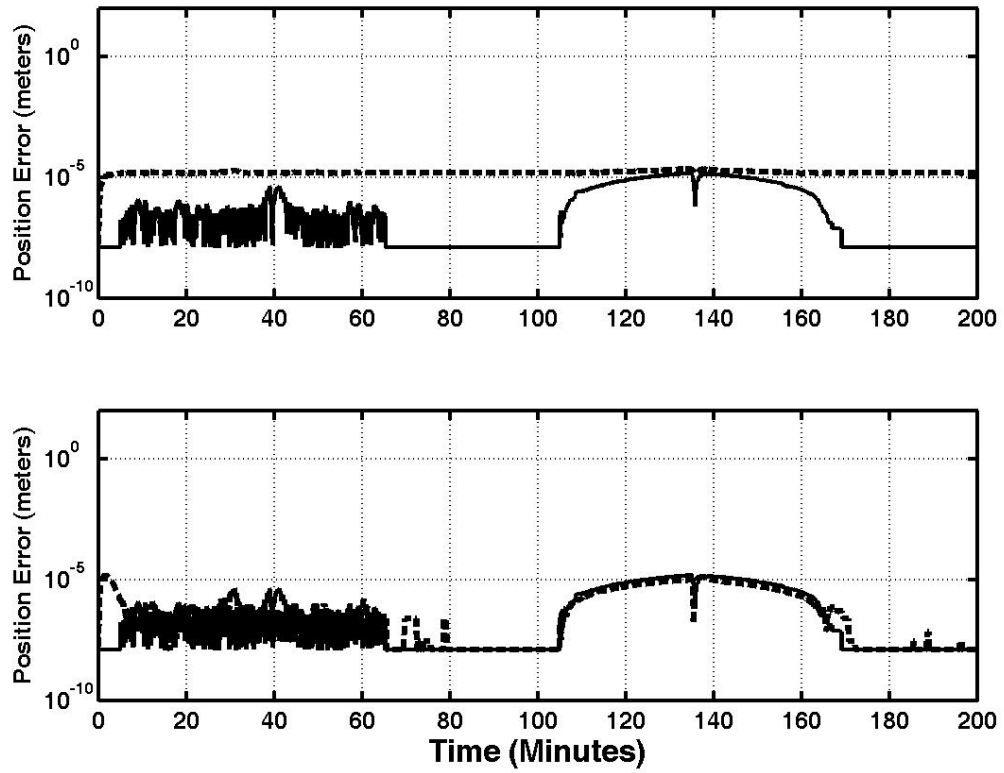
Figure 6.2: Range Error Profile, Scenario 1 with Solar Pressure Effects, Comparison with Baseline (solid), and Nonlinear Nonadaptive (top/dashed) and Adaptive (bottom/dashed) Control Algorithms
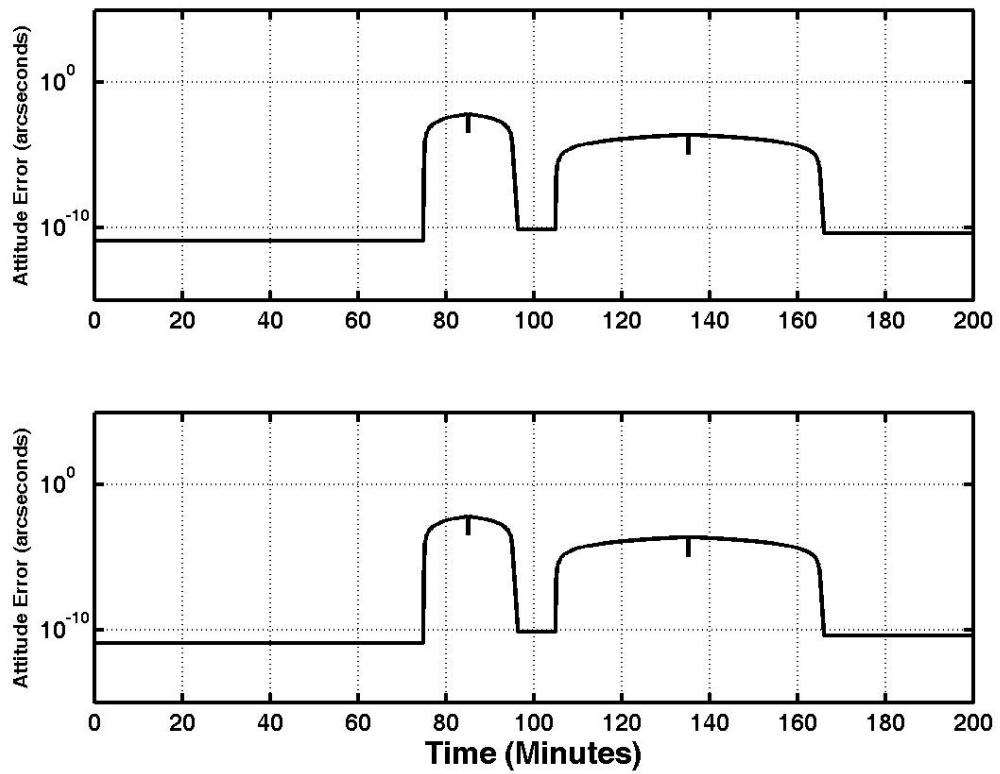
Figure 6.3: Attitude Error Profiles (Identical), Scenario 1 with Solar Pressure Effects, Comparison with Baseline (solid), and Nonlinear Nonadaptive (top/dashed) and Adaptive (bottom/dashed) Control Algorithms

Table 6.2: Scenario 1 with Solar Pressure – Nonlinear Controller Tracking Performance Comparison

Nonlinear Controller Mode/Type	Error			
	Minimum	Maximum	Mean	Units
Translation/Nonadaptive	10^{-5}	10^{-5}	1.6×10^{-5}	meters
Translation/Adaptive	$< 10^{-8}$ *	10^{-5}	1.9×10^{-6}	meters
Translation/Baseline	$< 10^{-8}$ *	10^{-5}	2.4×10^{-6}	meters
Attitude/Nonadaptive	$< 10^{-11}$ *	10^{-2}	3.8×10^{-4}	arcsec
Attitude/Adaptive	$< 10^{-11}$ *	10^{-2}	3.8×10^{-4}	arcsec
Attitude/Baseline	$< 10^{-11}$ *	10^{-2}	3.8×10^{-4}	arcsec

* Reflects limit of numerical precision.

Table 6.3: Scenario 1 with Solar Pressure – Controller Fuel Performance Summary

Nonlinear Controller Type	Fuel Consumption (meters/second)	Deviation from Ideal (Percent)
Ideal Translation/Attitude	23.25535	–
Nonadaptive Translation/Attitude	23.25498	-0.0015933%
Adaptive Translation/Attitude	23.25492	-0.0018465%

6.2.2   Compensation for Mass Property Uncertainty

Spacecraft mass properties are normally determined prior to launch. However, the true mass properties remain uncertain due to initial measurement errors and changes over the course of the mission, principally due to fuel consumption. Mass uncertainty is introduced by initializing the mass properties with "estimated" values. The estimated mass properties are used to compute the control. True mass properties are employed in the propagation. For the spacecraft mass the "estimated" value is set at 90% of the true value with the specific values:

Follower Mass: 1,980 kg, versus true value: 2,200 kg

Inertial properties are varied in several ways. First, the off-diagonal elements are ignored, and set to zero. The diagonal elements are varied by 5% of their true values and entered in the incorrect order. Specific values are:

Estimated Inertia Mass Properties:

$$\boldsymbol{H_R} = \begin{bmatrix} 190 & 0 & 0 \\ 0 & 210 & 0 \\ 0 & 0 & 315 \end{bmatrix} \text{ kg m}^2 \tag{6.5}$$

True Inertia Mass Properties:

$$\boldsymbol{H_R} = \begin{bmatrix} 200 & 10 & 5 \\ 10 & 300 & 15 \\ 5 & 15 & 200 \end{bmatrix} \text{ kg m}^2 \tag{6.6}$$

Figures 6.4 and 6.5, and Tables 6.4 and 6.5, present simulation results. Figure 6.4 and Table 6.4 describe the tracking performance for translation control. Figure 6.5 and Table 6.4 depict attitude tracking performance. Compared to solar pressure effects, mass uncertainty generates greater degradation in the nonlinear controller performance. The nonadaptive controller performance degrades by 5 orders of magnitude for translation tracking. In contrast the adaptive controller performance degrades only two to three orders of magnitude. Attitude tracking performance is also degraded, approximately three orders of magnitude for the nonadaptive controller and two orders of magnitude for the adaptive controller.
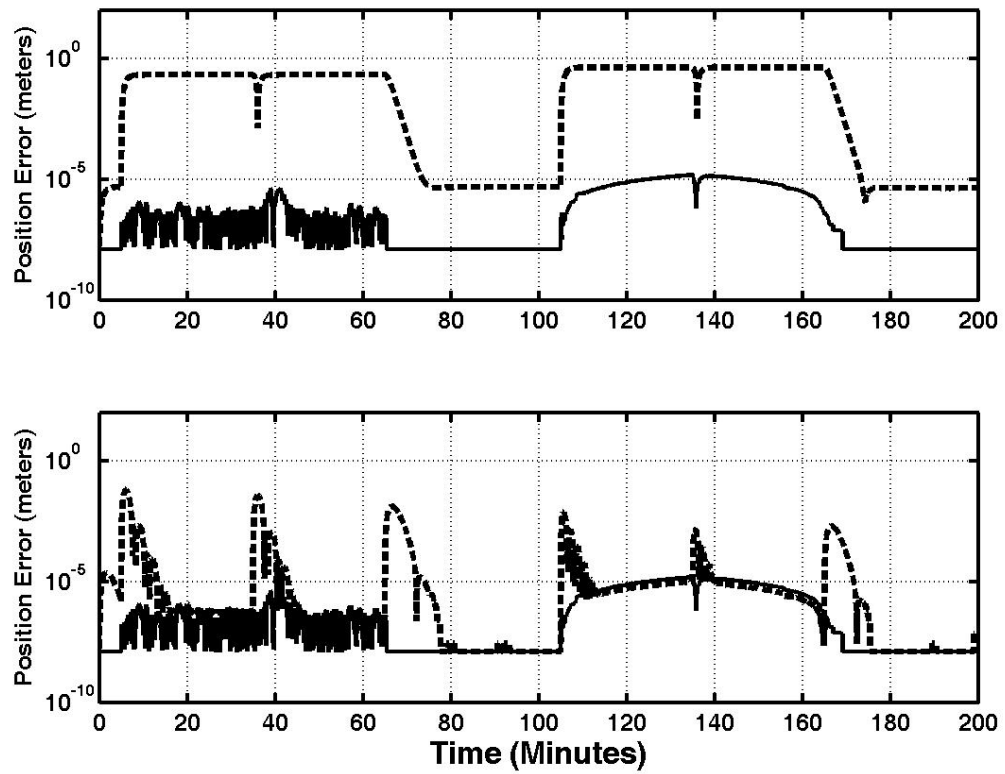
Figure 6.4: Range Error Profile Comparison, Scenario 1 with Mass Uncertainty Effects, Comparison with Baseline (solid), and Nonlinear Nonadaptive (top/dashed) and Adaptive (bottom/dashed) Control Algorithms
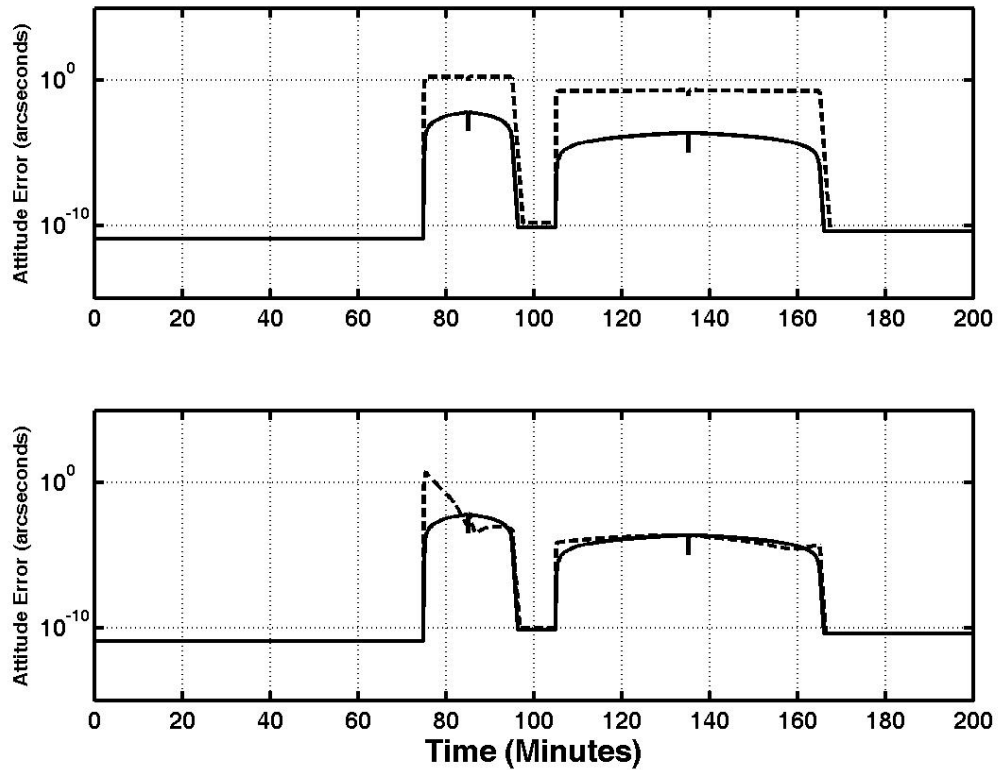
Figure 6.5: Attitude Error Profile Comparison, Scenario 1 with Mass Uncertainty Effects, Comparison with Baseline (solid), and Nonlinear Nonadaptive (top/dashed) and Adaptive (bottom/dashed) Control Algorithms

For the nonlinear adaptive controller the initial performance is perceptibly degraded, yet performance remains superior to the nonadaptive design. As the simulation progresses the performance improves to the unperturbed baseline model. To further demonstrate the advantage of the adaptive strategy the simulation was restarted using the mass parameter estimates from the first run. The values were:

Follower Mass: 2,198 kg (estimated after first run)

Inertia Mass Properties (estimated after first run):

$$\boldsymbol{H_R} = \begin{bmatrix} 186.9 & 48.3 & -16.1 \\ 48.3 & 251.6 & 34.5 \\ -16.1 & 34.5 & 194.1 \end{bmatrix} \text{kg m}^2 \tag{6.7}$$

Although the adaptive theory does not guarantee convergence of the estimated parameters to their true values, the Follower mass and the diagonal elements of the inertia matrix are closer to their true values than originally estimated. It is noted that after the second run there is no change is the estimated values for the inertia matrix. However, the estimated mass actually converges to the true value of 2,200 kg. The performance improvement during the second run is presented in Figure 6.6 and Table 6.4, comparing the results from the first and second run. The mean tracking error improves almost two orders of magnitude for both translation and attitude control. Both translation and attitude control performance approach the performance of the unperturbed system.

As shown in Table 6.5, the fuel consumption is close to the perfect tracking baseline.
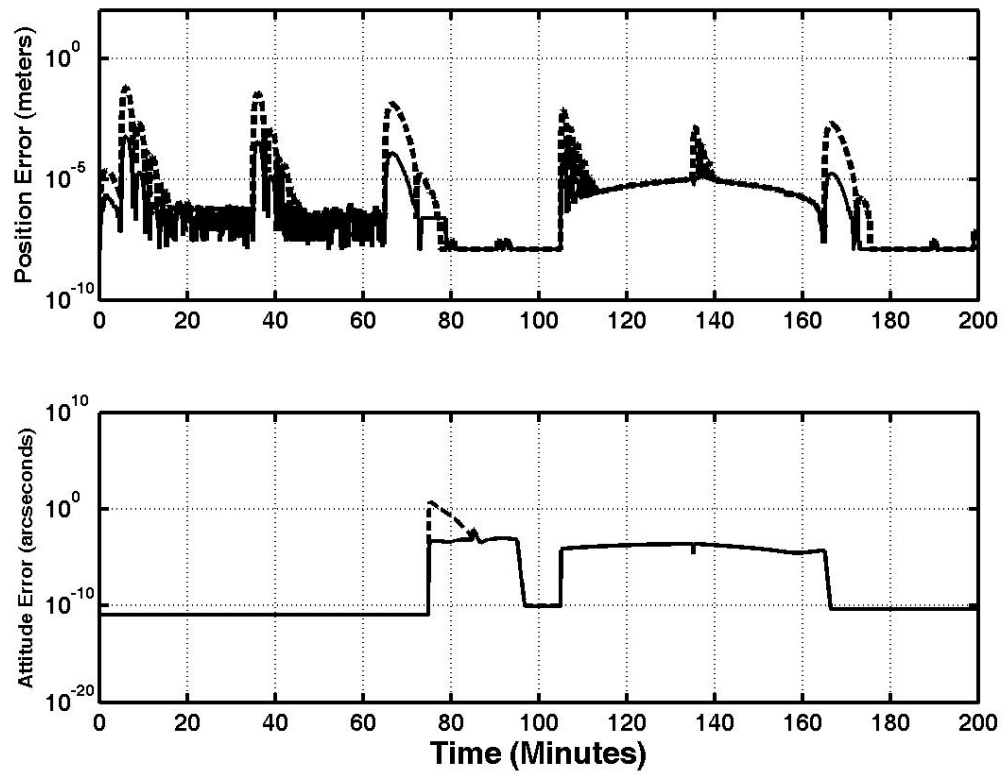
Figure 6.6: Nonlinear Adaptive Controller Performance Improvement for Second Run with Updated Mass Property Estimates. Position Tracking (top), Attitude Tracking (bottom) with Updated Parameters (solid), Original Simulation (dashed)

Table 6.4: Scenario 1 with Mass Uncertainty – Nonlinear Controller Tracking Performance Comparison

Nonlinear Controller	Error			
Mode/Type	Minimum	Maximum	Mean	Units
Translation/Nonadaptive	10^{-6}	10^{-1}	1.9×10^{-1}	meters
Translation/Adaptive	$< 10^{-8}$ *	10^{-1}	9.1×10^{-4}	meters
Translation/Adaptive (2nd Run)	$< 10^{-8}$ *	10^{-4}	1.0×10^{-5}	meters
Translation/Baseline	$< 10^{-8}$ *	10^{-5}	2.4×10^{-6}	meters
Attitude/Nonadaptive	$< 10^{-11}$ *	10^0	2.4×10^{-1}	arcsec
Attitude/Adaptive	$< 10^{-11}$ *	10^0	4.3×10^{-2}	arcsec
Attitude/Adaptive (2nd Run)	$< 10^{-11}$ *	10^{-2}	1.2×10^{-4}	arcsec
Attitude/Baseline	$< 10^{-11}$ *	10^{-2}	3.8×10^{-4}	arcsec

* Reflects limit of numerical precision.

Table 6.5: Scenario 1 with Mass Uncertainty – Controller Fuel Performance Summary

Nonlinear Controller Type	Fuel Consumption (meters/second)	Deviation from Ideal (Percent)
Ideal Translation/Attitude	23.25535	–
Nonadaptive Translation/Attitude	23.27020	0.0638510%
Adaptive Translation/Attitude	23.25583	0.0020318%
Adaptive Translation/Attitude (2nd Run)	23.25499	-0.0015807%

6.2.3   Compensation for Thruster Misalignment/Misplacement

Thruster placement and pointing are determined during the pre-launch phase of a mission. As discussed in Section 2.4, the mapping of the thruster output to the net force and torque on the spacecraft is expressed in the form of the matrix $\boldsymbol{B}_{thrust}$. The physical location and general pointing of the thrusters is not expected to change during the life of a mission. However, the spacecraft center of mass, the origin of the thruster mapping coordinate frame, will drift principally due to fuel consumption. Also, thruster output levels will vary during the life of the mission. Consequently, the true mapping matrix $\boldsymbol{B}_{thrust}$ exhibits variations during the life of a mission. The changes are sufficiently slow to track the changes using the adaptive mechanism discussed in Section 5.5.

Uncertainty is introduced in $\boldsymbol{B}_{thrust}$ by offsetting the position and direction for each thruster. Each thruster position is offset by 0.1 meters. A random set of unit vectors determines the direction of the offset. In a similar fashion the pointing direction of each thruster is subjected to a 30 degree Euler axis rotation. The Euler axis for each thruster is chosen from a random set of vectors. While each thruster is significantly displaced and repointed, the net effect is much smaller due to the random nature of the applied uncertainties. Recall the commanded thrust/torque on the spacecraft is transformed to the actual thrust torque according to the relation:

$$\mathbf{U}_{\text{actual}} = \boldsymbol{B}_{thrust} \, [\hat{\boldsymbol{B}}_{thrust}{}^{\mathsf{T}} (\hat{\boldsymbol{B}}_{thrust} \, \hat{\boldsymbol{B}}_{thrust}{}^{\mathsf{T}})^{-1}] \, \mathbf{U}_{\text{commanded}} \qquad (6.8)$$

The matrix $\boldsymbol{B}_{thrust}$ $[\hat{\boldsymbol{B}}_{thrust}{}^{\mathsf{T}}(\hat{\boldsymbol{B}}_{thrust}\ \hat{\boldsymbol{B}}_{thrust}{}^{\mathsf{T}})^{-1}]$ represents the combined effect of thruster misplacement and misalignment. To facilitate analysis, the matrix is partitioned as:

$$\boldsymbol{B}_{thrust}\ [\hat{\boldsymbol{B}}_{thrust}{}^{\mathsf{T}}(\hat{\boldsymbol{B}}_{thrust}\ \hat{\boldsymbol{B}}_{thrust}{}^{\mathsf{T}})^{-1}]\ = \begin{bmatrix} B_{1,1} & B_{1,2} \\ B_{2,1} & B_{2,2} \end{bmatrix} \tag{6.9}$$

The elements $B_{1,1}$ and $B_{2,2}$ reflect the net repointing of the thrust and torque vector, respectively. The elements $B_{1,2}$ and $B_{2,1}$ represent the coupling action introduced between the commanded thrust and torque. Based on the thruster placement/alignment uncertainty applied in the simulation, the net pointing error for the thrust vector is approximately 2.3 degrees, and 3.5 degrees for the net torque. Based on the singular values of $B_{1,1}$ and $B_{2,2}$, the magnitude of the net thrust vector varies between 72% and 116% of the commanded value. Variation of the net torque ranges between 87% and 125% of the commanded values.
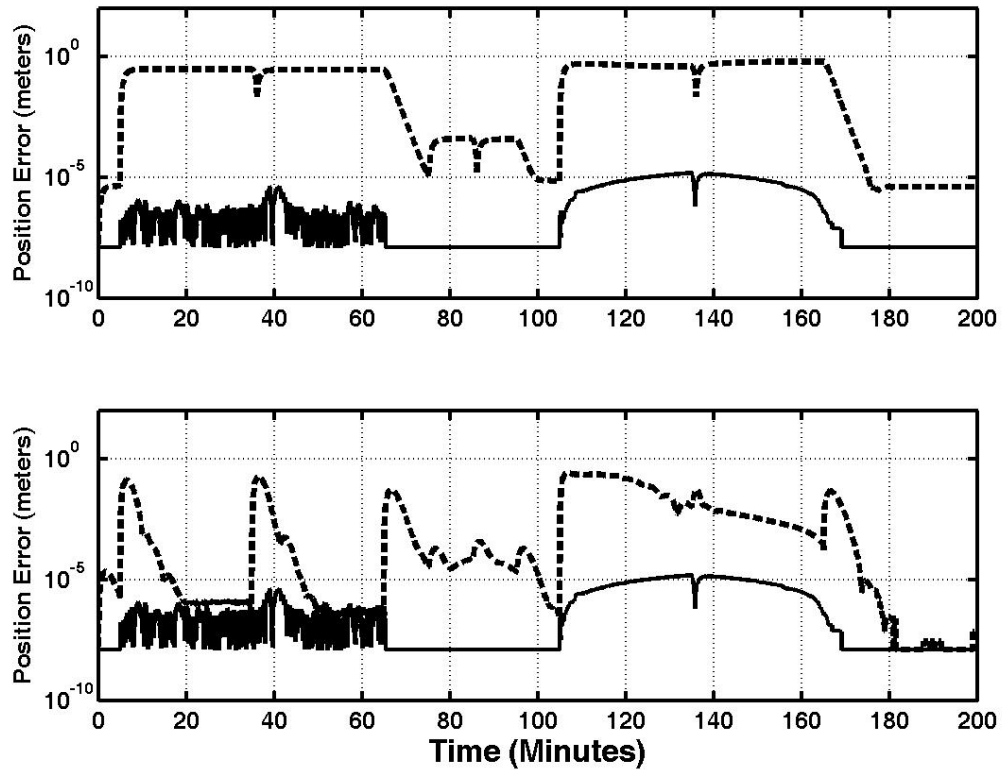
Figure 6.7: Range Error Profile Comparison, Scenario 1 with Thruster Misalignment/Performance Effects, Comparison with Baseline (solid), and Nonlinear Nonadaptive (top/dashed) and Adaptive (bottom/dashed) Control Algorithms

Simulation results are shown in Figures 6.7 and 6.8, and Tables 6.6 and 6.7. Similar to the previous cases the adaptive translation controller demonstrates the ability to compensate for uncertainty in model parameters. Translation tracking performance for the adaptive controller is significantly degraded during attitude maneuvers due to the uncertainty induced coupling between the commanded thrust and torque. The attitude error for the nonadaptive controller exhibits significant degradation during the entire control sequence.
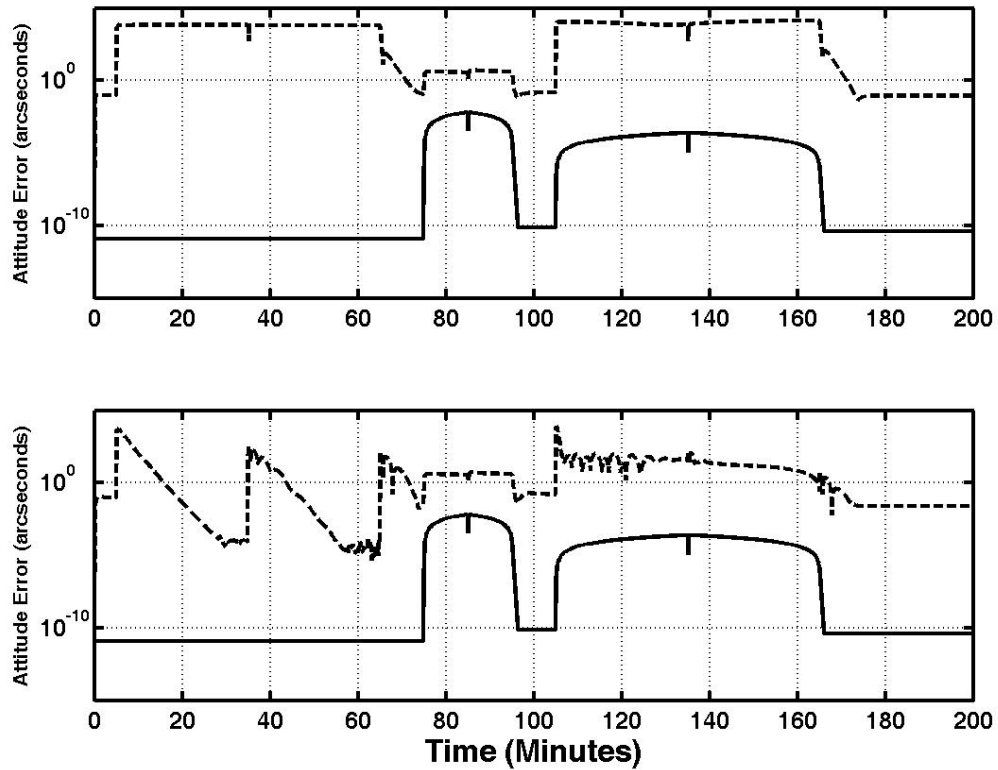
Figure 6.8: Attitude Error Profile Comparison, Scenario 1 with Thruster Misalignment/Performance Effects, Comparison with Baseline (solid), and Nonlinear Nonadaptive (top/dashed) and Adaptive (bottom/dashed) Control Algorithms

The nonlinear adaptive control performance experiences similar degradation for both translation and attitude control, as shown in Table 6.6. However, the adaptive mechanism provides performance improvement as the simulation progresses. To test the benefit of adaptation a second simulation is run using $\boldsymbol{B}_{thrust}$, as estimated from the first run. The results show improved tracking for the second run, Figure 6.9 and Table 6.6. The second run exhibits an order of

160

magnitude improvement in translation tracking, and almost an order of magnitude improvement in attitude tracking.

Fuel data, Table 6.7, shows a half percent fuel penalty for the adaptive control strategy. The penalty is reduced for the second run.
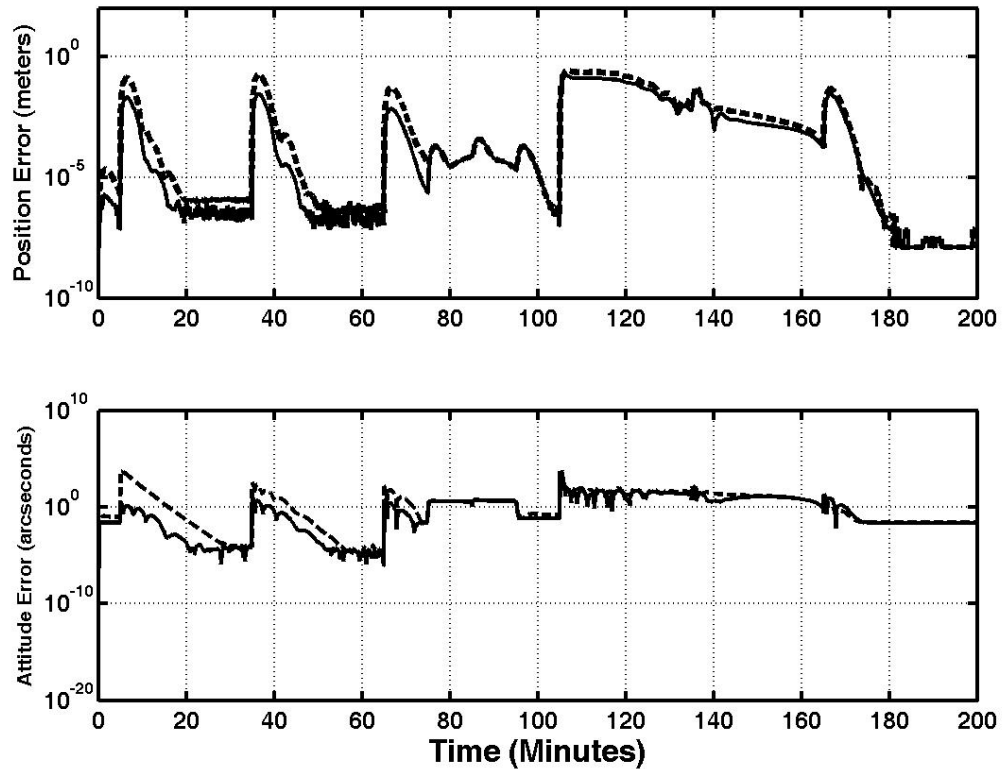
Figure 6.9: Nonlinear Adaptive Controller Performance Improvement for Second Run with Parameter Estimate Update for Thruster Misalignment/Performance Effects. Position Tracking (top), Attitude Tracking (bottom) with Updated Parameters (solid), Original Simulation (dashed)

Table 6.6: Scenario 1 with Thruster Misalignment/Performance Effects – Nonlinear Controller Tracking Performance Comparison

Nonlinear Controller	Error			
Mode/Type	Minimum	Maximum	Mean	Units
Translation/Nonadaptive	10^{-6}	10^{-1}	2.3×10^{-1}	meters
Translation/Adaptive	$< 10^{-8}$ *	10^{-1}	2.5×10^{-2}	meters
Translation/Adaptive (2nd Run)	$< 10^{-8}$ *	10^{-4}	1.3×10^{-3}	meters
Translation/Baseline	$< 10^{-8}$ *	10^{-5}	2.4×10^{-6}	meters
Attitude/Nonadaptive	10^{-1}	10^{0}	5.1×10^{3}	arcsec
Attitude/Adaptive	10^{-5}	10^{0}	7.1×10^{1}	arcsec
Attitude/Adaptive (2nd Run)	10^{-6}	10^{-2}	1.1×10^{1}	arcsec
Attitude/Baseline	$< 10^{-11}$ *	10^{-2}	3.8×10^{-4}	arcsec

* Reflects limit of numerical precision.

Table 6.7: Scenario 1 with Thruster Misalignment/Performance Effects – Controller Fuel Performance Summary

Nonlinear Controller Type	Fuel Consumption (meters/second)	Deviation from Ideal (Percent)
Ideal Translation/Attitude	23.25535	–
Nonadaptive Translation/Attitude	23.27592	0.088434%
Adaptive Translation/Attitude	23.36557	0.473950%
Adaptive Translation/Attitude (2nd Run)	23.36178	0.457650%

6.2.4 Compensation for Solar Pressure, Mass Properties, Thruster Alignment/Position Uncertainty

As a final step in characterizing the performance of the adaptive control design, performance is simulated with all sources of uncertainty applied. Perhaps expected, the results shown in Figures 6.10 and 6.11, and Tables 6.8 and 6.9, exhibit performance characteristics similar to those generated for thruster alignment/placement uncertainty, the worst case individual perturbation. Although similar, results show a slight improvement in performance with all adaptive mechanisms activated despite the presence of the perturbations associated with solar pressure and mass property uncertainty. Comparing Figures 6.7 and 6.10, the most prominent feature of improved performance is the position tracking error at the $t = 110$ minute mark in the simulation. This represents the start of the combined translation/attitude maneuver.
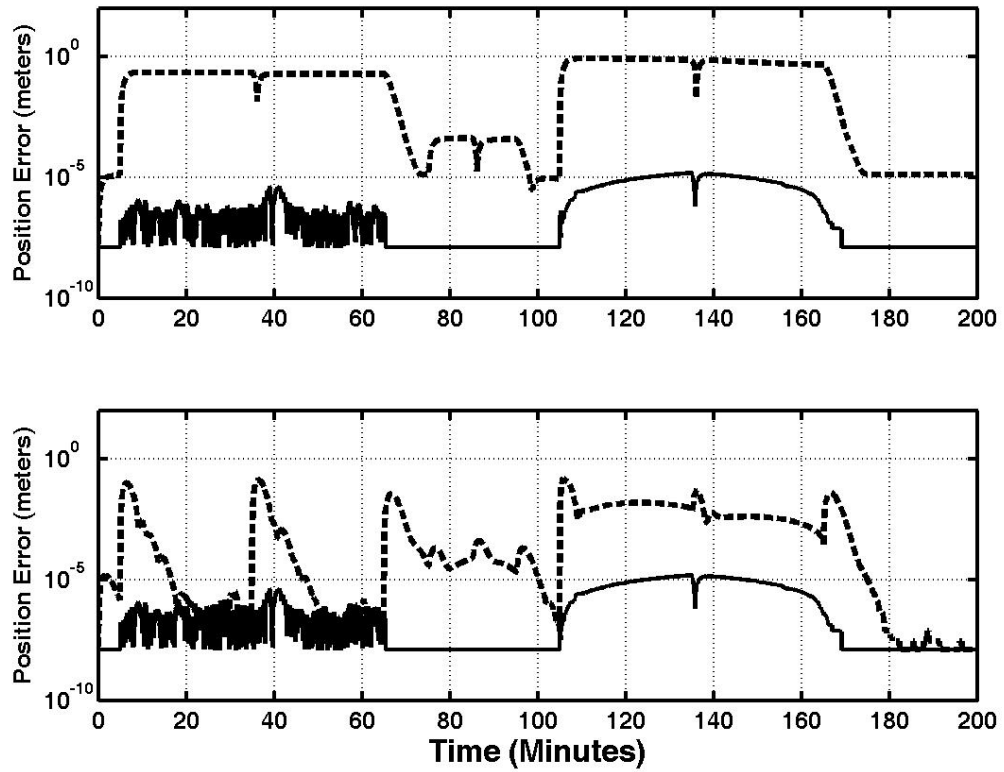
Figure 6.10: Range Error Profile Comparison, Scenario 1 with All Perturbation Effects, Comparison with Baseline (solid), and Nonlinear Nonadaptive (top/dashed) and Adaptive (bottom/dashed) Control Algorithms
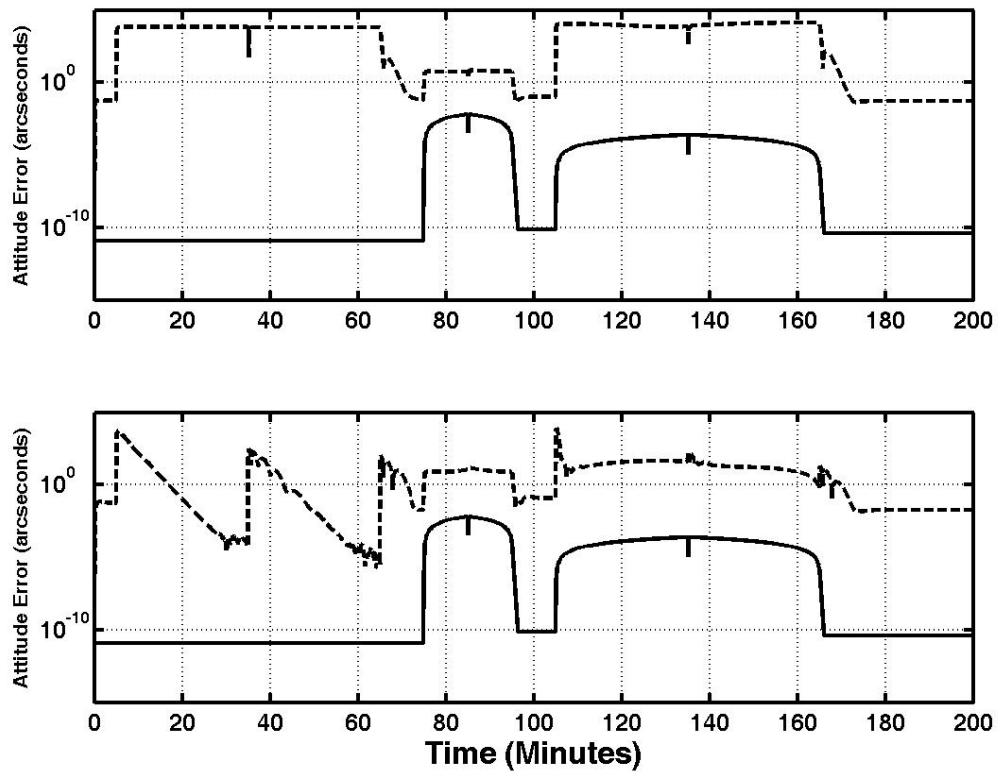
Figure 6.11: Attitude Error Profile Comparison, Scenario 1 with All Perturbation Effects, Comparison with Baseline (solid), and Nonlinear Nonadaptive (top/dashed) and Adaptive (bottom/dashed) Control Algorithms

As with the previous cases, the simulation is rerun with updated parameter estimates. As shown in Figure 6.12 and Table 6.8, tracking performance for both position and attitude continue to improve. From Table 6.9 the adaptive controller does experience a minor half percent increase in fuel usage.
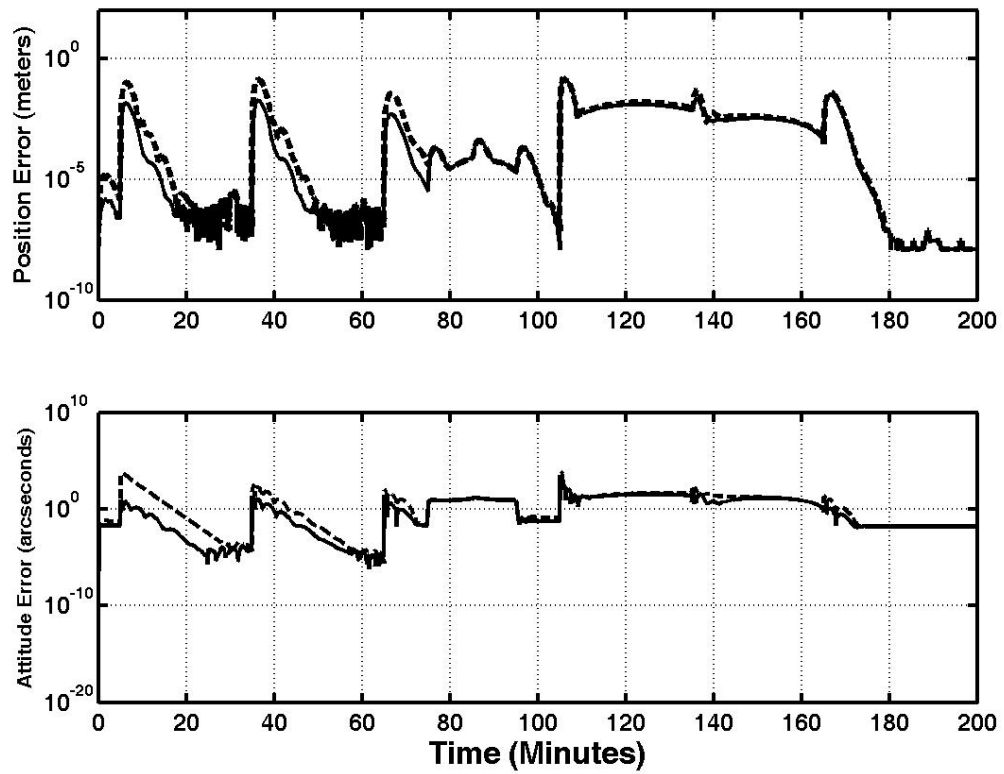
Figure 6.12: Nonlinear Adaptive Controller Performance Improvement for Second Run with Parameter Estimate Update for All Perturbation Effects. Position Tracking (top), Attitude Tracking (bottom) with Updated Parameters (solid), Original Simulation (dashed)

Table 6.8: Scenario 1 with All Perturbations – Nonlinear Controller Tracking Performance Comparison

| Nonlinear Controller	Error			
Mode/Type	Minimum	Maximum	Mean	Units
Translation/Nonadaptive	10^{-6}	10^0	2.6×10^{-1}	meters
Translation/Adaptive	$< 10^{-8}$ *	10^{-1}	7.3×10^{-3}	meters
Translation/Adaptive (2nd Run)	$< 10^{-8}$ *	10^{-1}	4.1×10^{-3}	meters
Translation/Baseline	$< 10^{-8}$ *	10^{-5}	2.4×10^{-6}	meters
Attitude/Nonadaptive	10^{-2}	10^4	5.1×10^3	arcsec
Attitude/Adaptive	10^{-5}	10^4	7.4×10^1	arcsec
Attitude/Adaptive (2nd Run)	10^{-6}	10^3	1.2×10^1	arcsec
Attitude/Baseline	$< 10^{-11}$ *	10^{-2}	3.8×10^{-4}	arcsec

* Reflects limit of numerical precision.

Table 6.9: Scenario 1 with All Perturbations – Controller Fuel Performance Summary

Nonlinear Controller Type	Fuel Consumption (meters/second)	Deviation from Ideal (Percent)
Ideal Translation/Attitude	23.25535	–
Nonadaptive Translation/Attitude	23.26750	0.05222%
Adaptive Translation/Attitude	23.36459	0.46973%
Adaptive Translation/Attitude (2nd Run)	23.36178	0.46148%

6.2.5 Performance Impact of Time Invariant Dynamics Model

As discussed in Section 4.5.5, the linear controller sustained equivalent performance through a 28 day period without a gain update. In comparison, the nonlinear adaptive controller design does not required gain updates. To demonstrate this point, Scenario 1 (without perturbations) is initiated with a start time 28 days after the epoch for gain computation. Tracking performance, Table 6.10, is unchanged. There is a slight improvement in fuel cost, as shown in Table 6.11. Graphically the performance is equivalent to the results presented in Figures 4.6, 4.7, and 4.8

Table 6.10: Scenario 1, 28 days after Epoch – Nonlinear Adaptive Controller Tracking Performance Summary

	Error			
Tracking Metric	Minimum	Maximum	Mean	Units
Translation (delay)	$< 10^{-8}$ *	10^{-5}	1.9×10^{-6}	meters
Translation (no delay)	$< 10^{-8}$ *	10^{-5}	2.2×10^{-6}	meters
Attitude (delay)	10^{-11}	10^{-3}	3.8×10^{-3}	arcsec
Attitude (no delay)	$< 10^{-11}$ *	10^{-3}	3.8×10^{-3}	arcsec

* Reflects limit of numerical precision.

Table 6.11: Scenario 1 – Nonlinear Adaptive Controller Fuel Performance Summary

Controller Type	Fuel Consumption (meters/second)	Deviation from (Ideal Percent)
Ideal Translation/Attitude	23.25535	–
Adaptive Translation/Attitude (no delay)	23.25498	-0.0015930%
Adaptive Translation/Attitude	23.25494	-0.0017685%

6.3   Summary Analysis

The results presented in the previous section sufficiently demonstrate that the nonlinear adaptive control design outperforms a similar nonadaptive controller. Based on the results in Chapter 4, the nonadaptive controller outperformed a similar linear controller. Therefore, the nonlinear adaptive controller provides the best overall performance. The superiority of the nonlinear adaptive control design lies within the adaptive integrator and inclusion of the desired acceleration term in the control law. The desired acceleration allows the controller to anticipate thrust commands, eliminating the observed characteristic transient response of the linear controller to a step input.

The adaptive mechanism of the nonlinear controller provides an enhanced integrator based on the system dynamics and a structured uncertainty model. The

nonlinear controller has the key advantage of adapting to a set of constant values. Exercising the nonlinear controller provides a learning mechanism which enhances future performance. In contrast the integrator in the linear controller chases a generally time varying control offset, and is unable to capitalize on performance history.

The chosen simulation control sequence is fairly simplistic. Further improvement in the performance of the nonlinear controller is expected with additional varied maneuvers.

These results support a general conclusion that the nonlinear adaptive controller is a superior design. Detailed analysis of control design options is required for specific missions to determine the best course of action.

Table 6.12: Scenario 1 with No Perturbations – Controller Tracking Performance Summary

	Error			
Controller Type	Minimum	Maximum	Mean	Units
Linear Translation	$< 10^{-8}$ *	10^1	3.4×10^{-1}	meters
NL Nonadaptive Translation	$< 10^{-8}$ *	10^{-5}	2.4×10^{-1}	meters
NL Adaptive Translation	$< 10^{-8}$ *	10^{-5}	2.0×10^{-1}	meters
Linear Attitude	10^{-11}	10^1	1.9×10^0	arcsec
NL Nonadaptive Attitude	$< 10^{-11}$ *	10^{-2}	3.8×10^0	arcsec
NL Adaptive Attitude	10^{-11}	10^{-2}	3.8×10^0	arcsec

* Reflects limit of numerical precision.

Table 6.13: Scenario 1 – Linear Controller Fuel Performance Summary

Controller Type	Fuel Consumption (meters/second)	Deviation from Ideal (Percent)
Ideal Translation/Attitude	23.25535	–
Linear Translation/Attitude (no delay)	23.63285	+1.6233%
Linear Translation/Attitude	23.63308	+1.6243%

Chapter 7

Summary and Conclusions

The main summary and conclusions for this research are provided in Section 1.5 at the end of Chapter 1. This chapter provides a synopsis of the contributions, topics for future research, and concluding remarks.

7.1   Contributions

This research characterizes the relative performance of linear and nonlinear control strategies for precision formation flying. The comparative analysis employs "equivalent" controller gains and incorporates an integrator in the linear control design to "level the playing field" between controller designs.

Controller performance is characterized through various simulations. The simulation design reflects a realistic space environment, including a full gravitational model and solar pressure effects. Spacecraft model properties are based on realistic mission design parameters. A fixed set of thrusters serve as control actuators for both translation and attitude control. Therefore, the control law design is based on a 6DOF control architecture, characteristic of precision formation flying control. Analysis includes the impact on controller performance due to omitted dynamics (gravitational sources and solar pressure) and model uncertainty (mass properties, thruster placement and thruster alignment). In general the prior work, cited in

Section 1.4, examines translation control only with ideal actuation and models.

Linearized equations of relative motion were derived for spacecraft operating in the context of the Restricted Three Body Problem. Prior work employed linearized dynamics based on numerical analysis, or neglected the gravity field. Although time varying, analysis demonstrated controller stability with gain scheduling. Gains are determined with a Linear Quadratic Regulator design assuming a constant linear model. For the studied case, gain scheduling within a 14-day period is recommended. Gain scheduling requirements are mission specific, and must be determined through analysis.

7.2   Results Summary

Linear and nonlinear control designs are considered to address the problem of precision formation flying. The linear control design includes development of an analytic model for the linearized equations of relative motion within the context of the restricted three body problem (RTBP). Restated results, presented in Tables 4.9 and 6.8, demonstrate the ability of the nonlinear controller to compensate for unmodeled dynamics and uncertainties. Also, the adaptive controller performance shows improvement with updated adaptation parameters.

Table 7.1: Scenario 1 with All Perturbations – Controller Tracking Performance Comparison

Nonlinear Controller	Error			
Mode/Type	Minimum	Maximum	Mean	Units
Translation/Linear	10^{-8}	10^{1}	3.4×10^{-1}	meters
Translation/Nonadaptive	10^{-6}	10^{0}	2.6×10^{-1}	meters
Translation/Adaptive	$< 10^{-8}$ *	10^{-1}	7.3×10^{-3}	meters
Translation/Adaptive (2nd Run)	$< 10^{-8}$ *	10^{-1}	4.1×10^{-3}	meters
Translation/Baseline	$< 10^{-8}$ *	10^{-5}	2.4×10^{-6}	meters
Attitude/Linear	10^{-2}	10^{4}	5.2×10^{3}	arcsec
Attitude/Nonadaptive	10^{-2}	10^{4}	5.1×10^{3}	arcsec
Attitude/Adaptive	10^{-5}	10^{4}	7.4×10^{1}	arcsec
Attitude/Adaptive (2nd Run)	10^{-6}	10^{3}	1.2×10^{1}	arcsec
Attitude/Baseline	$< 10^{-11}$ *	10^{-2}	3.8×10^{-4}	arcsec

* Reflects limit of numerical precision.

The results do not guarantee nonlinear adaptive control is the best design strategy. Rather they demonstrate a potential for improving controller performance to meet the extreme control requirements associated with formation flying missions like MAXIM and Stellar Imager. Mission specific analysis from a systems perspective is required to determine the best controller design. A systems level analysis considers all aspects of the control system, including sensors, actuators, and testing with high fidelity dynamic models.

7.3 Future Research

This research represents one step toward improving our understanding of control technology for precision formation flying. Further research is required to characterize controller performance with realistic sensor models, estimation algorithms and enhanced dynamic models. The following highlights some of the issues to be addressed.

The controller design and analysis presented in this research assumes perfect knowledge of the spacecraft states. In practice sensor measurements are employed to determine the states. A complete analysis of a controller design must incorporate appropriate sensor models. A typical sensor suite for a spacecraft formation flying application enables state measurement for relative translation and absolute attitude. Star trackers are currently the best sensor technology for fine attitude measurement in deep space. Relative attitude can be determined by differencing the absolute attitude of spacecraft pairs within the formation. Relative position/velocity sensors are an emerging technology. Sensor models are required to support controller performance analysis.

Sensor models include noise and quantization characteristics. Also, sensor performance may be state dependent. For example the design of a relative position/velocity sensor may restrict the relative spacecraft attitude for optimal performance.

Introducing noise in the measurement model motivates the requirement to consider estimation algorithms. This is particularly important with regard to

the nonlinear controller designs. A stable linear estimation algorithm can be independently designed for a linear controller application. The Separation Principal guarantees stability of a closed-loop system incorporating a stable linear controller and a stable linear estimator. However, if the controller and/or the estimator are based on a nonlinear design, combined controller/estimator stability is not guaranteed. The closed-loop stability of the combined estimator/controller must be independently verified.

An ideal sensor suite measures the full state required for controller implementation. Sensor limitations or failure can limit the measurements to a reduced state. This requires the development of strategies to extract the required full state information from the available measurements, or design controllers with reduced state requirements.

Shifting attention to enhanced spacecraft dynamic models, a number of issues arise. Higher fidelity modeling of thruster performance requires inclusion of realistic output characteristics, such as delay, saturation, range limitation and quantization. The potential for significant degradation in thruster performance (or complete failure) requires development of controller strategies with a reduced actuator set.

The controller designs presented in this research limit the actuator set to thrusters. An alternative approach incorporates momentum wheels to support attitude control. Momentum wheels add a degree of complexity to the controller design, and introduces additional challenges. Momentum wheels require inclusion of strategies to limit momentum build-up. Also, momentum wheels can introduce

spacecraft jitter due to wheel imbalance and digital wheel control.

Another important research area relates to spacecraft flexible dynamics. Spacecraft designs typically include flexible structures, i.e. solar arrays, booms and sun shades. Controller designs must incorporate provide flexible mode damping and avoid mode stimulation.

Solar torque is a related issue to spacecraft appendages and asymmetric design. Solar torque is generated by solar pressure acting on the surface of the spacecraft with a center of pressure offset from the spacecraft center of mass. The controller must incorporate compensation for attitude dependent solar torque.

These issues represent important areas for future research. In addition formation flying poses many other technology challenges related to initialization, maintenance of the global formation trajectory, communication delays, active optics, etc.

7.4 Concluding Remark – The End and a Beginning

Looking back to the opening remarks of Chapter 1, envision a small child standing in an open field beneath a clear night sky, staring up with eyes full of wonder, pondering the secrets of the universe. This quest for knowledge, this desire to explore motivates development of space-based astronomical platforms. Precision formation flying is one of many enabling technologies required to accomplish these missions.

Our quest to explore the universe is viewed as a journey with an intricate

network of paths leading to a boundary of discovery. This work represents a segment of that network, enhancing the knowledge base for spacecraft control with specific application to precision formation flying.

So this segment of the journey ends, having pushed the knowledge limit of spacecraft control a little further. Many new paths lie ahead, requiring the efforts of future researchers to pave the way for ultimate development of new space-based observatories, enabling the science community to unveil new knowledge of the universe.

Bibliography

[1] Bate, R. R., Mueller, D. D., and White J. E., *Fundamentals of Astrodynamics*, Dover Publications, Inc., New York, 1971.

[2] Battin, R. H., *An Introduction to the Mathematics and Methods of Astrodynamics*, AIAA Education Series, AIAA, New York, 1987.

[3] Beard, R. W., Lawton, J. and Hadaegh, F. Y., "A Coordination Architecture for Spacecraft Formation Control," *IEEE Trans. on Control Systems Technology*, November 2001.

[4] Bronowski, J., *The Ascent of Man* (Little, Brown and Company, Boston/Toronto, 1973).

[5] Carpenter, J. R., Leitner, J. A., Burns, R. D. and Folta, D. C., "Benchmark Problems for Spacecraft Formation Flying Mission," *Proceedings of the AIAA Guidance, Navigation and Control Conference*, August 2003, Paper No. AIAA 2003-5364.

[6] Carpenter, K. G., et al., "The Stellar Imager (SI) Mission Concept," *SPIE's Astronomical and Instrumentation Conference*, Waikoloa, Hawaii, August 2002.

[7] Carpenter, K. G., et al., "SI-Stellar Imager," *Vision Mission Study Report*, NASA Goddard Space Flight Center, September 15, 2005.

[8] Cash, W. C., Gendreau, K. C., Shipley, A. F. and Gallagher, D., "MAXIM Pathfinder: A Practical Configuration," *SPIE's Conference on Optics for EUV, X-Ray, and Gamma-Ray Astronomy*, San Diego, CA, August 2003.

[9] Chen, C., *Linear System Theory and Design*, CBS College Publishing, New York, 1974.

[10] "The Constellation X (Con-X) Homepage," http://constellation.gsfc.nasa.gov/

[11] Crouch, P. E., "Spacecraft Attitude Control and Stabilization: Applications of Geometric Control Theory to Rigid Body Models," *IEEE Trans. on Automatic Control*, April 1984.

[12] de Queiroz, M. S., Kapila, V. and Yan, Q., "Adaptive Nonlinear Control of Multiple Spacecraft Formation Flying," *Journal of Guidance, Control, and Dynamics*, May-June 2000.

[13] Dorato, P., Adballah, C. and Cerone, V., *Linear Quadratic Control, An Introduction*, Prentice Hall, Inc., New Jersey, 1995.

[14] Egeland, O. and Godhavn, J. M., "Passivity-Based Adaptive Attitude Control of a Rigid Spacecraft," *IEEE Trans. on Automatic Control*, April 1994.

[15] Folta, D. and Hawkins, A., "Results of NASA's First Autonomous Formation Flying Experiment: Earth Observing-1 (EO-1)," *Proceedings of the AAS/AIAA Astrodynamics Specialist Conference*, August 2002, Paper No. AIAA 2002-4743.

[16] Fossen, T. I. and Sagatun, S. I., "Adaptive Control of Nonlinear Underwater Robotic Systems," *Proceedings of the 1991 IEEE International Conference on Robotics and Automation*, April 1991.

[17] Fossen, T. I., *Guidance and Control of Ocean Vehicles*, John Wiley and Sons Ltd., West Sussex, England, 1994 (Reprinted May 1998).

[18] "Freeflyer", Spacecraft Analysis Software by a.i. Solutions, Lanham, Maryland, http://www.ai-solutions.com/

[19] Gendreau, K. C., Cash, W. C., Shipley, A. F. and White, N., "The MAXIM Pathfinder X-ray Interferometry Mission," *SPIE's X-Ray and Gamma-Ray Telescopes and Instruments for Astronomy Conference*, Waikoloa, Hawaii, August 2002.

[20] Gendreau, K. C., Leitner, J., Markley, L., Cash, W. C. and Shipley, A. F., "Requirements and Options for a Stable Inertial Reference Frame for a 100 μarcsecond Imaging Telescope," *SPIE's X-Ray and Gamma-Ray Telescopes and Instruments for Astronomy Conference*, Waikoloa, Hawaii, August 2002.

[21] Gendreau, K. C., Cash, W. C., Shipley, A. F. and White, N., "The MAXIM Interferometry Mission," *SPIE's X-Ray and Gamma-Ray Astronomy Conference Proceedings*, Vol. 5168, pp 420-434, SPIE, Bellingham, WA, 2004.

[22] Gendreau, K. C., Cash, W. C., Shipley, A. F. and White, N., "MAXIM: The Black Hole Imager," *SPIE's UV and Gamma-Ray Space Telescope Systems Conference Proceedings*, Vol. 5488, pp 394-402, SPIE, Bellingham, WA, 2004.

[23] Goebel, D. M., Katz, I., Ziemer, J., Brophy, J. R., Polk, J. E. and Johnson, L., "Electric Propulsion Research and Development at JPL," *AIAA/ASME/SAE/ASEE Joint Propulsion Conference & Exhibit* , July 2005, Paper No. AIAA-2005-3535.

[24] Green, M. and Limebeer, D., *Linear Robust Control* (Prentice-Hall, Inc., Englewood Cliffs, New Jersey, 1995).

[25] Gurfil, P., Idan M. and Kasdin, N. J., "Adaptive Neural Control of Deep-Space Formation Flying," *Journal of Guidance, Control, and Dynamics*, Vol. 26, No. 3, May-June 2003, pp. 491-501.

[26] Hamilton, N. H., Folta, D. and Carpenter, R., "Formation Flying Satellite Control Around The L2 Sun-Earth Libration Point," *Proceedings of the AAS/AIAA Astrodynamics Specialist Conference*, August 2002

[27] Hsiao, F. Y. and Scheeres, D. J., "Design of Spacecraft Formation Orbits Relative to a Stabilized Trajectory," *Journal of Guidance, Control, and Dynamics*, Vol. 28, No. 4, July-August 2005, pp. 782-794.

[28] Ioannou, P. A. and Sun J., *Robust Adaptive Control*, Prentice Hall, Inc., New Jersey, 1996.

[29] Isidori, A., *Nonlinear Control Systems*, Springer-Verlag, Great Britain, 1995 (3rd. Ed.).

[30] "JPL Solar System Dynamics, Planetary Ephemeris Data", http://ssd.jpl.nasa.gov/?ephemerides.

[31] Kailath, T, *Linear Systems*, Prentice Hall, Inc., New Jersey, 1980.

[32] Kapila, V., Sparks, A. G., Buffington, J. M. and Yan, Q., "Spacecraft Formation Flying: Dynamics and Control," *Journal of Guidance, Control, and Dynamics*, Vol. 23, No. 3, May-June 2000, pp. 561-564

[33] Khalil, H. K., *Nonlinear Systems*, Prentice Hall, Inc., New Jersey, 1996 (2nd. Ed.).

[34] Krstić, M., Kanellakopoulos, I., and Kokotović, P., *Nonlinear and Adaptive Control Design*, John Wiley & Sons, Inc., New York, 1996 (2nd. Ed.).

[35] Lawson, P. R., "The Terrestrial Planet Finder: the Search for Life Elsewhere," *Proceedings of the 1999 IEEE Areospace Conference*, Aspen, CO, March 2001, Vol. 4, pp. 2005-2011.

[36] Leitner, J., Bauer, F., Folta, D., Moreau, M., Carpenter, R., and How, J., "Formation in Flight Distributed Spacecraft Systems Develop New GPS Capabilities," *GPS World*, Feb. 2002.

[37] Lieber, M. and Gallagher, D., "System performance evaluation of the MAXIM concept with integrated modeling," *SPIE's X-Ray and Gamma-Ray Telescopes and Instruments for Astronomy Conference*, Waikoloa, Hawaii, August 2002.

[38] Luquette, R. J. and Sanner, R. M., "A Nonlinear Approach to Spacecraft Trajectory Control in the Vicinity of a Libration Point," *Proceedings of the Flight Mechanics Symposium*, Goddard Space Flight Center, June 2001.

[39] Luquette, R. J. and Sanner, R. M., "A Nonlinear Approach to Spacecraft Formation Control in the Vicinity of a Collinear Libration Point," *Proceedings of the AAS/AIAA Astrodynamics Specialist Conference*, July 2001, Paper No. AAS 01-330.

[40] Luquette, R. J. and Sanner, R. M., "A Nonlinear, Six-Degree of Freedom, Precision Formation Control Algorithm, Based on Restricted Three Body Dynamics," *26th Annual AAS Guidance and Control Conference*, February 2003, Paper No. AAS 03-007.

[41] Luquette, R. J. and Sanner, R. M., "Linear State-Space Representation of the Dynamics of Relative Motion, Based on Restricted Three Body Dynamics," *AIAA Guidance, Navigation and Control Conference*, August 2004, Paper No. AIAA-2004-4783.

[42] Luquette, R. J., Sanner, R. M., Leitner, J. and Gendreau, K. C., "Formation Control for the MAXIM Mission," *2nd International Symposium on Formation Flying*, September 2004.

[43] Marchand, B. G. and Howell, K. C., "Control Strategies for Formation Flight in the Vicinity of the Libration Points," *Journal of Guidance, Control, and Dynamics*, Vol. 28, No. 6, November-December 2005, pp. 1210-1219.

[44] "Official Web Site for the MicroArcsecond X-Ray Imaging Mission (MAXIM)," http://maxim.gsfc.nasa.gov/.

[45] Mesbahi, M. and Hadaegh, F. Y, "Formation Flying Control of Multiple Spacecraft via Graphs, Matrix Inequalities, and Switching," *Journal of Guidance, Control, and Dynamics*, Vol. 24, No. 2, March-April 2001, pp. 369-377.

[46] Moulton, F.R.,*An Introduction to Celestial Mechanics* (The MacMilliam Company, Copyright 1914, 12th Printing, 1959).

[47] "NASA Space Science Enterprise, New Millennium Program, Space Technology 9 (ST9)," http://nmp.jpl.nasa.gov/st9/.

[48] Noecker, C. and Kilston, S., "Terrestrial Planet Finder: the Search for Life Elsewhere," *Proceedings of the 1999 IEEE Areospace Conference*, Aspen, CO, March 1999, Vol. 4, pp. 49-57.

[49] Ogata, K., *Modern Control Theory*, Prentice Hall, Inc., New Jersey, 1997 (3rd. Ed.).

[50] Polzin, K. A., Choueiri, E. Y., Gurfil, P. and Kasdin, N. J., "Plasma Propulsion Options for Multiple Terrestrial Planet Finder Architectures," *Journal of Spacecraft and Rockets*, Vol. 39, No. 3, May-June 2002, pp. 347-356.

[51] Rugh, W. J., *Linear System Theory*, Prentice Hall, Inc., New Jersey, 1996 (2nd. Ed.).

[52] "Satellite Tool Kit", Spacecraft Analysis Software by Analytic Graphics Incorporated, Exton, Pennsylvania, http://www.agi.com/

[53] Scharf, D. P., Hadaegh, F. Y. and Ploen, S. R., "A Survey of Spacecraft Formation Flying Guidance and Control (Part II): Control," *Proceedings of the 2004 American Control Conference*, pp 2976-2985, Boston, Massachusetts, June 30-July 2, 2004.

[54] Sengupta P. and Vadali, S. R., "Satellite Orbit Transfer and Formation Reconfiguration via an Attitude Control Analogy," *Journal of Guidance, Control, and Dynamics*, Vol. 28, No. 6, November-December 2005, pp. 1200-1209.

[55] Shipley, A. F., Cash, W. C., Gendreau, K. C. and Gallagher, D., "MAXIM Interferometer Tolerances and Tradeoffs," *SPIE's X-Ray and Gamma-Ray Telescopes and Instruments for Astronomy Conference*, Waikoloa, Hawaii, August 2002.

[56] "The Stellar Imager (SI) Homepage," http://hires.gsfc.nasa.gov/~si/.

[57] Slotine, J. J. E. and Di Benedetto, M. D., "Hamiltonian Adaptive Control of Spacecraft," *IEEE Trans. on Automatic Control*, July 1990.

[58] Slotine, J. and Li, W., *Applied Nonlinear Control*, Prentice Hall, Inc., New Jersey, 1991.

[59] Smith, R. S. and Hadaegh, F. Y., "Control of Deep-Space Formation-Flying Scacecraft: Relative Sensing and Switched Information," *Journal of Guidance, Control, and Dynamics*, Vol. 28, No. 1, January-February 2005, pp. 106-114.

[60] "The Astronomical Almanac," Nautical Almanac Office, U.S. Naval Observatory, 1999.

[61] "The Terrestrial Planet Finder (TPF) Homepage," http://planetquest.jpl.nasa.gov/TPF/tpf_index.html.

[62] Vaddi S. S., Alfriend K. T., Vadali, S. R. and Sengupta P., "Formation Establishment and Reconfiguration Using Impulsive Control," *Journal of Guidance, Control, and Dynamics*, Vol. 28, No. 2, March-April 2005, pp. 262-268.

[63] Vassar, R. H. and Sherwood, R. B., "Formationkeeping for a pair of Satellites in a Circular Orbit," *Journal of Guidance, Control, and Dynamics*, Vol. 8, No. 2, March-April 1985, pp. 235-242.

[64] Vogt, B., LeBrouef, R., Kim, J., Sanneman, R., and McCullough, M., "Attitude Control System Handbook," *Prepared by Swales Aerospace for NASA/GSFC/Flight Dynamics and Analysis Branch*, June 2002.

[65] Wang, P. K. C., Hadaegh, F. Y. and Lau, K., "Synchronized Formation Rotation and Attitude Control of Multiple Free-Flying Spacecraft," *Journal of Guidance, Control, and Dynamics*, Vol. 22, No. 1, January-February 1999, pp. 28-35.

[66] Wen, T. W. and Kreutz-Delgado, K., "The Attitude Control Problem," *IEEE Trans. on Automatic Control*, October 1991.

[67] Wertz, J. R., *Spacecraft Attitude Determination and Control*, Kluwer Academic Publishers, Holland, 1978 (1999 Reprint).

[68] Wie, B., *Space Vehicle Dynamics and Control*, AIAA Education Series., AIAA, Inc. Virginia, 1998.

[69] Zhou, K., *Essential of Robust Control*, Prentice Hall, New Jersey, 1998.